3D PRINTED MUON DETECTOR STRUCTURES

Submitted to Swansea University in fulfilment of the requirements for the degree of Master of Science by Research (MscR) in Material Engineering

AUGUST 31, 2022

SAMUEL CRESSALL
College of Engineering
Swansea university
Bay Campus
Swansea
SA1 8EN
2022

Abstract

The work presented in this thesis explores the feasibility of incorporating additive manufacturing (AM) solutions into the fabrication of structural components in cosmic-ray muon imaging (muography) systems. The work has been sponsored by Lynkeos Technology Limited (UK) who deploys muography to investigate nuclear waste containers. Currently, muography is in the early stage of industry adoption and offers advantages over traditional non-destructive testing (NDT) methods in safety, deployment, and material. This thesis has identified three challenges to realise the technology's commercial potential: timescales needed per image, design and assembly of the structure, and costs of materials and components. Lynkeos has previously collaborated with Swansea University to produce a proof of concept 3D printed structure which encases the required components. To address challenges, the system's fabrication, material, and assembly have been investigated and improved upon by applying a design process and accelerated lifecycle testing.

The constraints, limitations and objectives of the system deigns have been summarised in a product design specification (PDS). Building on the PDS a novel design solution is proposed which improved upon previous design attempts by integrating electronics and incorporating modularity into the design. The novel design solution has demonstrated a detection area of 0.05m^2, which is an increase of 335% over the previous design proposal. Additionally, the design was more compact than previous designs improving the portability. The novel design proved successful in measuring background radiation and locating a beta source emitter within the detection plane, demonstrating the feasibility of the modular design. Further conceptualised improvements leveraging AM design capabilities have decreased print time by 38% and material used by 36%, making the component more economically viable. The improvements also increase the probability of muon detection, reducing the time scale required for image reconstruction.

The work then reviewed the radiation robustness of 3D printed parts. Accelerated lifetime testing was carried out to mimic the operating conditions of Lynkeos' system. The first-ever characterisation of the response of Polyethylene Terephthalate Glycol (PETG) and Acrylonitrile Butadiene Styrene (ASA) to gamma radiation was carried out. The findings indicate that PETG exhibits excellent mechanical resistance to high-intensity gamma radiation. At an exposure of 0.75 MGy, PETG maintained 99.2% and 93% of its ultimate tensile strength and maximum strain, respectively. This exposure is over ten times the recommended dose the previously used material, polylactic acid, can withstand. These findings support Lynkeos' manufacturing of cosmic-ray muon imaging structures and influence other industries hoping to leverage AM technologies in radioactive environments.

Acknowledgements

I wish to thank Prof. Davide Deganello and Dr. Christopher Phillips, at Swansea University, who acted as my academic supervisors. They have provided excellent support in preparing this thesis and pushed me to be the best academic I can be.

I would also like to thank Dr. David Mahon and the entire Lynkeos team. Who have helped me enormously throughout the process. I am grateful to have been a part of such a fantastic team.

A final thanks to Dr. Wafaa Al-Shatty for supporting me with testing and guiding me through the research process, always fast to respond to my never-ending emails.

For Sarah, Duncan, Ollie, and Josh

Declarations

This work has not previously been accepted in substance for any degree and is not being concurrently submitted in candidature for any degree.

Signed 

Date: 02/09/2022

This thesis is the result of my own investigations, except where otherwise stated. Other sources are acknowledged by footnotes giving explicit references. A bibliography is appended.

Signed 

Date: 02/09/2022

I hereby give consent for my thesis, if accepted, to be available for photocopying and for inter-library loan, and for the title and summary to be made available to outside organisations.

Signed 

Date: 02/09/2022

The University's ethical procedures have been followed and, where appropriate, that ethical approval has been granted.

Signed 

Date: 02/09/2022

Contents

List of Acronyms

NDT	Non-Destructive Testing
AM	Additive Manufacturing
MR	Muon Radiography
MT	Muon Tomography
MIS	Muon Imaging System
NNL	National Nuclear Laboratory
RP	Rapid Prototyping
CNC	Computer Number Controlled
GRP	Ground Penetrating Radar
SAFT	Synthetic Aperture Focusing Technique
PDE	Photon Detection Efficiency
SiPM	Silicon Photomultipliers
SLA	Stereolithography
SLS	Selective Laser Sintering
FDM	Fused Deposition Modelling
LOM	Lamination Object Manufacturing
UC	Ultrasonic Consolidation
SLM	Selective Laser Melting
EBM	Electron Beam Melting
LENS	Laser Net Shape Engineering
CAD	Computer-Aided Design
.STL	Stereolithography file
ABS	Acrylonitrile Butadiene Styrene
PLA	Polylactic Acid
PETG	Polyethylene Terephthalate Glycol
ASA	Acrylonitrile Styrene Acrylate
PEEK	Polyether Ether Ketone
FRP	Fibre Reinforced Plastics
CFRP	Carbon Fibre Reinforced Plastic
GRP	Glass Reinforced Plastics
UTS	Ultimate Tensile Strength
PDS	Product Design Specification
FER	Front end readout

List of Figures

List of Tables

List of Equations

Chapter 1: Scope, Background and, Motivation

1.1 Scope

The work was carried out in collaboration with Lynkeos Technology, a spinout from the University of Glasgow working in the passive non-destructive testing (NDT) field of cosmic-ray muography. Muography has been identified as a disruptive technology that can provide advantages over existing NDT methods. Muography has the potential to aid numerous industries in defect detection, structural monitoring, and nuclear material identification. The research focused on addressing key barriers limiting widespread industrial adoption of muography technology as an NDT technique, namely high detector materials costs, construction costs, and portability issues.

Previous attempts using additive manufacturing (AM) to fabricate the structural components of particle detectors by 3DScint have demonstrated the feasibility of the approach. The work presented in this thesis improves upon previous attempts from a design and material perspective. The objective of the improvements is set out in a product design specification (PDS), in Table 3.1, to develop the scalability, mobility, and adaptability of the system. These aims are achieved by investigating the design and fabrication of the encasing structure, which house electrical and optical components required for detection. Further investigation is carried out into the material suitability through accelerated lifecycle testing of polymers exposed to gamma radiation validating the materials' robustness to expected operating environmental conditions.

The work presented provides an overview of enabling technologies, applies a design process framework, and validates the material compatibility for applying additive manufacturing (AM) techniques to these challenges. Recommendations and other considerations produced in the work provide improvements to the design and manufacture for future integration of AM technologies into the fabrication of muography systems.

1.2 Background: Non-Destructive Testing and Muography

The global Non-destructive testing (NDT) market was valued at $ 16.72 billion in 2022 and is expected to grow to $ 24.64 billion by 2026 (Mordor Intelligence) [1]. This growth is fuelled by the increase in defect detection for products, plants and structures to improve operational safety. Specifically, there is increasing electrical generation occurring at nuclear power plants; NDT systems

are being used to monitor and control these power plants, e.g., reducing the failure rate of fuel rods. Furthermore, known limitations of incumbent technologies motivate the development of new capabilities [1]. However, the high equipment cost and lack of skilled technicians restrain the NDT's market growth [1]. Cosmic-ray muon imaging (muography) is one such innovation that may offer advantages over traditional NDT methods, including the ability to inspect defects deeper inside structures, operate entirely passively, and minimise safety precautions. Recent proof-of-concept research has indicated that the technology could be a competitive alternative to traditional NDTs [2].

Applications of muography absorption measurements date back to 1955. When researchers investigated the thickness of ice formation above a mining tunnel in Australia [3]. It wasn't until 1970 when chambers hidden within the pyramid of Giza were investigated [4], that cosmic-ray muon 3D imaging first gained the public's attention as an NDT technique. Alvarez concluded that no chamber of the expected size exists. However, with advancements in technology, in 2017, researchers successfully discovered a 30-meter-long space within the pyramids [5].

Muography has the potential to be a disruptive technology in existing NDT markets, such as X-ray, radar, and ultrasound. For example, muography uses naturally occurring cosmic rays, significantly reducing the health and safety precautions compared to X-rays. Muons are also highly penetrative, allowing deeper measurements compared to radar or ultrasound. Finally, the passive nature of muons allows for a range of volumes to be investigated, spanning many orders of magnitude without the risk of damage [6]. In light of these advantages, companies are beginning to investigate the potential for muography to monitor the degradation of civil structures to help with early failure detection. Additionally, there is growing interest in using muography to identify and image nuclear material. Either onboard shipping containers to rapidly identify contraband or to visualise the internal make-up of waste nuclear energy silos.

Advancements in the understanding, technology, materials, and industrial applications of muography, have led to rapid growth in research. Figure 1.1 shows the number of publications since 1950 which contained the phrase 'Muography' from Google Scholar. The research rate is rapidly growing; there have been more publications in the last two years than in the five years before. From this, it is evident that researchers and companies are keen to realise the potential of this technology.

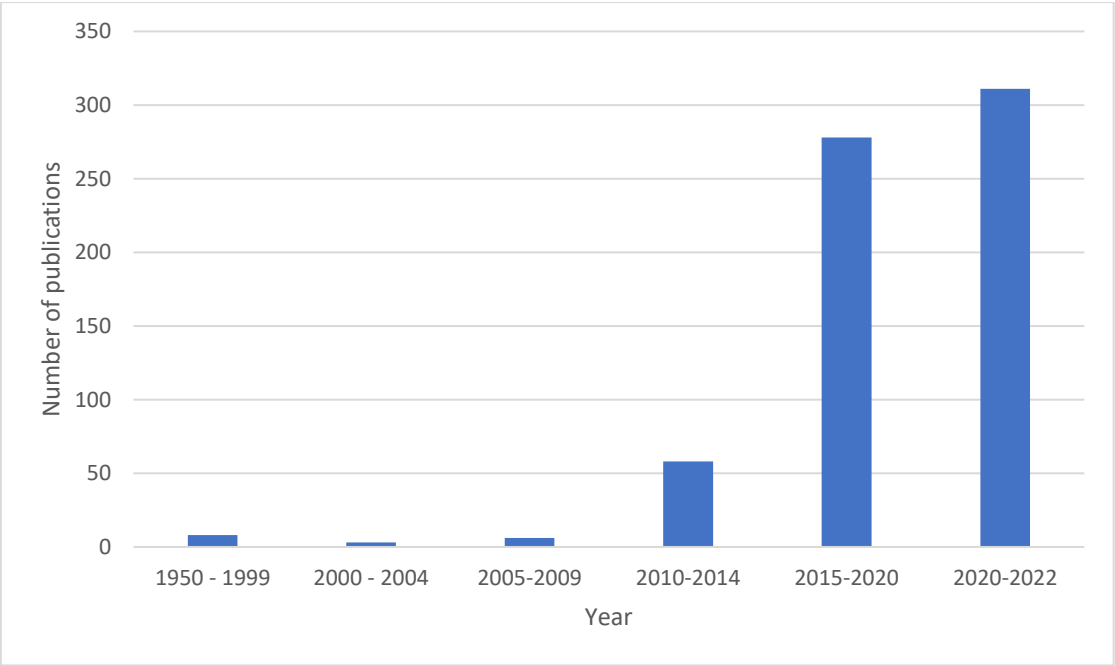

Figure 1.1 *– Number of publications including 'muography' since the 1950s. The search was carried out on google scholar containing the phrase 'muography' in the publication title*

1.3 Motivation: Lynkeos Technologies Limited

The research presented in this thesis has been sponsored by Lynkeos Technologies Ltd [7]. Lynkeos is a spinout company from the University of Glasgow that has been operating since 2016. In 2018, Lynkeos achieved CE certification for their Muon Imaging System (MIS) and secured the first commercial imaging contract with the National Nuclear Laboratory (NNL). Currently, Lynkeos have secured contacts with Sellafield (UK), BGE, BAM (both Germany) and ESS (Sweden) to improve and deploy its system. Lynkeos currently target nuclear waste decommissioning by deploying their muography system to categorise nuclear waste containers.

Nuclear waste decommissioning poses a challenge for the global industry in the next century, estimated to cost £250 Bn annually [8]. One pressing issue is the characterisation of waste storage containers which have been piling up since the beginning of nuclear power generation. There are tens of thousands of waste drums in the UK alone [8]. Lynkeos is tackling the issue of characterising waste material composition. Over seven years, Lynkeos developed the MIS, Figure 1.3, successfully identifying high-density materials such as uranium and lead within concrete-filled containers, Figure 1.3. The MIS has also been used to provide quality assurance for new waste encapsulation techniques, including assessing the homogeneity of samples after a thermal waste treatment process [8].

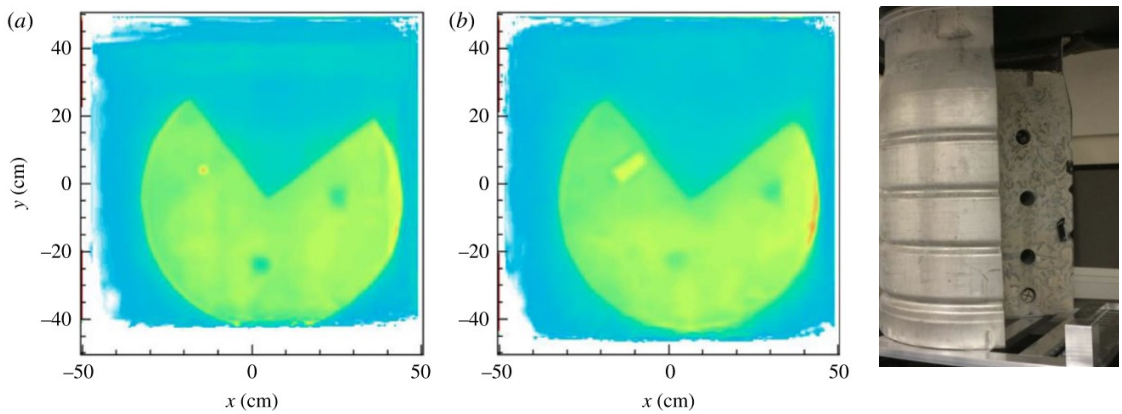

Figure 1.2 *– Results from Lynkeos MIS investigating a) uranium, and b) lead material encased within a concrete drum. Results show that the system successfully recognised the high-density material, c) decommissioned 500-litre concrete waste storage barrel*

Figure 1.3 *– Lynkeos muon imaging system (MIS) fully assembled at The University of Glasgow*

Lynkeos' MIS has proven the potential of muography within the laboratory and in a few permanent industrial locations. Lynkeos use scintillating muon tomography to image the internal density distribution with nuclear waste containers. To produce images, muons are first detected by scintillating fibres located in the detection planes. An event is recorded when fibres are excited by a muon passing through them, releasing a photon. The photon travels to the end of the fibre through total internal reflection. Photon events are recorded by photosensitive cells on silicon photomultipliers (SiPM) and converted to digital signals. The signals are then collected by front-end readout (FER) PCBs, which compare the time stamp of events between detection planes. Algorithms

are then used to compute the path traversed by the muon, allowing 3D images of the object to be produced [6].

While muography has been shown to be a capable imaging solution and the current design has proven successful in the lab, Lynkeos aims to realise the potential of muography on a larger commercial scale. Three limitations with the current design have been identified, image duration, detector design, and associated costs. Lynkeos has shown interest in leveraging new manufacturing techniques, such as additive manufacturing (AM), to enable widespread adoption of their technology into existing NDT markets.

1.4 Preliminary Work: 3D Printing Muon Detector Structures

An example of adopting AM practices into the fabrication of muography system structures was demonstrated by the 3DScint research collaboration (Swansea University and Lynkeos), funded by the EU ATTRACT scheme [9]. The work presented in this thesis directly builds upon the findings presented by 3DScint. This research designed a basic muography structure to house all components needed for muon detection. This work successfully demonstrated that 3D printing is a suitable manufacturing solution, capable of housing and protecting critical components. The prototype in Figure 1.4, printed all structural components for PLA using FDM. The prototype was designed to house two sets of 64 2mm fibres. The total detection area was 0.015m^2, and images produced had a resolution of 32x32 pixels.

However, while the preliminary work was successful at a small scale, no attempts were made to improve the commercial prospects of the system, i.e. scalability, assembly process, or robustness.

- The fibre spacing was large increasing the probability of missing muons traversing the detection area.
- The detection area was too small to be useful on a commercial scale, and no design considerations were taken to increase the detection area.
- The electronics were not integrated into the system extra fibre optics were used to route signals to external photo-sensitive cells.
- No considerations into material robustness to radiation were considered.

The design solutions presented in this thesis build upon the successes of the 3DScint design proposal while targeting the limitation that has been identified.
Specific novelties that are investigated in the designs proposed are:

- Incorporating modularity into the design to scale the detection area to meet customer requirements
- Incorporate new PCBs, supplied by Lynkeos, into the design to improve the compactness and mobility of the system.
- Investigate complex geometries possible with AM to improve fibre diameter, increase detection rate, and reduce print time and weight.
- Validating the material choice for robustness during operation.

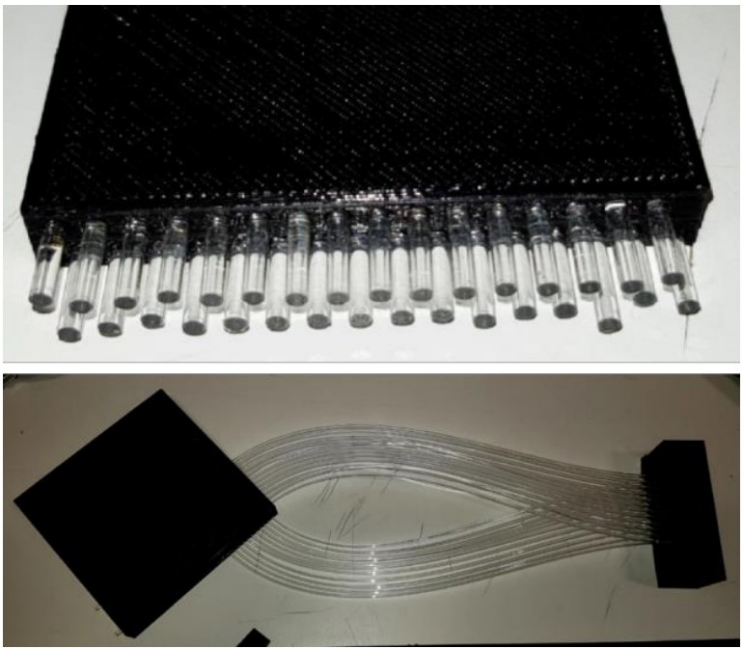

Figure 1.4 *– 3D printed muon detector structure by 3D Scint. 32 x 2mm fibres on each axis, giving 64 channels.*

1.5 Thesis Outline

The work presented aims to recommend design and material decisions that provide an improvement over the preliminary design proposed by 3DScint. Improvements have focused on scalability, mobility, and adaptability. Targeting these areas for improvement will increase the commercialisation of 3DScints proposal and guide future industrial-scale product design and material decisions for Lynkeos.

The thesis is laid out as follows:

Chapter 2 - Literature review

Initially, a literature review was conducted on muography to assess the current needs, applications, and hurdles related to the technology. The review discusses Lynkeos' current MIS system construction identifying the limitations with scaling, adapting and transporting. A discussion of the current manufacturing and material choices is presented.

The review of 3D printing focused on Fused Deposition Modelling (FDM). This review assessed the advantages, limitations, design practices, and manufacturing capabilities of additive manufacturing. The advantages of 3D printing are compared to the requirements to improve Lynkeos' MIS.

Finally, polymetric materials' response to gamma radiation was reviewed. Ensuring that AM materials chosen are robust to the radioactive operating environment in which the MIS is currently deployed is crucial. This review discusses the chemical mechanisms that radiation induces in polymers. Examples of industrial applications in which components are subject to gamma radiation sources are provided. The review then assesses previous work characterising the mechanical and chemical response of 3D printed parts to gamma radiation.

Chapter 3 – Housing Structure Design Process

A design process has been applied to the muon imaging system to identify design, manufacture and assembly improvements. The process first reviewed a preliminary 3D printed muon imaging system designed by 3D Scint. Limitations of the design proposal have been summarised in a design specification.

The research tasks undertaken in this thesis are shown in Figure 1.5. The initial task is to plan and determine the deliverables of the design process. This has been done in collaboration with Lynkeos with the outcome of the planning stage being a product design specification (PDS).

Following the PDS a novel design solution was proposed which focused on two key areas of improvement over 3DScints designs, namely integrated electronics and modular design. The solution was at The University of Glasgow to validate the design and cosmic-ray detection capability.

limitations with the novel design solution were identified compared to the design specification. To address the new limitations concepts for the fibre channels component have been investigated to improve the design and manufacturing. Prototypes of design solutions were fabricated and print runs were simulated to quantify material cost and time investment.

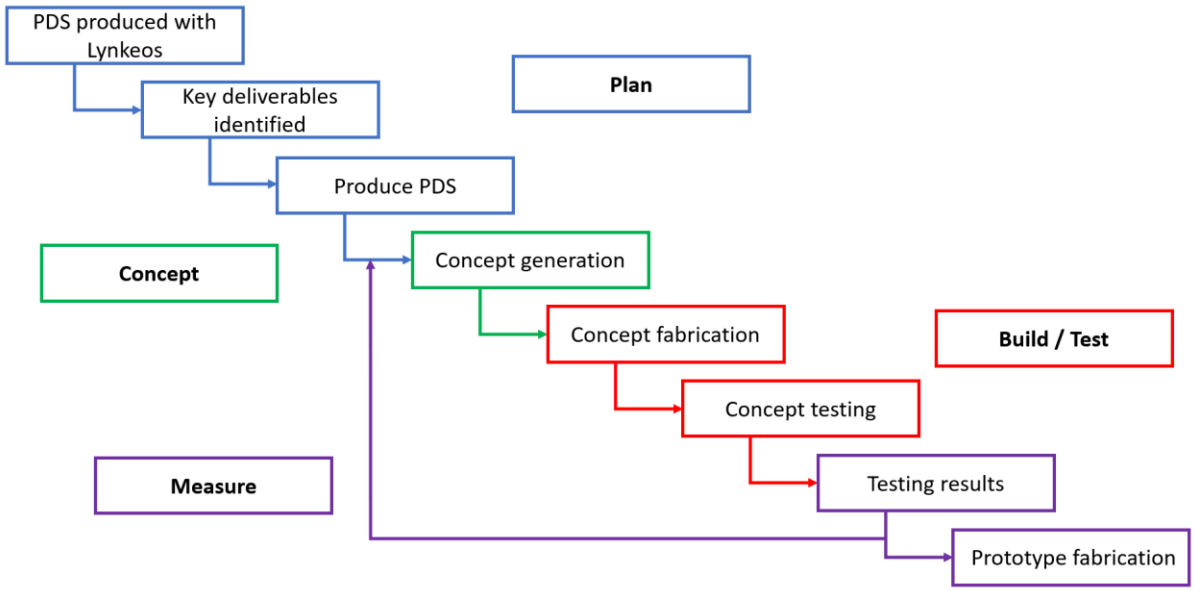

Figure 1.5 – *Design process methodology*

Chapter 4 – The response of 3D printed parts exposed to gamma radiation

The research then investigated the material selection. This was done to validate robustness to the current working environment Lynkeos deploys their system in, namely radioactive waste containers.

To simulate the operating environment of the MIS, 3D printed samples were exposed to high-intensity gamma radiation at The University of Manchester. This chapter follows an experimental methodology to assess the mechanical and chemical response of 3D printed samples when exposed to gamma radiation. Firstly, the materials and testing method are explained. Results from chemical and mechanical testing, as well as visual inspection, are provided. A discussion of results is then presented and linked to the impact of results for Lynkeos. Finally, a suitable material is selected for the additive manufacture of a new muon detection system.

Chapter 5 – Concluding remarks

The final chapter discusses the research questions and how the results presented have provided solutions to limitations with preliminary additively manufactured design proposals. The findings have been discussed in relation to the value and impact provided to Lynkeos and the wider community. Future research topics are provided to further enhance the results presented in this thesis. Finally, the future hopes for muography following this research are presented.

Chapter 2: Literature Review

2.1 Muography

2.1.1 Muography Overview

Similarly, to X-ray, ultrasound, and radar, muons can be used as an NDT solution. In contrast to other NDTs, muography uses cosmic rays to produce 3D density measurements of internal structures. These naturally occurring particles have been extensively studied since their discovery in 1936 by Neddermeyer and Anderson [10], who investigated and measured the energy of the particles occurring in cosmic ray showers. At 15km of elevation in the Earth's atmosphere, primary cosmic rays from sources such as supernovae interact with atmospheric molecules. These interactions cause the particles to undergo nuclear reactions creating a cascade effect that generates a *shower* of cosmic ray muons, classified as elementary particles [10]. The produced muons continuously bombard the surface of the Earth; on average, 600 passthrough a human body every minute. Muons are highly penetrating, with an average energy of 3GeV, over 10000 times to energy of a typical X-ray. This allows muons to penetrate hundreds of metres of rock [6] without damaging the object of interest. Furthermore, muography can be used for a wide range of application scales [6]. Additionally, due to the passive nature of muons, there are minimal health and safety considerations compared to other NDT such as X-rays [11]. Finally, the abundance of muons passing through the atmosphere makes muography a cheap and reliable method for internal feature identification.

When muons pass through matter, two measurable effects can be studied: (I) a loss in energy proportional to the amount of matter traversed (II) the incident direction is deflected due to multiple scattering from atomic nuclei [12]. These effects can be extracted to produce useful information. In general, the two methods of muon 3D imaging, namely *muon radiography* and *muon tomography,* are commonly classified as *muography*. In this thesis, muography will refer to the general application of muon 3D imaging. MR and MT will refer to muon radiography and muon tomography respectively.

Early applications of muography were based on the absorption of muons traversing a volume, effect (I). This is known as muon radiography (MR). Radiography effectively counts the number of muons that exit the volume of interest; assuming a known material composition, the thickness of the volume can be deduced or vice versa [13]. As the quantity of muons formed through interaction with the atmosphere is relatively constant, measuring the flux of muons after traversing a given volume allows measurements of the density variation within the volume to be taken. A ratio of incoming muons to

traversed muons can be calculated, providing insight into the material that has been traversed. Lighter materials like aluminium will have a larger ratio than heavier metals such as lead. MR has been used on larger scales to investigate the inaccessible interior of archaeological and geological landmarks such as pyramids, volcanoes, and seismic faults [5] [14] [15], as well as industrial applications in the mining industry [11].

Alternatively, Muon tomography (MT) measures the multiple scattering effect of the exiting muon to deduce the density of materials within the volume of interest, effect (II). This technique requires the vector measurement of incoming and outgoing muons through the volume. MT uses two high-precision, position-sensitive detector layers, above and below the volume, to measure direction vectors of both incoming and scattered muons. Measuring the locations allows the scattering angle of traversing muons to be calculated. Ultimately, three-dimensional images of the volume's contents are obtained [16] [17]. Historically, MT has been used on smaller scales to image the distribution of heavy metals or steel rebar encased in lighter materials such as concrete and fully loaded cargo containers [2][18][19].

Both imagining methods, MT and MR, have been successfully deployed in the industry. Depending on the application, MT or MR may be more suitable. Factors affecting the method may be the requirement for scale, resolution, the object of interest, and photon detection efficiency. The photodetection efficiency (PDE) is commonly used to quantify the probability that a charged particle traversing the detector will be recorded [20].

2.1.2 Industrial Applications of Muography

Whilst muography is still in the infancy of industrial application; there are examples of companies successfully deploying muon imaging systems in three distinct industries. These are:

1. Cargo scanning

Cargo scanning is a means of identifying smuggled nuclear material passing through national borders. Muon detection has successfully identified high-Z materials within 40-foot cargo containers [19]. Muography has been shown to scan an entire container within eight minutes [21]. Due to the passive advantage, companies have begun developing large-scale detectors for this application. Decision Sciences (USA), Lingacom (Israel), Muon Systems (Spain) and GScan (Estonia) are currently developing muon detection systems to identify contraband during border inspections. Despite this high

commercial activity, due to the short timescales required to obtain reliable information, the technique is not yet suitable for routine use for this application and more research is required.

2. Mining Exploration

The ability to visualise rock formations greatly interests the mining industry. Identifying economic mining locations is a costly expense. One traditional method of inspection is core drilling [11]. However, accurately categorising the internal makeup for rock mass requires many holes to be drilled. Other methods, such as seismic imaging and ground penetrating radar are used. However, these too have limitations in the measurement's penetration and resolution capabilities. As discussed, muons are highly penetrative, making muography an excellent choice for identifying high-density ore within low-density rock. Companies such as Lingacom (Israel), Ideon Technologies (Canada), and Muon Solutions (Finland) are attempting to realise the potential of muography in this industry.

3. Nuclear safety

As previously mentioned, the need to inspect nuclear waste for improved storage safety is growing. Previously published work has shown that muon detection is suitable for identifying nuclear material [22][23]. The only company applying muography to image nuclear waste is Lynkeos Technology (UK). They have successfully demonstrated that their system can produce high-resolution three-dimensional images of storage containers, the degradation of container integrity, and the waste materials within [8]. It is hoped that further technological developments will improve storage safety, reducing risks and costs associated with long-term storage.

2.1.3 Competing NDTs vs Muography

Competing NDT technologies such as radar, ultrasound and X-ray have historically been used for defect inspection, structural monitoring, and subterranean mineral identification.

However, these NDTs have disadvantages such as required resolution, high installation costs, highly trained professional operators, or safety concerns which limit the application of traditional NDTs. Furthermore, these NDTs rely upon short wavelengths for high resolution at the cost of penetrating depth [24] [25]. In contrast, muography does not depend on wavelength to achieve high resolution; the only loss in resolution at depth is due to a lower frequency of muons traversing the material [26]. However, as the NDT market is mature and existing technology has been widely adopted, muography must be demonstrated to be a commercially reliable and operationally robust technology if it is to disrupt the market.

2.1.4 Muography Detector Design

Since the first use of MT, many different detector technologies have been developed. Design variation depends on the detection technology deployed and the object being investigated. There are currently three predominant detection technologies [13].

(I) Nuclear Emulsion detectors (NED) were one of the first muon measurement devices deployed [27]. The path traversed by charged particles in these gel-based systems can be seen in Ag grains following chemical development. NEDs do not require any electrical input and can be compact and easily transported. However, no real-time information is available, and post-processing and secondary scanning equipment are needed to identify the muon tracks.

(II) Gaseous detectors, including drift chambers, resistive plate chambers and multi-wire proportional counters, are all filled with gas mixtures that become ionised when a charged particle passes through them [28]. Tracking is possible by recording which elements (e.g., plates or wires) are simultaneously ionised. Gaseous detectors are more challenging to maintain and control than other methods and require complex gas feeds or regular re-filling to operate. Most conventional gas mixtures are increasingly being banned in the UK.

(III) Scintillation detectors are the most used. These use plastic materials doped with a fluorescent material that produces scintillation photons when ionising radiation, such as a muon, passes through it. It is common to use orthogonally arranged scintillation fibres. The photons are then totally internally reflected (TIF) along the length of the fibre. The scintillating fibres are optically coupled to photon detectors at the ends. Photon detectors convert the light signal to an electrical current that is processed by a bespoke readout system. The most common photodetectors are silicon photomultipliers (SiPM) due to their cost effectiveness, efficiency, low power consumption, and robustness.

All detectors are designed for high reliability, operation in adverse environmental conditions, high PDE, and acceptable angular resolution. Due to the specification of design, detector structures are commonly bespoke. This limitation reduces the system's reproducibility, assembly, and maintenance, ultimately increasing the cost to companies.

This work will focus on scintillation detectors, the technology focus of Lynkeos Technology's development. Examples of scintillating detectors are presented in Figure 2.1. Most structures use

aluminium extrusion to support multiple layers of scintillating sheets to detect passing muons. Many of the detectors shown in Figure 2.1 are permanent installations with the exception of c, which was relocated around the volcano being inspected to produce 3D images and Ideon technologies, g), who have developed a borehole detector for the inspection of rock formations.

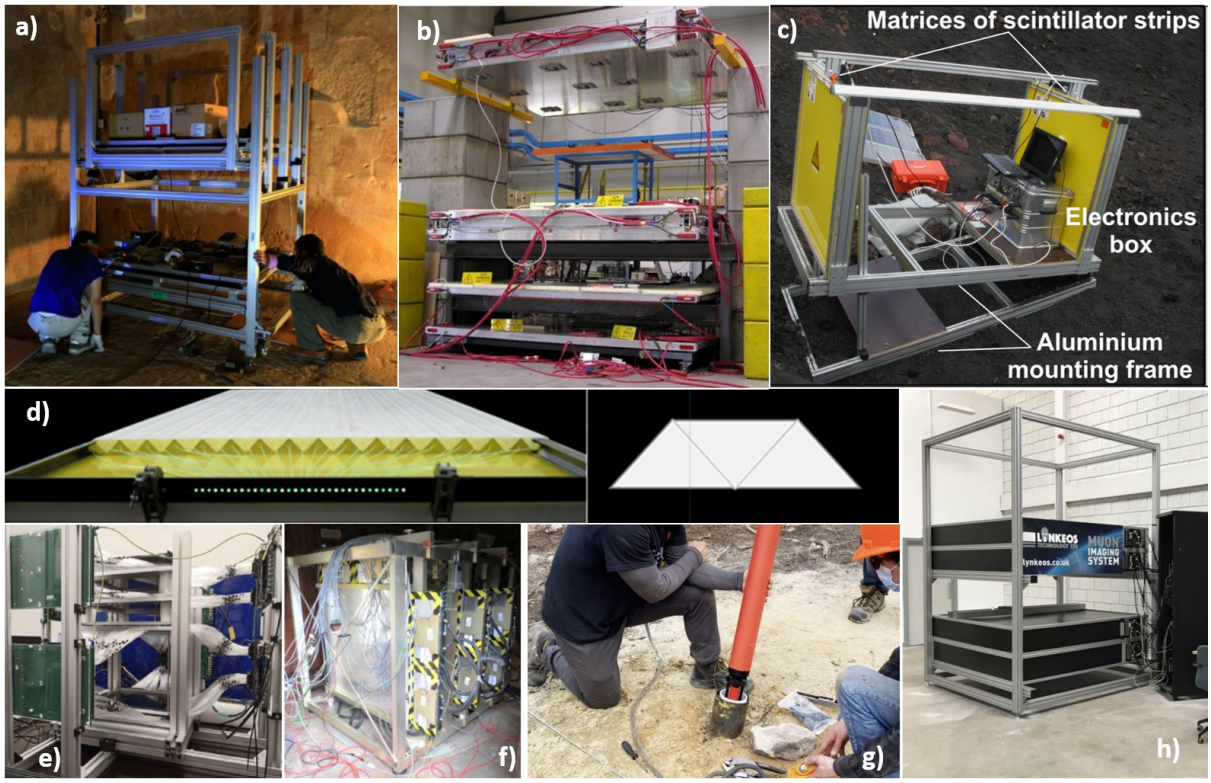

Figure 2.1 *– A selection of operational muon detector structures showing a) Muon radiography detector panels placed inside the great pyramids* [5] *b) INFN muon tomography demonstrator c) Muon Tomographic telescope imaging a volcano in Italy* [14] *d) Triangular scintillators used in the MURAVES detector*[29] *e) GScan's prototype muon tomography system, Estonia* [30] *f) ToMuVol, France* [31] *g) Ideon technologies borehole detector, Canada*[32] *h) Lynkeos technologies muon imaging system, UK* [7]

2.1.5 Lynkeos Muography Detector: Principle and Design

2.1.5.1 Working Principle

Lynkeos uses muon tomography to calculate the change in the path of muons as they interact with the object of interest. To achieve this, two layers of orthogonal scintillating fibres are stacked above and below the volume of interest, Figure 2.2. An event occurs when a muon traverses the scintillating fibre. A photon is produced, which travels to the end of the fibre through total internal reflection. The photon is converted into an electronic signal by a photosensitive cell positioned at the end of the fibre. The two layers of fibres allow an x and y coordinate to be measured; the separation

of the detection planes, the z coordinate, is known. By comparing the position of events in the top detection plane to the bottom detection plane, the change in path can be calculated using the multiple coulomb scattering principle. To ensure accurate and precise image reconstruction the fibres must have good locational stability and tight packing to increase resolution and detection probability. Stability, resolution and detection probability are essential considerations when designing the housing structure for the fibres.

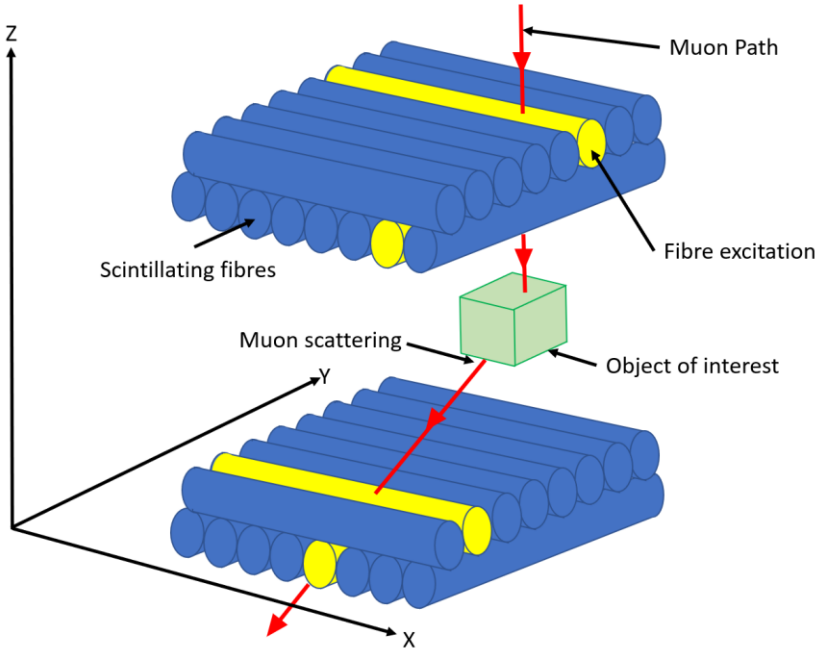

Figure 2.2 *–Working principle of muon tomography deployed by Lynkeos*

2.1.5.2 Design Aspects

The current muon imaging system (MIS), seen in Figure 1.3, uses four detection planes to calculate the path traversed by muons. Figure 2.3 shows a schematic diagram of one of these planes. The 2.1m^2 footprint of the current system is limited to a detection area of 1.5m^2. This is because space is required to connect scintillating fibres to external SiPMs, this is a limitation which was present in 3DScints preliminary design. The external SIPMS reduce the detector's volumetric efficiency and increases the number of parts and assembly time.

A primary objective of the research presented is to incorporate integrated electronics into the system. New SiPMs have been supplied to Lynkoes which removes the need for external SiPMs. The new SiPMs will directly interface with the scantling fibres in the detection plane increasing the spatial efficiency and removing the electronics section in Figure 2.3.

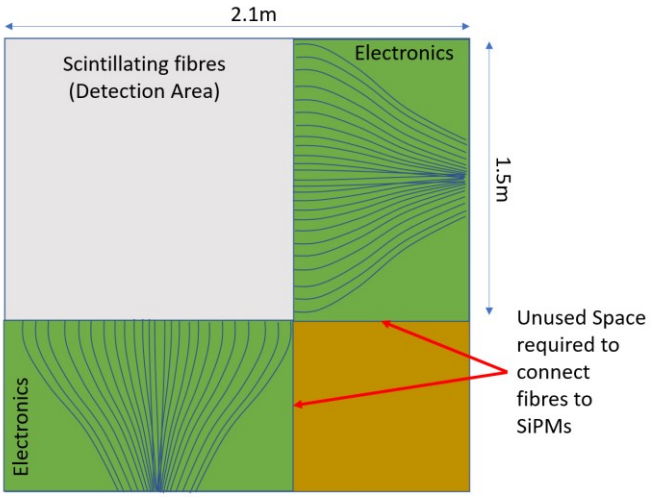

Figure 2.3 *– Schematic diagram of one detection plane from the MIS. The detection area is shown in grey, the area required for electronics is shown in green, and the unused area is shown in orange.*

Within the detection planes, fibre channels are fabricated from polystyrene sheets, Figure 2.4. The function of these channels is to support and position the scintillating fibres. A primary focus of the research presented is to investigate how the structure of the detection area can be improved by incorporating AM into the design and fabrication process.

The current methodology adopted by Lynkeos is as follows: Grooves are cut into the polystyrene sheets using CNC, and two layers of staggered fibres are stacked, figure 2.2, and secured with adhesives. On the opposite side of the sheet, similar grooves are cut in a perpendicular direction and a second layup for two staggered fibre layers is carried out.

There are issues with this method for securing scintillating fibres. Firstly, the fibres are installed permanently with adhesives, preventing the ability for reuse in other systems. This process is completed by hand and can lead to mistakes during assembly making the components hard to reproduce. The polystyrene sheets are also cut to size for the specific application and are not designed to be modular, meaning they are purpose-built and new sheets are required for every system. Finally, polystyrene is a delicate material, and care must be taken to transport and assemble the systems.

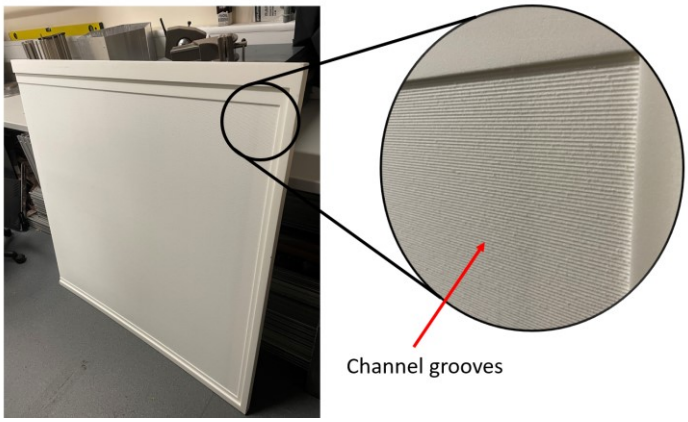

Figure 2.4 *– Polystyrene fibre channel component. Grooves for fibre alignment have been highlighted*

The discussion above has identified the constraints placed on new designs from a working principle perspective (stability, resolution, and detection efficiency) and a design aspect perspective (integrating electronics, removing the use of adhesives, and adaptability to meet customer needs). Addressing these limitations will reduce costs and help provide a competitive on-demand muon imaging business model.

2.1.6 Identified Limitations with The Existing Design

From the MIS and communication with Lynkeos, this thesis has identified three areas for improvement (A discussion on potential solutions to the limitation discussed above are presented in section 2.3.11) :

(I) Timeframe

Muography is limited by what nature can provide in terms of muons, around 170Hz/m^2. This leads to imaging duration taking days or weeks. There are two approaches to combat this limitation. Firstly, increasing the probability of detection, i.e. bigger detectors and more efficient systems. However, these solutions add costs to the system. Secondly, extracting more data from low muon frequencies using new statistical techniques, Machine Learning or combining muography with other imaging modalities, e.g., detecting neutrons produced in muon-induced fission. Detecting neutrons helps to improve the timescales for cargo scanning applications that need a decision in less than a minute to maintain the flow of commerce at ports. Muons alone would take too long to give a reliable measurement of smuggled nuclear contraband but detecting even one neutron from muon-induced fission is a non-ambiguous sign of fissile material present.

(II) Detector design and assembly

For the Lynkeos Sellafield system, the entire detector will need to be constructed on-site due to size limitations. Scaling up through modular design and better construction techniques will improve reproducibility, allowing commercial companies to invest in quality assurance within the product range. The assembly needs modularity but also robustness, as not all systems will be in an external frame in a controlled indoor environment. For future systems on a bridge, for example, systems must be lightweight and assembled quickly at height and in any weather condition.

(III) Cost

Currently, core system components are only used in high-energy physics experiments. Scintillating fibres are approx. £25 per fibre, each system requires around 10,000 of them to ensure high spatial resolution. Silicon photon sensors are similar and price and require one sensor per fibre. Regarding electronics, the Front End Readout (FER) cards cost around £7000 each – one per 64 fibres. For permanent installations, the customer pays for the entire system. Spares of core components are required for any repairs or maintenance – it is typical only to repair a single silicon PCB or FERS; fibres are very rarely in need of replacement. For permanent systems, adhesives can be used to bond fibres in place. However, for future systems using an on-demand service business model, there is a need for a planar system to image bridges or borehole systems for subterranean inspection. Reusing fibres, silicon sensors, and FERS in different holding structures would reduce overall component and material costs. Adaptable detector designs with the ability to reuse components are of high importance to Lynkeos, who would then be able to offer a more competitive rental/service price to customers.

2.1.7 Muography Conclusion

While still in the early adoption phase, muography has already shown advantages over competing NDT technologies such as radar, ultrasound and X-ray. The primary advantages are that muons are highly penetrative, entirely passive and non-destructive – reducing safety considerations for operators.

Muography has been shown to be a highly useful technology with a host of advantages over traditional techniques. Alternative NDTs can not compete with the highly penetrative properties of muons, making them a powerful imaging tool. Researchers are keen to advance the technology for deployment in untapped markets, such as civil structure monitoring. However, this will require advancements to the physical system to reduce the cost and improve the mobility of the technology.

2.3 An Overview Of Additive Manufacturing

2.3.1 Introduction

Additive manufacturing (AM), commonly referred to as 3D printing, is a rapidly growing area of research and has exploded in popularity in recent years due to a significant increase in accessibility. This rapid increase in popularity has driven extensive research into the field, leading to frequent advancements in the efficiency, performance, materials, and cost of additively manufactured parts.

AM is a layer-by-layer fabrication method, selectively depositing materials in locations specified by a digital file. While AM was initially envisioned as a rapid prototyping (RP) solution, advancements in the deposition method and materials available have improved the accuracy, material properties, and cost of AM parts, allowing AM to be deployed in the field as functional parts. This is possible due to advancements in AM technologies. In 2018, a survey conducted by Sculpteo investigated the growth in the adoption of 3D printing across eight sectors [33]. The result was overwhelmingly positive towards 3D printing, with more investment, applications and impact being generated through 3D printing.

Additive manufacturing (AM) was first patented in 1984 [34], for the rapid prototyping of parts. This is the first example of Stereolithography (SLA) which selectively cures photosensitive resin, building layers on top of each to fabricate the desired geometry. Following this patent in 1989, a new form of AM was patented, selective laser sintering (SLS)[35]. SLS uses high-intensity lasers to selectively fuse polymers powders forming a three-dimensional object. During this time, a third method was developed: fused deposition modelling (FDM), which melts and extrudes polymers to form geometries [36].

AM can be defined as the fabrication of parts from a digital model through additive layer-by-layer material deposition. The deposition areas are determined by a digital file, which is why AM is typically classed as a digital manufacturing technique. The numerous AM process allows for a wide variety of materials to be used for fabrication. The method of deposition and material deposited varies based on the application.

Broadly, manufacturing markets are shifting away from mass production and into customisable and personalised products that are growing in popularity [37]. For Lynkeos, AM appears to be an obvious choice for the development of bespoke Muography systems. The required components have complex internal geometries which are difficult to form using traditional methods. AM also offers excellent flexibility in production allowing components to be adapted and scaled without the need for tool

changing. Finally, AM can utilise the broad range of materials available to ensure mechanical robustness during operation and transport expected for onsite cosmic ray imaging systems.

2.3.2 Types of AM

The ASTM standard F2792-12a [38] lists seven classifications of AM: Binder Jetting, Direct Energy Deposition, Material extrusion, material jetting, powder bed fusion, sheet lamination, and vat photo-polymerisation. The classification will depend on the application, which influences the available materials. These classifications can be broadly split into three phase types; Liquid-based, Solid Based; and Powder-based [39], Figure 2.5.

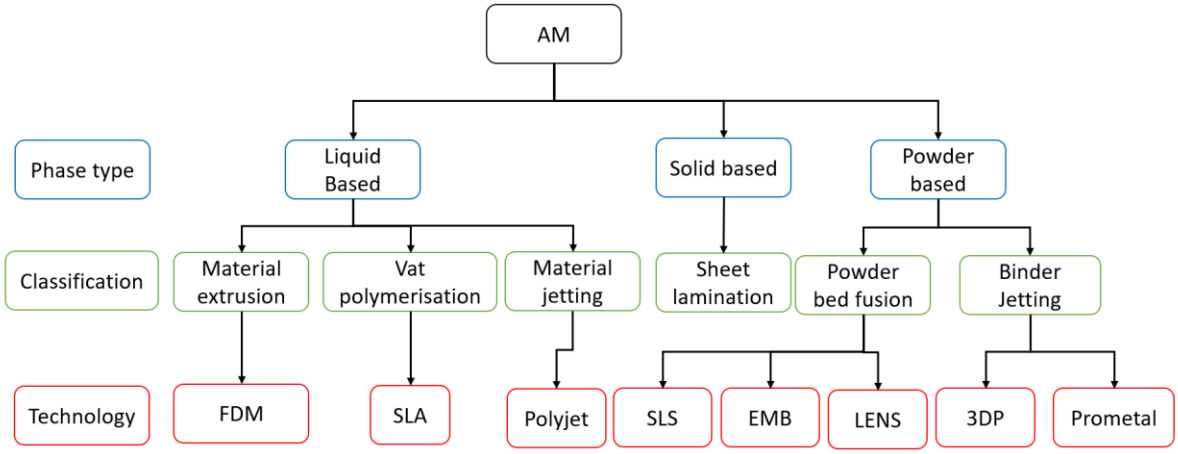

Figure 2.5 *– Flow chart of AM technologies. Phase type - starting material phase. Classification - the method of depositing material. Technology - examples of specific technologies within the categories mentioned above*

A description of the types of processes and applications presented in Figure 2.5 are discussed in the appendix.

2.3.3 AM Technologies Investigated In This Thesis

There are many types of AM processes, all with unique strengths; depending on the application's requirements, a suitable process can be selected. For the work presented in this thesis, FDM and SLA have been chosen to be investigated for the fabrication of the muography system components. Preliminary work by 3DScint has already demonstrated the feasibility of using FDM to

fabricate the fibre housing component. FDM is a good choice for the fabrication of the components as the available materials are cheap and lightweight. Additionally, the operating conditions for the muography system are not expected to be exposed to thermal cycling, so temperature resistance is not of great concern. FDM can also produce net shape parts minimising postprocessing operations and reducing the assembly time of the detectors. While FDM parts are weaker than other AM processes, the printed muography components are not expected to receive excessive loading during operation. Finally, the resolution of FDM has been deemed acceptable to house components of the required dimensions. SLA has also been chosen for investigation. While SLA is more expensive, the part strength is higher when compared to FDM. SLA can also produce significantly higher resolution parts which may prove beneficial for geometrically complex holding structures. However, it is unclear if the benefits of SLA in strength and resolution outweigh the added costs and the necessary post-processing step.

2.3.5 An Overview of Fused Deposition Modelling (FDM)

Figure 2.6 labels a commercially available FDM printer and components. FDM uses a spool of material (typically 1.75mm in diameter) that is fed into the hot end. The hot end contains a heating unit, a nozzle (typically 0.4mm), and a stepper motor that pushes material into the hot end at a specified speed to achieve the desired flow rate. Depending on the material used, the hot end and bed temperature can be set to the desired temperature. The geometry is fabricated by moving the hot end in x and y to create cross-sections of the part. The hot end is then moved upwards in the z-direction, and the next cross-section is deposited. By repeating these steps, the completed part is created.

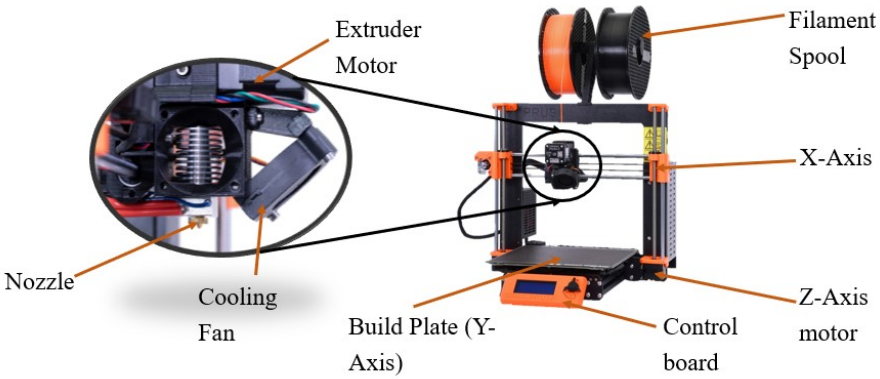

***Figure 2.6** –Diagram of a Prusa i3MK3 (standard FDM printer). Components have been labelled*

FDM uses a digital computer-aided design (CAD) model which is *sliced* into layers. During the AM process, layers are additively applied on top of each other to create the final part. This differs from

traditional manufacturing techniques where the material is subtracted from unprocessed bulk material, leading to excessive waste material.

The desired part is typically created as a CAD file, which is then converted into a stereolithography (.STL) file, approximating the geometry for the CAD file as triangles. The .STL files can then be sliced using the software. Slicing transforms the 3D geometry into a list of commands the printer can execute. The output from the slicing program is called the G-Code. For example, G-Code in FDM printing contains information such as Tool path, Layer height, Hot end temperature, Bed temperature, Flow rate, Retraction speed, and travel speed. The G-code can also contain geometrical changes during the slicing process. Material addition during the slicing process, such as support structure and build plate adhesion, improves print success rate or dimensional accuracy. Using the information from the G-Code, the printer can execute commands and fabricate the initial CAD part.

2.3.6 FDM Materials

Since the conceptualisation of FDM by Scott Crump in 1988, advancements in materials research have improved the properties of parts that can be printed using FDM. Extensive research has been carried out into polymers and composite polymers to meet industrial needs [40] [41]. The work presented in Chapter 4 focuses on base polymers. However, investigating the mechanical response of polymer when exposed to gamma radiation, may be transferable to composite FDM materials. The base polymer matrix material remains in composite parts and will require robustness to operate under radioactive conditions.

Polymers

Initially, FDM printing was designed for thermoplastics utilising the low melting point. Acrylonitrile Butadiene Styrene (ABS) was the dominant polymer used in 3D printing [42]. However, there are many shortcomings with this material. Such as the large deformation observed during cooling, leading to warping and cracks forming within the structure. ABS also releases toxic fumes when heated, creating health and safety risks. In recent years, polylactic acid (PLA) has been commonly used in FDM due to the ease of printing, good overhangs and low printing temperature. New thermoplastics such as Polyethylene terephthalate glycol (PETG), Acrylonitrile styrene acrylate (ASA), and Polyether Ether Ketone (PEEK) are more frequently used due to improvements in toughness, resistance, and appearance of parts.

Particle-reinforced polymer composites

Particle-reinforced polymer composites use powdered additives and a polymer matrix to reinforce the material. Different additives can be added to the matrix to enhance specific properties. Additives can include aluminium [43], iron [44], barium [45], and tungsten [46]. Depending on the additive, properties such as strength, flexibility, thermal conductivity, wear resistance, and toughness can be improved. Metal particle reinforced polymer composites can either be partially metallic, where the polymer remains in the final part. Conversely, the polymer matrix can be sintered to produce nearly 100% metal parts.

Polymer Ceramic Composites

Polymer ceramic composites or biocomposites are particularly useful in biomedical applications. These composites are biocompatible and extremely resistant to corrosion and temperature. Common additives are TiO_2, ZrO_2, Al_2O_3 and calcium ceramics [47].

Fibre Reinforced plastics (FRP)

FRPs are commonly used in high-strength, low-weight applications such as the aerospace industry. The most common types of FRP in the aerospace industry are carbon fibre-reinforced plastic (CFRP) [48] and glass-reinforced plastics (GFP) [49]. However, due to environmental concerns, research is actively searching for a natural fibre replacement to replace carbon fibre.

The literature shows clear benefits to combining 3D printable polymers with additives. Depending on the application's needs, numerous properties can be improved.

2.3.7 Printing Parameters in FDM

Print paraments will have a significant effect on the properties of the final part. Depending on the application, parameters can be set to improve strength, reduce print time, or improve accuracy. However, these effects are not independent; typically, optimising for one property will alter another. For example, a smaller layer height could be used for better dimensional accuracy but increases the print time. A review of the mechanical effects of changing print parameters is presented in section 2.3.8. The parts designed in this thesis (Chapter 4) require good mechanical robustness to survive transport and operational stresses. A good resolution to accurately house the electronics and good bridging characteristics. While weight and print time are not critical considerations, reducing these variables will inevitably improve overall production and transport and operation.

Infill

Infill is the percentage of the internal volume that is filled with material. This parameter directly affects the relative tensile strength of the part as more material leads to tougher and more robust parts. The percentage is not the only factor determining infill; infill geometry can also significantly affect anisotropic properties, Figure 2.7. Higher infill per cent leads to stronger parts due to increased part density. However, higher percentages will increase the print time. Different infill types can improve strength and anisotropic stiffness.

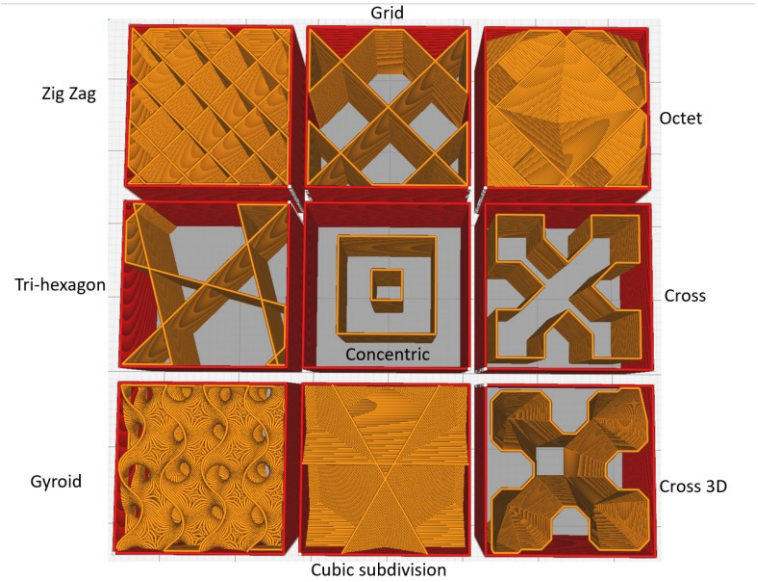

Figure 2.7 *– Examples of infill types at 10% infill*

Print orientation

3D printing is inherently anisotropic as the z-axis relies on layer adhesion for strength. Good 3D printing practices reduce the use of the z-axis, opting to print in a horizontal orientation. Reducing the use of the z-axis reduces print time, increases strength, and improves the success rates of prints. Examples of the same object with three orientation is shown in Figure 2.8.

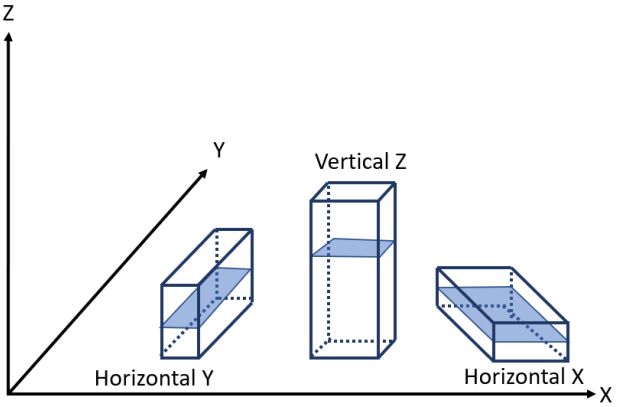

Figure 2.8 *– Examples of print orientation relative to build plate*

Nozzle and bed temperature

The temperature is used to melt the filament in the hot end. Commonly suppliers provide a suitable range of temperatures for the filament to be printed. Higher temperatures can lead to better layer adhesion. However, high temperatures will lead to overhangs sagging and a reduction in dimensional accuracy. Bed temperature is used to incentivise bonding to the build plate during printing. After fabrication, the bed temperature is reduced, which releases the part from the bed. Typically, material suppliers will provide recommended bed temperatures, Figure 2.9.

Layer height

Layer height sets the z-axis distance between layers. Thick layers will reduce print time at the expense of surface finish, Figure 2.9.

Nozzle width

The width of the nozzle determines the resolution of the part in the x-y plane. Typically, nozzles are 0.4mm in diameter. However, nozzles ranging from 0.2 to 1.2mm are commercially available depending on the application, Figure 2.9. Reducing the nozzle width allows for higher resolution parts at the cost of increased print time.

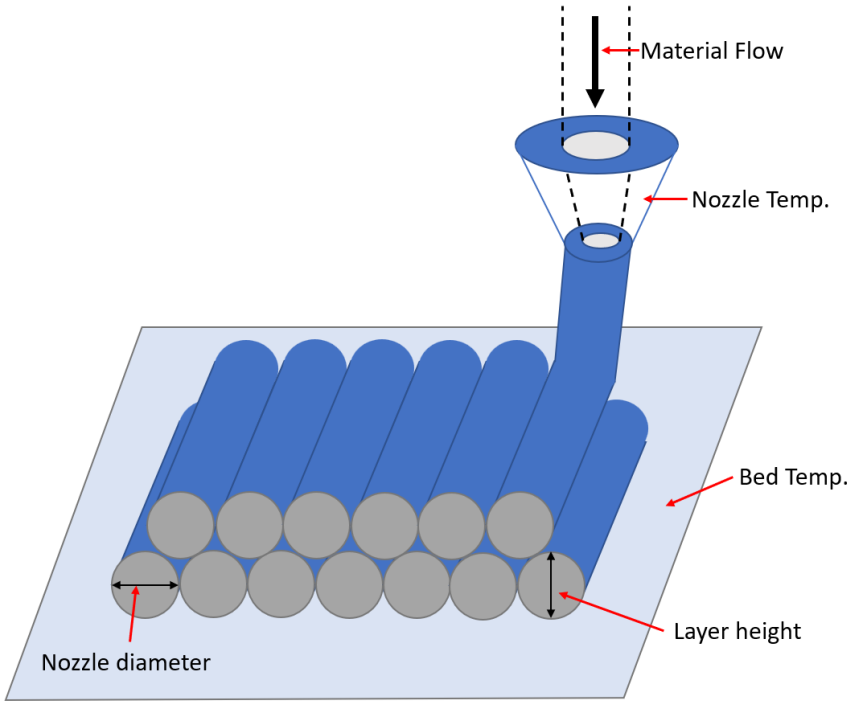

Figure 2.9– *Diagram of the printing process. Print parameters have been labelled for reference to the text.*

Raster orientation

Raster orientation is the direction of the bottom and top layers. Changes to the raster orientation can affect tensile strength and lead to anisotropy in part, Figure 2.10.

Fan speed

Fan speed determines the cooling of the filament just after extrusion from the hot end. Higher fan speeds will improve dimensional accuracy and overhangs. However, it will reduce the layer adhesion as the material can cool too quickly.

Walls

The walls are defined as the number of outer shell lines printed on the layer's perimeter, Figure 2.10. Using more walls will increase the part's strength as walls are printed with effectively 100% infill. However, more walls increase the print time.

Build plate adhesion

Build plate adhesion is a slicing operation that reduces warping and improves adhesion to the build plate. Typically, there are two forms of build plate adhesion. Brims are external contours printed on the first and promote adhesion to the build plate, Figure 2.10. Rafts are printed structures below the part; these are used when there are details or features on the bottom surface that will require support material.

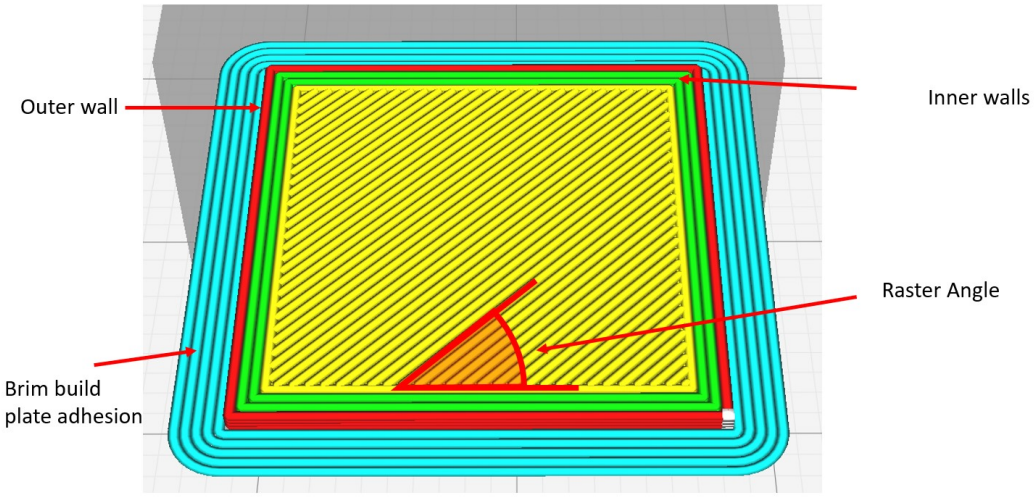

Figure 2.10 *– Diagram of the sliced cube. Printing parameters have been labelled for reference to the text.*

2.3.8 The Effect Of Print Parameters On The Mechanical Properties

G-Code optimisation and printing parameter selection have become active areas of research in academia. This is because how the material is deposited can significantly affect the material properties of the final piece [50,51].

Commonly used slicers such as Cura, Repetier Host, and Prusa slicer are continuously updated with the latest advancements in slicing software. These improvements aim to give the designer greater control over the fabrication process. There has been extensive work into the effect changing printing parameters can have on the properties of the final part [51–55]. Printing parameters can affect mechanical properties differently depending on the material being printed.

Algarni et Al. [56] conducted a comparative study across numerous published papers, identifying parameters that affect the following mechanical properties: Young's modulus, UTS, flexural strength and elongation at break.

For PLA, the most significant parameter is the infill percentage. The raster angle significantly affected the UTS and elongation at break. While infill speed affected the flexural strength

For PETG, infill percentage was the most significant parameter when comparing Young's modulus and UTS. Layer thickness had a noticeable effect on UTS and flexural strength. Again, infill speed was the most significant for flexural, and raster angle influenced the elongation at break.

For ABS, infill percentage had the most influence on all mechanical properties, with raster angle and layer thickness having a notable influence on Young's modulus, UTS, and elongation at break.

The review suggests that the dominant factor in determining mechanical properties is infill percentage which has the greatest effect on mechanical properties and other parameters such as raster angle and print speed play significant roles in the mechanical performance. However, there is a considerable variation in the results obtained from the collated papers, with some contradictions between papers. This is most likely due to a lack of standardisation in the AM space and a lack of details covering print settings. That being said, while the study does identify key parameters that affect mechanical properties, parameter settings are not the only consideration when fabricating with AM. During the AM design process, it is important to consider features, orientation, and assembly steps to ensure successful, time and material-effective prints.

2.3.9 Design Processes

Design processes are used to tackle large projects by systematically breaking down the project to address requirements. Using a design process improves creative problem-solving without relying on inspiration. Project goals are defined through a criterion which influences design decisions. Creative solutions are then generated in line with the criteria. Design processes typically deploy a type of feedback, with continuous improvements driven through iterative testing and analysing.

Design processes are generally split into four phases:

Plan – This is the data collection phase of the process. Research is conducted into the target audience, existing solutions, and the needs and constraints of the project. Ultimately the task is defined by recognising specific outcomes that need to be achieved.

Concept – This phase considers a variety of solutions to meet the required outcomes. Research from the planning phase, brainstorming, and sketching incentivises idea generation. Ideas can be combined or trimmed depending on the fit to the defined project goals.

Build / Test – This phase is where the concepts are physically formed. This gives insight into the manufacturability and performance of the concept. It is typical for this phase to be iterative, looping back to the concept phase after testing.

Measure – Once the design has been finalised, it is essential to measure the project's success using the goals originally defined in the planning phase. There may still be minor issues at this point which can be addressed. So long as the project achieves the predefined goals, it has been a success.

It is essential to define the project's goals clearly and concisely during the planning phase. The project goals influence concept generation, testing, and the measurement of success.

2.3.10 - 3D Printing Design Principles

Since its inception, additive manufacturing has matured as a technology. Advancements have been pushed by the increased interest from the private and public sectors. There have been efforts to produce frameworks for designing with AM utilising the advantages of the manufacturing solution. Such frameworks have been produced to allow for innovation, improve the success of prints and increase the efficiency of part fabrication.

Frameworks such as the 'Design innovation with additive manufacturing [57] extracted 23 design principles from existing online design repositories. For the work in this thesis, ten related principles have been extracted and summarised in Table 2.1.

These principles provide an early indication of successful designs with AM. The novel design solution presented in Chapter Three has been influenced by these principles; notably modularity (#23) and standardisation (#21, #22) are directly applied to the novel design proposed. These principles help address the limitations of scaling, assembling, and integrating electronics.

Further design improvements investigate the effect of orientation (#1, #4, #10, and #12) and cellular structures (#5) these improvements address weight, print time and accuracy.

Table 2.1 Design principles adapted from [57]

No.	**AM Design Principle**
1	Print small features without the use of support and in an appropriate orientation
4	Print success can be improved by printing with the lowest vertical aspect ratio
5	Cellular structures can be used to improve weight, cost and strength
10	Improve print time by orienting with the lowest vertical aspect ratio
12	Improve the accuracy of critical features by orientating in the axis with the highest resolution
18	Consider the resolution of AM process during designing
21	Standardise assembly process
22	Standardise interfacing joints
23	Divide larger pieces into multiple smaller pieces

2.3.11 How 3D Printing Can Address Challenges Facing Muography

As previously mentioned, Lynkeos has shown an interest in incorporating AM into the manufacture of their MIS. It is hoped that the previously stated hurdles constraining wide-scale technology adoption will be improved using AM. Specifically, AM hopes to address challenges (II) and (III) set out in Section 2.1.6.

(II) AM offers solutions to improve the scalability and reproducibility of the design and assembly process for Lynkeos' MIS.

a) Due to constraints with installation, new systems require the ability to be assembled on-site. AM offers modular design solutions, allowing for flexible scaling systems to meet customer requirements. Modular design also improves the onsite assembly process, improving assembly in adverse conditions, i.e. at height inspecting civil structures such as bridges.

b) As AM is a computer numerically controlled (CNC) technology, there is a high degree of automation in the fabrication process. This reduces the need for manual labour, ultimately providing quality assurance to the customer and minimising human error during fabrication.

c) AM offers many material choices, which allows tailoring robustness to numerous adverse operating environments, i.e. weathering, thermal cycling, and ionising particles.

(III) Costs

AM can provide cost reduction to future business models such as on-demand servicing using muon imaging.

a) AM is a flexible manufacturing solution capable of fabricating complex parts without requiring expensive dies. This reduces associated costs with bespoke structures by allowing rapid fabrication for specific applications such as planar and borehole detectors.

b) The scintillating fibres are a high cost of Lynkeos' MIS. Fibres, which are currently permanently installed with adhesives, cannot be reused. Fabricating complex geometries with AM provides opportunities to install fibres temporarily. This allows the repurposing of fibres for new system designs, recycling fibres from older systems.

c) Currently, polystyrene grooves used to house the fibres are a one-time fit. For new detectors, AM offers the ability to scale the detector to meet the needs of the customer without the costly process of redesigning and reproducing.

2.3.12 Additive Manufacturing Summary

To conclude, AM is vital in many of today's vital industries. The capabilities of AM are driving costs down whilst improving innovation at the design level. Similarly, Lynkeos hopes to leverage the advantages of AM to gain a competitive edge over the market. Specifically, the capability to fabricate complex geometries reduces the need for extra parts and assembly steps. Modular design allows for flexible scaling specific to the application and can improve the on-site assembly. Furthermore, there is no requirement to mass produce more than 100 detector planes. This makes 3D printing an excellent economical choice. Finally, the numerous material options available allow for strength, weight, and robustness to be assessed to meet the customer's requirements.

2.5 The Response Of Polymers To Gamma Radiation

2.5.1 Introduction

A key application area for Lynkeos is investigating the distribution of radioactive waste within concrete barrels. This means their muography system is subject to gamma radiation Research has indicated that equipment operating near spent fuel cells could be exposed to radiation up to 5500 Gy/day [58,59]. It is well documented in the literature that radiation exposure will degrade polymetric material. If the structure of the system is 3D printed with plastics, it is of interest to understand the response of 3D printed materials when exposed to gamma radiation.

The effect of gamma-ray radiation on polymers has been well-documented for over 30 years. In 1994, Mohamad and Ariston [60] explained that the primary mechanisms in polymers exposed to radiation are cross-linking and chain scission. Cross-linking forms a three-dimensional polymer network, ultimately increasing molecular mass with radiation exposure [61]. This occurs through free radicalisation, which induces oxidation and ultimately leads to the embrittlement and degradation of the material [62]. In contrast, chain scission occurs through the breaking of long polymer chains. Chain scission reduces the molecular weight and leads to the material softening and loss of elastic properties. Many factors can affect the resistance to radiation including molecular structure, temperature, dose rate, and dissolved oxygen.

2.5.2 – Applications Of Irradiated Polymers

From a broader perspective, there is a growing interest in deploying Fused Deposition Modelled (FDM) parts in environments subject to gamma radiation. A few examples of these applications include the sterilization of surgical equipment [40,63–65], deployment of robotics in the nuclear industry [66,67], and flexible manufacturing during space missions [68][69]. As interest in additive manufacturing (AM) in these sectors continues to grow, it will become important to understand the chemical and mechanical response of 3D printed materials exposed to high radiation levels. Extensive research has been carried out into the effect of printing parameters on the mechanical properties of parts [53][52][55][56]. It has also been shown that 3D printed parts can have a controlled porosity by how the material is deposited, making them geometrically different to bulk materials and changing the nature of oxygen diffusion through the part [70]. This is a design aspect that may well influence the response to radiation.

The magnitude of radiation exposure varies between applications. A typical unit of measurement for radiation exposure is the Gray [Gy], where one Gray [Gy] is a unit radiation dose equivalent to a joule of energy absorbed per kilogram (or 100 rad) [71]. Depending on the application and duration of deployment, the range of dosages experienced by people and apparatus will vary substantially. Example dosages for specific applications are listed in Table 2.2. These vary from an upper extreme in applications such as nuclear incident clean-up or operating in the vicinity of spent nuclear fuels, which will amount to over 2MGy after a year of operation. Additionally, in the medical industry, polymeric medical devices are typically sterilised to 25kGy. However, the cumulative nature of radiation can lead to a rapid rise in total exposure over an extended lifetime with multiple sterilisations. Finally, the lowest doses are from ambient exposure during space travel.

Table 2.2 Examples of industry-based applications exposed to gamma radiation and typical exposure rate

Industry	Application	Dose (Gy/day)	Reference
Space exploration	Round trip to Mars	0.002	[72]
	Previous space missions	220μ -1270μ	[73,74]
Sterilisation of polymeric materials	Poly(vinyl chloride) - Food packaging Poly(methyl methacrylate) – medical supplies Polycarbonate - Engineering resin	25000 / sterilisation	[65,75]
Nuclear	ROV clean-up and maintenance at Fukushima	24000	[67,76]
	Operating near spent fuel cells	5500	[58,59]

2.5.3 Irradiated Polymers in Industry

The dominant chemical mechanisms in irradiated polymers are cross-linking and chain scission. While these processes will degrade the polymer in large quantities, research has suggested that radiation-induced chemical changes can be advantageous to some properties if adequately controlled. For example, irradiation of polymers has become standard practice in the chemical industry [61], becoming the preferred method for many key chemical processes such as polymerisation, grafting, and curing. This is because the purity of the material can be maintained as no catalysts or additives are required. Additionally, crosslinking has improved poly(vinyl alcohol)'s thermal and mechanical properties [77]. Furthermore, radiation has also been used in the Biomedical, Electrical and Textile industries to improve the performance of the products [61]. Finally, regarding 3D printing, radiation has been used to reduce the inherent anisotropy of 3D printed parts by inducing crosslinking across layer boundaries [78].

2.5.4 – 3D Printed Parts Response To Radiation

Investigating 3D printed parts subject to gamma radiation, Wady et al. [70] concluded that the rate of oxygen diffusion, which is determined by the porosity, can be controlled through printing parameter optimization, specifically infill percentage and orientation, which directly affects the diffusion coefficient [70][79]. By controlling the rate of oxygen diffusion within the microstructure, optimisation of the radiation-induced chemical process is possible, with higher oxygen levels promoting chemical changes. This conclusion indicates that the radiation-induced chemistry occurring within the 3D printed parts will differ from the chemical changes observed in polymers manufactured with traditional methods. Emphasising the importance of understanding how the response of 3D printed parts differs from bulk material.

Research into the mechanical and chemical changes within 3D printed parts following exposure to gamma radiation has been steadily increasing since 2016. However, the range of materials investigated is limited. Previous research has focused on Polylactic Acid (PLA) and Acrylonitrile butadiene styrene (ABS); historically, these have been the most commonly printed and commercially available materials (Table 2.3). However, PLA has shown to be hypersensitive to small radiation dosages, making it unsuitable for many long-life operations exposed to radiation. While ABS has demonstrated more robustness to gamma radiation, ABS is difficult to print compared to other material options available today. To print ABS actively heated chambers are required to reduce warping and cracking. In addition, a fume cupboard is needed to remove toxic gases when heated. Previously published work on the response of the mechanical properties (ultimate tensile strength (UTS), maximum strain, Young's modulus, and hardness) of PLA and ABS have been summarised and provided in Table 2.3.

Table 2.3 Changes in mechanical properties of PLA and ABS as a result of gamma radiation exposure

Material	Dose (MGy)	Percentage of the mechanical property remaining after gamma irradiation compared to control samples				Reference
		UTS	Max. strain	Youngs modulus	Hardness	
PLA	0.03	69.5	62.7	129.5	N/A	[80]
	0.05	83.8	44.0	103.5	101.3	[71]
	0.15	16.8	8.5	110.7	103.9	
	0.2	7.2	3.7	114.3	105.2	
	0.3	7.6	NA	78.2	N/A	[70]
ABS	0.01	102.9	109.7	107	101.4	[81]
	0.015	103.5	106.9	109	105	[82]

	1	28.8	9.8	122.9	110.3	[81]
	1.4	21.6	4.8	126.8	112.2	
	2.6	37.5	N/A	101.6	N/A	[70]

From Table 2.3, PLA has shown significant degradation in the UTS and maximum strain for exposure levels above 0.05 MGy. Increases in Young's modulus and hardness were recorded up to an exposure of 0.2 MGy Findings from [71] measured increases in Young's modulus and hardness. The authors attributed initial changes in the mechanical properties to cross-linking. In contrast, the findings from [70] measured a decrease in the Youngs modulus of PLA at a similar exposure level, 0.15 MGy. The authors attribute this to the decrease in glass transition temperature and increase in the viscosity of the material due to heating during radiation. This discrepancy between results could be due to the difference in dose rate applied to PLA, 1 kGy/h [71], 6.2 kGy/h [70]. Both papers conducted Fourier transform infrared (FTIR) analysis on the PLA samples. However, few similarities can be drawn between the results. Findings from [71] measured increases in peak intensity up to exposure of 50kGy. This paper also observed a formation of a peak between 3200 and 3550 assigned to the O-H stretch, hypothesised to indicate crosslinking, and new peaks appearing at 1660, 1560, 1492, and 1424 cm^{-1}. However, findings from [70] make no mention of the formation of a new peak, only recording increased intensity in all peaks present before irradiation. Finally, [70] recorded the molecular weight loss and concluded that chain scission is the dominant mechanism in PLA, evidenced by the formation of volatile organic compounds.

From Table 2.3, ABS has shown higher mechanical robustness to gamma radiation, with samples subject to exposure above the maximum PLA dose of 0.3 MGy. At doses lower than 0.05 MGy, slight increases in UTS and maximum strain were observed by [81] & [82]. However, at dosages over 1 MGy significant decreases in UTS and maximum strain were recorded [70] & [81]. The literature referenced in Table 2.3 recorded increases in the Youngs modulus and hardness at all gamma radiation exposure dosages. FTIR was carried out in [70], and it was concluded that cross-linking is dominant at lower exposure levels due to the loss of the butadiene band (known to favour crosslinking) and increase in Youngs modulus. However, at high exposure levels, the reduction in UTS has been attributed to chain scission.

Previously published work agrees with the expected response of polymers to radiation. Both PLA and ABS demonstrated signs of cross-linking and chain scission. This is apparent from mechanical and chemical inspection of the materials after radiation. Substantially more degradation is observed in PLA when compared to ABS. Literature has indicated that the aromatic ring present in ABS increases the resistance to radiation-chemical-induced changes [83].

2.5.5 Polymetric AM Parts Response To Gamma Radiation Summary

The flexible and complex fabrication abilities of AM parts make them well-suited for numerous applications in radioactive environments. For successful deployment, robust materials must be identified for operating in such environments. Findings from work will validate if 3D printed materials are suitable for the manufacture of Lynkeos' muon imaging system, where a year of operations radiation exposure could reach 2MGy.

Chapter 3: Design Process For Muon Detector Structure

3.1 Introduction

This chapter focuses on improving the 3D printed components required to house the electronics for a muon imaging system. Preliminary design solutions by 3DScint have been investigated to identify limitations hampering adoption into the industry, and possible solutions have been presented. The deliverables, limitations and solutions have been laid out in a product design specification (PDS) in Table 3.1. The design specification has been used as a reference to track improvements throughout the design process.

A novel design solution was proposed to target limitations in the design specification. Initially, two improvements were proposed for the novel design, integrated electronics and modular detection area components. Following the fabrication of the novel design solution, two testing procedures were carried out at The University of Glasgow. The test consisted of recording cosmic ray interactions within the scintillating fibres and reconstructing singles to produce spatial plots of the cosmic ray distribution.

The novel design solution was then compared against the design specification and further improvements were identified. These improvements focused on a single component for development, the fibre housing channels. Two aspects of the component have been investigated for improvements, the geometry and the manufacturing process. These improvements were validated through visual inspection of prototypes, and simulated print runs to assess the print time and material usage. Further improvements were again compared to the remaining deliverables set out in the design specification.

Finally, a new design strategy is proposed. The concluding section discusses how the improvements recommended have addressed limitations with the 3DScint prototype and improved the commercial feasibility of 3D printing muon imaging structures.

3.2 Preliminary Work - 3DScint

Preliminary work by Lynkeos and 3DScint printed and validated a small-scale prototype scintillating muon imaging system. Figure 3.1 shows the components and assembly of the prototype. The prototype successfully held the scintillating fibres and produced 2D spatial plots of muon interactions [9]. The design was printed without the use of support structures to mitigate damage to the fibres during installation.

3D Scint used two layers of staggered square channels arranged orthogonally and joined using adhesives (Figure 3.1 - a & c). At the end of the fibre channels, extra fibre optics were used to route the signals to the silicon photomultipliers (SiPM), Figure 3.1 - f). After a muon interaction within the fibre, the SiPMs convert photons produced within the fibre to an electrical signal. The electrical signal is then relayed to a processing unit to calculate the position of the muon (Figure 3.1 - f).

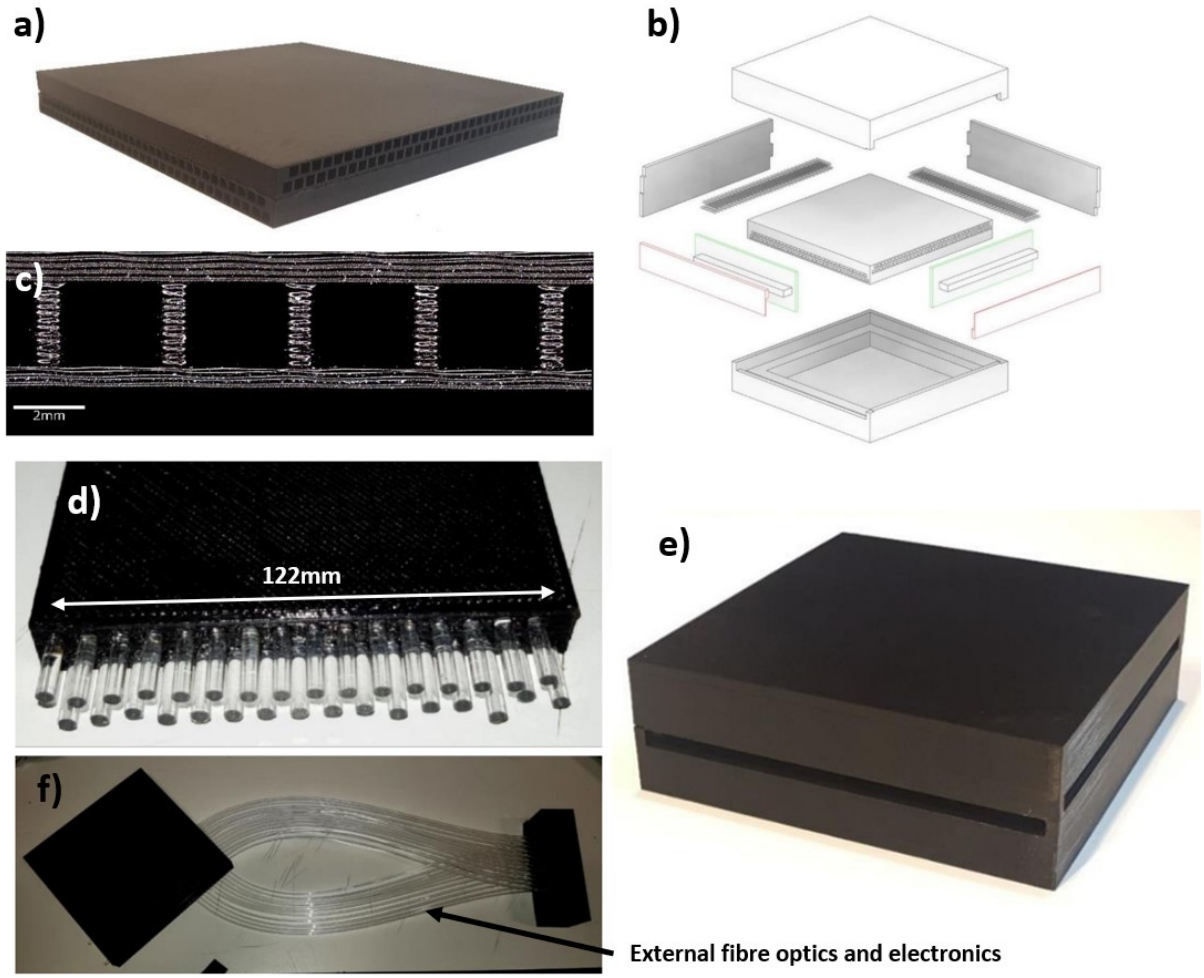

Figure 3.1 – 3DScints prototype design [9] *a) Four layers of 2mm fibre channels, two stacked in x and two stacked in y. b) Exploded assembly of the detector. c) Microscope image of square geometry channels. D) 2mm fibre installed in channels. e) Full assembly of the detector. f) Full assembly connected with scintillating fibre to external SiPMs and FERs.*

3.2.1 Limitations with 3DScints Prototype

The proposed design by 3DScint successfully demonstrated the feasibility of fabricating structural components required for a muon imaging system. However, there exist limitations with the design that hamper the commercialisation of the system.

1) Scalability

For commercial applications, Lynkeos require adaptable scaling of the system to meet customer needs. This is key to making the system attractive to a range of industrial applications. The design proposed by 3DScint has a fixed detection area. Efforts to scale this design would lead to long print times, a part too large to fit within the build volume and require excessive material and adhesives

To improve the scalability of the system, modularity can be incorporated. This provides a standardised approach to increasing the detection area of the system. Furthermore, modularity would break parts into printable sections and remove the need for adhesives between layers.

2) Electronics

A significant limitation of the design proposed by 3DScint is the external electronics required to house the SiPMs (Figure 3.1 – f). Similarly to Lynkeos' current design approach, the design proposed by 3DScint requires external components to route signals to SiPM positioned outside of the system. This reduces the system's efficiency as the signal strength weakens proportionally to the length of fibre traversed.

To improve electronics integration, Lynkeos has acquired new SiPMs that interface directly with the scintillating fibres. The new SiPMs (Figure 3.3) have a linear spacing of 3.5mm. This allows for direct interfacing with the scintillating fibres and a fully integrated system drastically improves the compactness and mobility of the system.

3) Fibre access and positioning

A high cost associated with muon imaging systems is the scintillating fibres. Lynkeos currently use adhesives to permanently install the fibres onto polystyrene panels. 3Scint has improved upon this by removing the use of adhesives, simply using friction provided by the channels to hold the fibres in position. However, fibres are only able to be removed after a full disassembly of the system, making it labour-intensive to repurpose the fibres. Additionally, to accurately align the fibres with the SiPMs, the friction must be high enough to prevent slippage during operation but low enough to allow realignment for good interfacing. With the square channel geometry chosen by 3DScint fine-tuning the frictional resistance is difficult.

Leveraging the advantages of 3D printing allows complex geometries to be fabricated. Changing the square geometry to a more complex shape could provide advantages to the accessibility and positioning of the fibres.

4) Fibre selection

Maximising the detection probability of muons traversing the detection area improves the imaging time frame; the more muons detected, the more data collected for reconstruction. The design proposed by 3DScint limits the diameter of fibres to 2mm. Thin fibres create angular dark regions in which muons passing through the detection plane can be missed.

To increase the diameter of fibre which can be installed channels must be made larger. The manufacturing technique used by 3DScint is limited to a maximum fibre diameter of 2.5mm, at which point the walls between fibres become too thin to fabricate. Thus, a higher resolution technique is required.

5) Material robustness

Lynkeos' current operating environment exposure the system to ionising radiation, which is known to degrade polymeric material. No attempts were made to investigate if the material used, PLA, maintained mechanical integrity in the required environment. An investigation into 3D printed material robustness to gamma radiation is provided in Chapter 4.

The work presented in this chapter has considered the limitation of 3DScints design, applying the knowledge gained from their prototype to influence design decisions for an updated novel design solution.

3.3 Design Specification: Deliverables, Limitations, and Solutions

The work presented in this thesis has produced a novel design to address the limitations of 3DScints prototype. To target the limitations a design specification has been produced, Table 3.1. The specification has defined design deliverables within five categories. Factors limiting the deliverable have been identified and possible solutions have been provided. Deliverables have been assigned as a class denoting whether this is an **existing** deliverable from 3DScints work (**E**) or a **new** deliverable addressed in this research (**N**). The novel design solution presented in this work will consider the **existing** limitation tackled by 3DScint and incorporate **new** solutions to enhance the commercialisation of the system.

Table 3.1 Design Specification - Identified from 3DScints prototype

ID	Deliverable	Limitation	Solutions	Class
Performance				
1.1	Photon detection efficiency *	Minimise dark zones between fibres	Staggered layers of fibres	**E**
1.2	Angular resolution **	The structural integrity of walls between fibres	Higher resolution printing	**N**

1.3	Spatial resolution	Predetermined by electronics. SiPM spacing 3.5mm	Constrained	**N**
1.4	Light proofing	External light sources will not excite fibres	External shell material	**E**
1.5	Good interfacing between fibres and SiPMs	Difficult to position fibres after installation	Fibre position adjustable after assembly	**N**
1.6	Cross talking	Minimise cross-talking between scintillating fibres	Ends of fibres should not have a line of sight to other fibres	**E**
Geometry				
2.1	Scaling detection area	Limited print volume size: 250x250x300mm	Modular detection area components	**N**
2.3	Integrated electronics	Signals routed outside of the system for processing	SiPMs provided by Lynkeos can be integrated into the system	**N**
Materials				
3.1	Radiation robustness ***	Should maintain mechanical properties at operating radiation levels	See Chapter 4	**N**
Additive manufacturing				
4.1	Fast fabrication	3D printing is a batch process, multiple print runs are required for full fabrication	Optimising print parameters and orientation	**N**
4.2	Low cost		Material choice and manufacturing method	**N**
Assembly				
5.1	Assembly time and manual labour	Individual components must be assembled following fabrication	Minimise the number of parts and steps	**E**
5.2	Maintenance	No access to components once installed	Fibres should be assessable without total disassembly	**N**
5.3	Mobility / Transport	Non-integrated electronics make transporting the system difficult	Improved compactness of the system to increase the mobility	**N**
5.4	Disassembly	Adhesives prevent disassembly	Remove the use of adhesives	**N**

Each deliverable has been assigned a class to denote whether the deliverable has been met in previous design proposals. Existing deliverables (**E**) have been incorporated into the design proposed by 3D Scint. New deliverables (**N**) have been identified from limitations with 3Dcints design and focus more

on commercial prospects of the design. Both classes of deliverables will be incorporated into the new design proposed in this work.

* Photon detection efficiency

The system's performance will depend on the efficiency of muon detection. Photon detection efficiency (PDE) can be defined as the probability that a muon traversing the detection area is recorded by the system. Increasing the PDE reduces the timeframe for image reconstruction as more events are recorded proving more data per unit of time.

** Angular resolution

The diameter of the fibre determines the angular resolution, as shown in Figure 3.2. The majority of muons reaching the surface of the earth have an angular deflection from horizontal of ±30° from horizontal [2]. Increasing the diameter of the fibre reduces the *angular dark region*, increasing the probability and efficiency of detecting muons. Previously, 3DScint used 2mm fibres; Lynkeos are hoping to increase the diameter to 3mm. Geometry has been used to calculate the *angular dark region* using the known spatial resolution from the SiPM, fibre diameter, and tangent lines between adjacent fibres. Figure 3.2 shows the *angular dark region* for different diameters of fibres. For 2mm, the dark region is 33.5°, between 4.5°and 38°. Increasing the diameter to 3mm reduces the dark zone to 4.24°, between 23.89° and 28.13°.

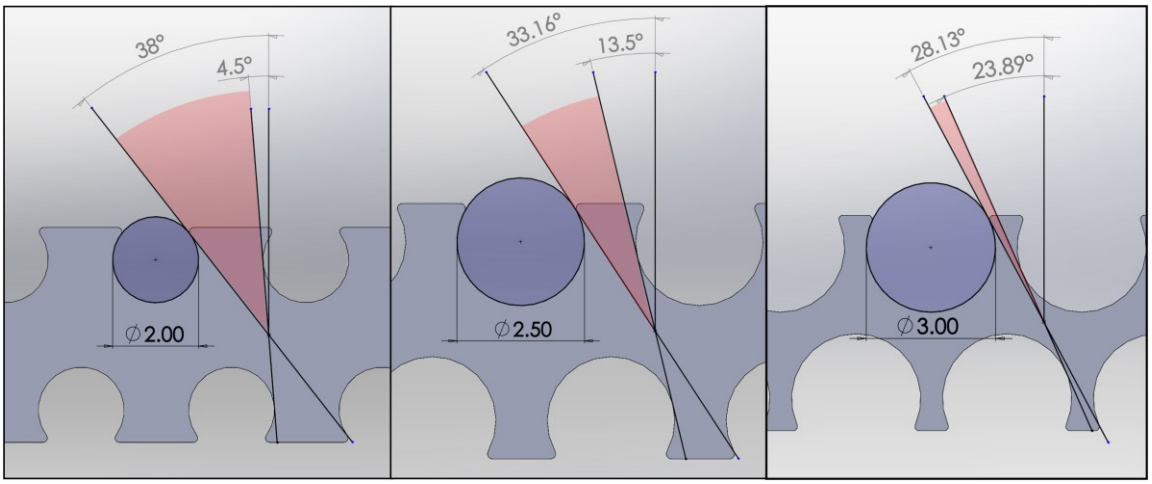

Figure 3.2 *– Angular dark region calculated for various fibre diameters*

The issue with increasing fibre diameter is reducing the thickness of walls between fibres. Thinner walls are harder to print accurately and are more susceptible to failure.

*** Radiation robustness

Lynkeos deploy their MIS in close proximity to nuclear waste. Nuclear waste will emit ionising radiation, which is known to degrade the mechanical properties of polymeric materials. Thus there are concerns about the mechanical integrity of 3D printed parts when operating for extended periods near radiation. Chapter 4 investigates if the robustness of 3D printed materials is suitable for deployment in radioactive zones.

3.4 A Novel Design: Modular and Integrated

Following the identification of limitations and possible solutions, a novel design has been proposed. This design has taken inspiration from the solutions identified in the design specification.

Note, these solutions have not addressed all the deliverables set out in the design specification but have been used as a starting point to improve the most pressing limitations identified with the system.

Two key changes have been made to improve upon 3DScints design:

6) Integrated electronics

New SiPMs provided by Lynkeos, Figure 3.3, have improved the integration of the electronics within the system. The new SiPMs constrain the spacing of fibres to 3.5mm, ID 1.3. Additionally, the new SiPMs can directly interface with fibres removing the need for extra fibre optics routing the signals to processing units, ID 2.3. The new electronics also improve the compactness of the system, ID 5.3, as the SiPMs are directly connected to the imaging structure.

7) Modular channels

The channels used to house the fibres in the detection area have been divided into quadrants. This has been done to allow channels to fit within the build volume, ID 2.2, and provide a method to adaptively scale the detection area to meet the customer's needs, ID 2.1. By integrating modularity into the design the detection area can be increased to meet specific customer needs. The modular channel has been incorporated with the use of adhesive, ID 5.4, opting to use structural support to position the channel instead.

It is hoped that incorporating these solutions into the design will improve the commercialisation of the system. To assess the effectiveness of the solutions a full prototype has been manufactured, assembled, and tested. The following sections discuss existing constraints, manufacturing of 3D printed components, and testing of the prototype.

3.4.1 Constraints: Electronics and Fibres

The electronics provided by Lynkeos placed initial dimensional constraints on the design. There are three components provided by Lynkeos listed below:

(I) Silicon Photo-Multiplier (SiPM)

Hamamatsu Photonics, Japan, produced the SiPM PCBs. PCBs have 64 cells arranged in a single line. There are four screw holes in the corners and an electronic coupling (Samtec HSEC8 170-02-S-DV) on the backside. SiPMs are responsible for transferring optical signals from the excitation within the fibres to electrical signals for data processing.

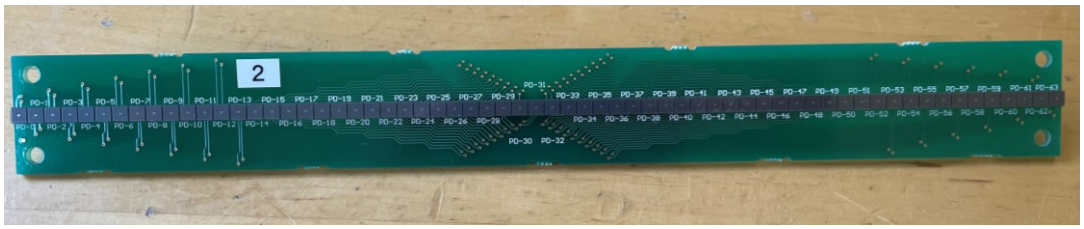

Figure 3.3 *– Silicon Photo Multiplier (SiPM) PCBs. 64 photo-sensitive cells per card*

(II) Front End Readout System (FERS)

CAEN, Italy, produced the FER PCBs. The FERs are responsible for collecting the digital readout from the SiPMs and relaying the signals back to the processing units.

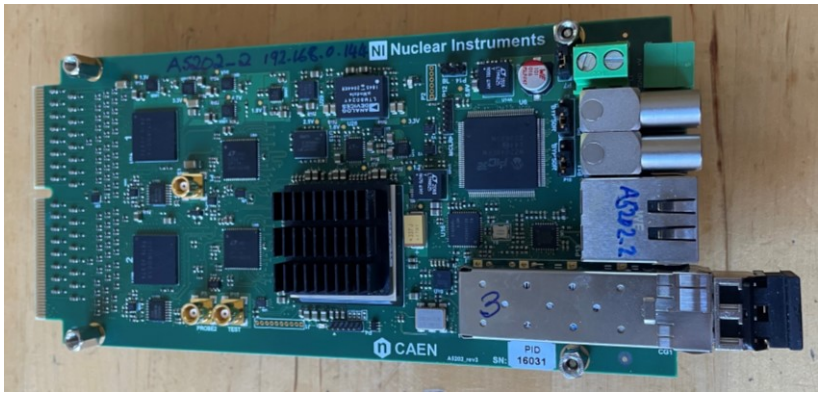

Figure 3.4 *– Front End Readout (FERs) cards*

(III) Scintillating fibres

Bicron, USA, manufacture the scintillating fibres. The fibres have a polystyrene-based core and PMMA cladding. They are responsible for the detection of muons. When charged particles interact with the fibre, photons are emitted using total internal reflection; signals are relayed to photosensitive cells at the end of the fibres.

3.4.2 Manufacturing: 3D Printed Components

The manufacturing was equivalent to 3DScint, all components were manufactured on a Sidewinder X1 FDM printer using a 0.4mm nozzle. The material used for fabrication was PLA. Printing parameters are provided in Table 3.2.

Table 3.2 Novel design printing parameters

Printing parameter	PLA
Infill (%)	100
Nozzle Temp (°C)	210
Bed Temp (°C)	65
Layer Height (mm)	0.2
Raster orientation (°)	± 45
Speed (mm/s)	60

The 3D printed components have been designed to accommodate the constraints mentioned above whilst also providing structural rigidity and shielding from external light sources. Four 3D printed components have been listed below:

(I) Fibre channels

The channels used the same geometry as 3DScint's design. Square channels are arranged in a double staggered layer, reducing dark zones and improving angular resolution. This prototype used two layers of four fibre channel components, providing insight into the feasibility of modular scaling.

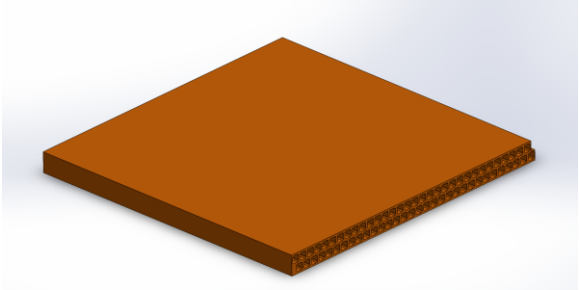

Figure 3.5 *– Initial prototype channel geometry. The figure shows 1 out of 8 channels required for complete assembly*

(II) Interface

The interface components are connected to the SIPM using threaded inserts. The SiPM could then be assembled with the rest of the structure. Cut-outs in the interface aligned with SiPM cells to allow contact between cells and fibres.

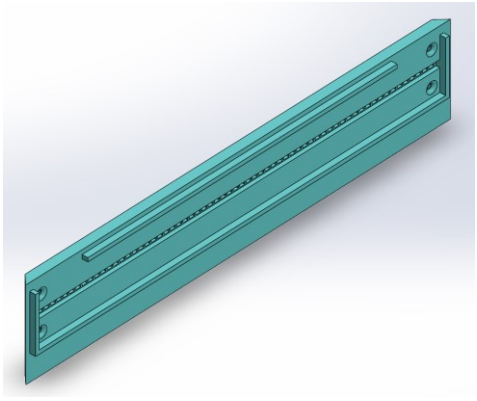

Figure 3.6 *-SiPM interfacing component. Four are required for complete assembly*

(III) Crossbeam and Corner Joints

The beam runs along the intersection between channels, providing vertical support. Cut-outs in the interface components support the beam.

The corner joints use friction to join the four interfacing components together. Two joints are placed where interfacing components meet. The corner joints also vertically support the channels in the corners.

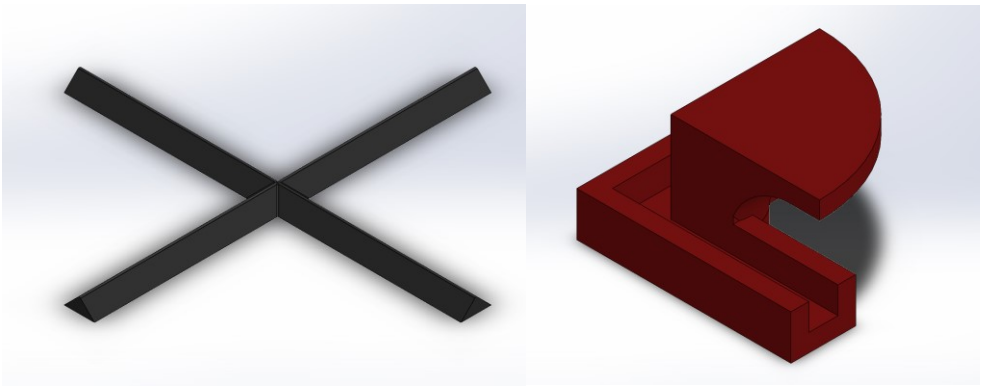

Figure 3.7 *– Crossbeams (Left) Two are required for complete assembly. Corner joints (Right) eight are required for complete assembly*

3.4.3 Novel Design Assembly

A diagram of the fully assembled novel design is provided in Figure 3.8. A diagram of the cross-section is provided in Figure 3.9 to visualise the two perpendicular directions of channels. The detection area of the novel design proposal is 0.05$m^{2,}$, which is a 335% increase compared to 3DScints prototype (0.015m^2).

Figure 3.10 shows the fully assembled initial prototype. The assembly process was completed by hand and took around 3 hours, with most of the time spent cutting and installing 2mm fibres. It is noted that not all channels were able to house fibres due to blockages in the channels. This occurred either on the first layers or the first bridging layers where small defects during material deposition were significant enough to affect the tight tolerances required for fibre positioning. The width of the channels was 2.8mm providing 0.8mm tolerance when installing the 2mm fibres. These blockages were difficult to remove due to the thin walls and long channels. Some fibres were cut by hand, reducing photon transmissivity to the SiPMs.

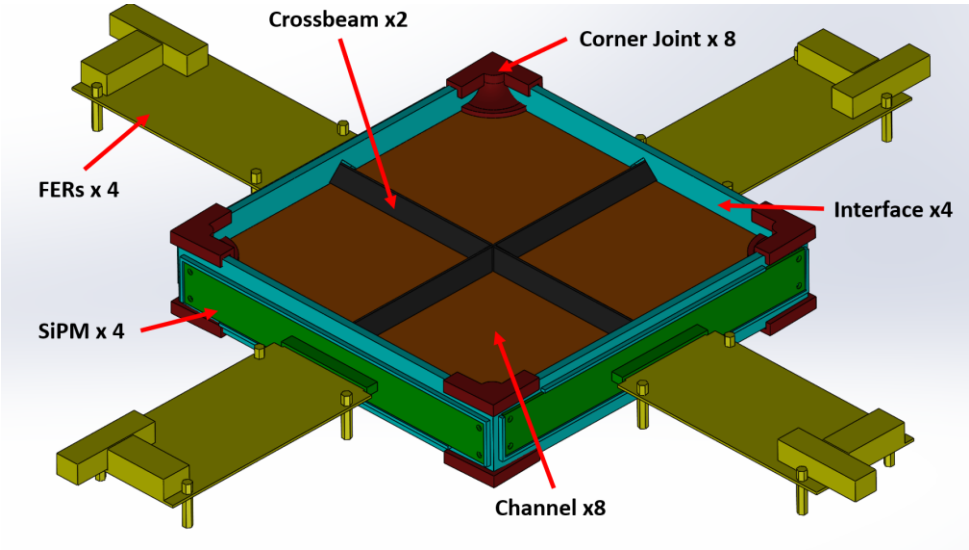

Figure 3.8 *– Diagram of novel design assembly. Components quantities have been labelled.*

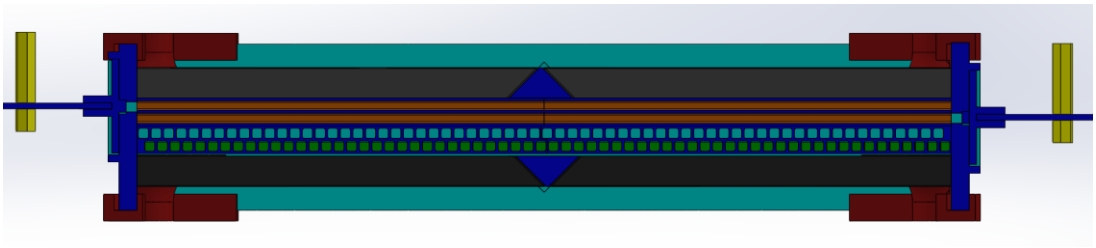

Figure 3.9 *– Cross section of the novel design proposal*

Figure 3.10 *– Complete assembly of the novel design proposal. Inc. 3D printed components, Fibres, and SiPMs*

3.4.4 Novel Design Testing

3.4.4.1 Testing Set up

Once all components were assembled, the FERs cards were linked together and connected through Ethernet to an external clock. The use of an opaque cloth was required to prevent external light from interfering with the measurements, Figure 3.11. Photons interacting with the scintillating fibres lead to a current produced by the SiPMs. Good external light proofing was confirmed by measuring a standby current from the FERs of less than 0.1 Amp.

During testing, the frequency of events was recorded for each channel number. An event is identified as a signal above the 0.1 Amp threshold. It is important to note that not all events indicate a muon interaction. Threshold optimisation would be required to filter background noise to only record muons. Other radiation sources, such as alpha and beta, could lead to recorded events.

Detectors have been labelled in Figure 3.11. Comparing different axis detectors, i.e. D1&D2 or D3&D4, provides insight into the spatial distribution of the events, which be calculated if the channel spacing is known. Visualisation of event location was produced using the Root Software, Cern. As each SiPM had 64 channels, the images produced have a resolution of 64x64 pixels per image. Figures 3.12 and 3.13 have been produced by comparing the time stamp of events between detectors.

Two experiments were run. First, a passive background test with no external source was run for approximately three hours, Figure 3.12. This test recorded naturally occurring charged particles which

induced a current above 0.1 Amp in the SiPM PCBs. The second test introduced a beta source, Strontium 90, into the environment, Figure 3.13. The beta source was placed in a known location, Figure 3.11, and data was collected for 10 minutes.

To visualise the data, event records from separate detectors can be compared. Figures 3.12 and 3.13 compare perpendicular axis channels to produce spatial X-Y plots indicating the position of events within the detection area.

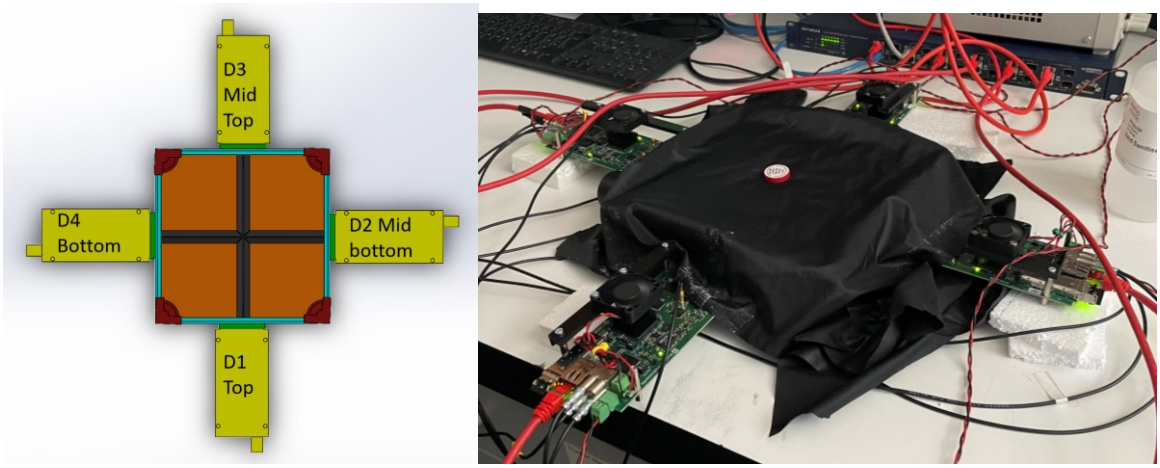

Figure 3.11 *– Testing set up for initial prototype validation. Detector labels (Left). Light proofing fabric and strontium beta radiation source (Right)*

3.4.4.2 Results from Testing

Passive Background testing

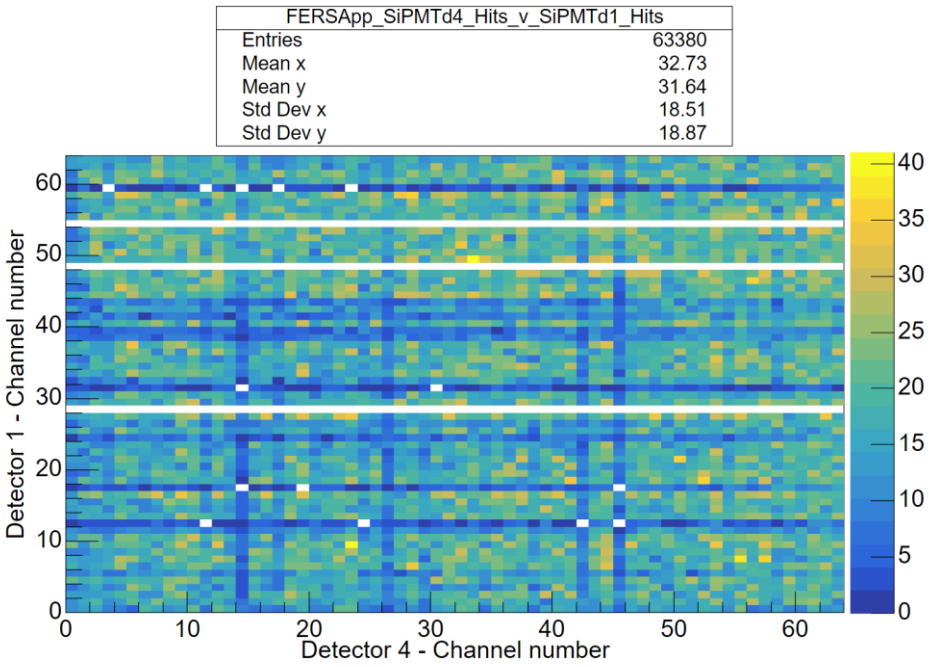

Figure 3.12 *– Results from passive background testing, D1 vs D4*

From the background study, the system successfully detected events. It is also clear which channels were missing fibres due to blockages and which channels have reduced events due to poor meshing with the SiPM. Over the 3 hours of background testing, 62280 events were recorded which is equivalent to a flux of 114 Hz/m^2.

Active beta source, Strontium 90 testing

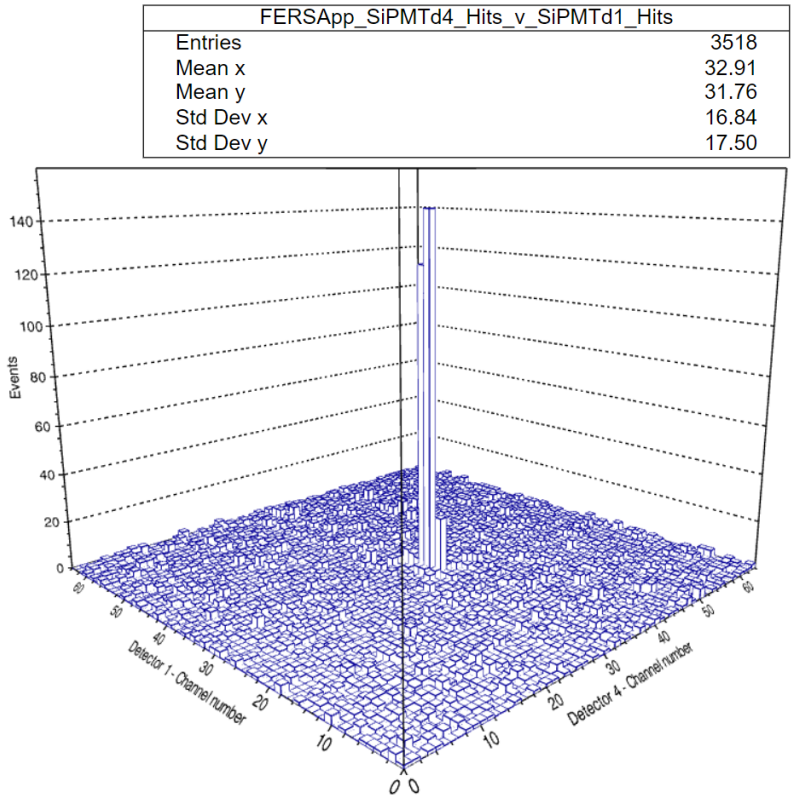

Figure 3.13 *– Result from Strontium 90 beta source testing. D4 vs D1*

From the strontium testing, the prototype successfully locates the beta source's position, indicated by the numerous events recorded in the centre of the detector. Only the expected channels measured a high number of events indicating cross-talking was not occurring.

3.4.5 Discussion Of Results From Testing

The initial prototype validated 3DScints work, demonstrating 3D printing is a feasible solution to manufacturing cosmic-ray imaging enclosures. The structure provided enough rigidity to hold the fibres in position. The resolution of the 2mm fibres was suitable to indicate the location of the beta source within 10 minutes.

Background testing measured flux of 114 Hz/m^2 events. It is difficult to draw definitive conclusions on the efficiency of the system from this result. There are many factors that affect the detection rate of the system, i.e. the environment (height above sea level, shielding of buildings, radiation sources present in the room), the system (efficiency of scintillator, photo transmissivity, the current threshold for an event, missing fibres, angular resolution). That being said, research conducted into five different Latin American giant observatories (LAGOs) in the southern hemisphere, recorded a flux of secondary particle radiation in the order of magnitude of 10^2 Hz/m [84], a similar result to that presented in this thesis.

The prototype further demonstrated that modular channel parts were a viable solution for scalability, with no significant decrease in performance with the increased detection area and no evidence of cross-talking from the strontium testing.

Below is a comparison of the novel design solution to the original design, specification is provided. Deliverables filled in green have been met. Deliverables filled in yellow were partially met. Deliverables in orange were not considered or improved upon.

Table 3.3 – Comparison of novel design solution to design specification

Deliverable met		Deliverable partially met	Deliverable not met
ID	Deliverable	Discussion	Further solutions
1.1	Photon detection efficiency	High frequency of events was recorded. A beta radiation source was able to be located within the specified timeframe	
1.2	Angular resolution	Fibre diameter remained at 2mm	Higher resolution fabrication methods will allow thinner features to be fabricated
1.3	Spatial resolution	2mm fibres we able to be space to the required 3.5mm	
1.4	Light proofing	Light proofing was achievable with opaque material	Integrate shell structure to block external light sources
1.5	Fibres interfacing with SIPM	Events recorded from charged particles interacting with SiPMs	
1.6	Cross talking	No evidence of cross talking: During strontium testing events were constrained to source location	
2.1	Scaling detection area	Detection area increased by 335% compared to 3DScints prototype	
2.2	Parts limited to build volume	All 3D printed components fit within build volume	

2.3	Integrated electronics	SiPM successfully integrated into the structure	
3.1	Radiation robustness	No testing was carried out	Chapter 4
4.1	Fabrication time	No improvements made	Investigated in Section x
4.2	Reduce cost	No improvements made	Investigated in Section x
5.1	Assembly time and manual labour	Considering added detection area, several parts are similar to 3DScint. Assembly took around 3 hours	Combine the functionality of parts to reduce total components
5.2	Maintenance	No adhesives used allow for full disassembly. Fibres not accessible without disassembly	Investigate channel geometry for better fibre accessibility
5.3	Mobility / Transport	Integrated electronics remove the external fibres for routing signals	
5.4	Disassembly	No adhesives used, full disassembly possible	

3.4.6 Novel Design Summary

From the design specification comparison, Table 3.3, many of the new deliverables defined in this project have been achieved. Importantly, the two solutions applied to the novel design have proved successful in meeting the criteria.

1) Integrating the SiPMs has compacted the design, improving the mobility of the system. The fibres, which were spatially constrained by the SiPM, had good interfacing with the photosensitive cells. No cross-talking was detected indicating there is no line of sight between fibres at the interface between fibres and cells/
2) The modular channel structures, which were constrained by the print volume, significantly increased the detector area by 335% compared to 3DScints prototype. No noticeable drop in efficiency was detected. No cross talking was detected, indicating the modular design did not increase the noise-to-signal ratio.

However, some deliverables have not been met, leading to further limitations:

1. Angular resolution has not improved upon 3DScints design as the fibre diameter was 2mm.
2. Material radiation robustness is investigated in Chapter 4.
3. Fabrication time and cost of materials was not assessed.
4. The maintenance, which is determined by the accessibility to fibres without disassembly, was not improved upon. The square channel geometry prevents access to fibres during operation and makes fibre positioning difficult.

From the review of the new limitations identified, it has been proposed that improvements to the channel component will enable solutions mitigate limitations. The following section discusses opportunities to improve channel geometry components.

3.5 Further Improvements

The main component identified for further improvement is the fibre channel. It is hypothesised that leveraging AM advantages will enhance the design of the channel components, ultimately addressing the remaining deliverables not met in the design specification.

The deliverables that will be targeted in this section are angular resolution, fabrication time, material and process costs, and maintenance (accessibility to fibres). To address the deliverables both the channel geometry and manufacturing process have been investigated. Tests have been carried out for two diameters of fibres (2.5mm and 3mm), three new channel geometries (**Vertical Press-fit**, **Single layer press-fit**, and **Square**), and three fabrication AM processes (**FDM 0.4mm nozzle**, **FDM 0.2mm nozzle**, and **SLA**). Combinations of fibres, geometries, and processes have been fabricated to give insight into the most suitable approach to meet the deliverables et out in the design specification.

3.5.1 Channel Geometry

There are two geometries compared in this section the **square geometry**, used by 3DScint, and the **press-fit geometry**.

The new press-fit design proposed provides advantages over the square geometry. Firstly, the open channel design allows fibres to be installed later in the assembly process and be accessed and removed without full disassembly, ID 5.2. The press-fit design also opens the possibility for thicker fibres to be installed, ID 1.2. Finally, the press-fit design uses less material per unit area of the channel, ID 4.1, 4.2. However, there are potential issues with the design which include the rigidity of the component, the strength of the walls, and possible cross talking from exposed fibres.

Two FDM orientations of the press-fit are proposed, vertical and single layer, to investigate if changing the orientation will affect the strength, alignment, and friction of the components. The orientation also affects the printing success of the part as high vertical to horizontal ratios are more likely to fail and take longer to print. However, printing in a vertical orientation allows more components to be printed in a single run.

Below a list of the geometries are presented:

1) **Square**

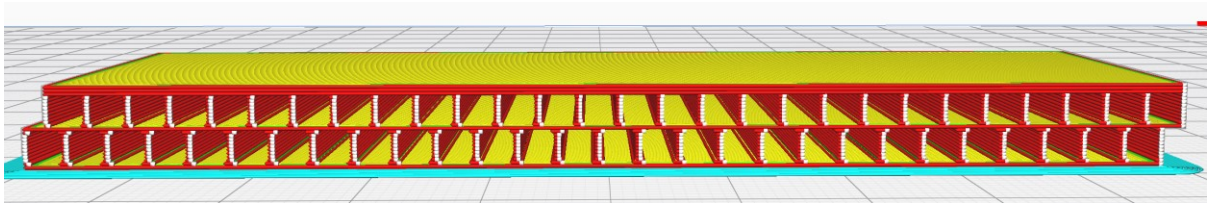

Figure 3.14 - FDM slicing profile of square geometry

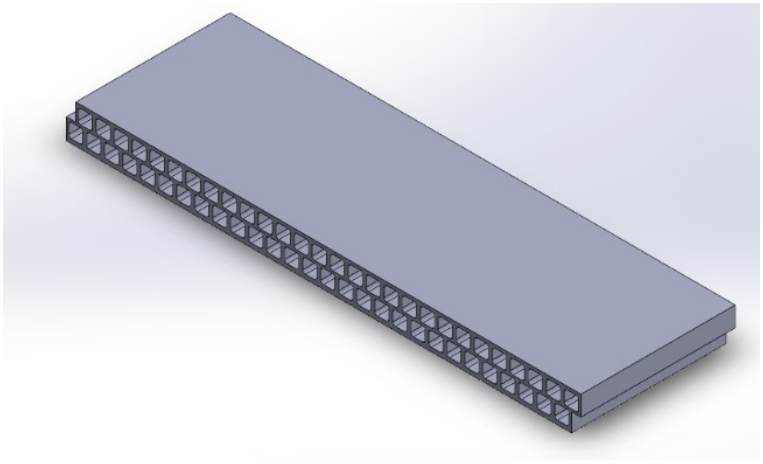

Figure 3.15 – CAD model isometric view of square geometry

2) Vertical press-fit

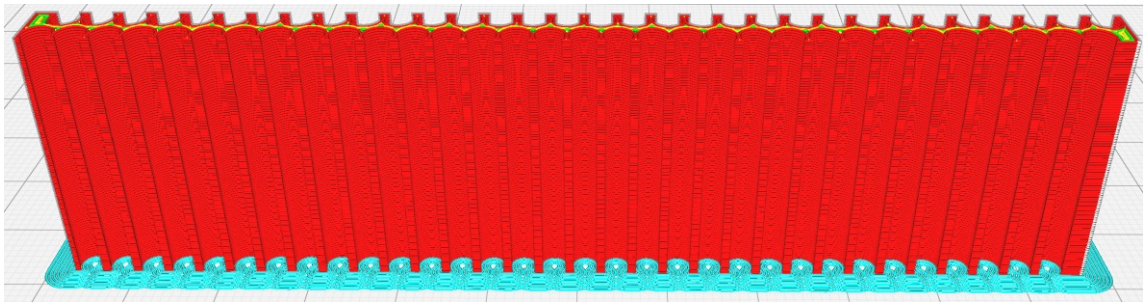

***Figure 3.16** - FDM slicing profile of vertical press-fit*

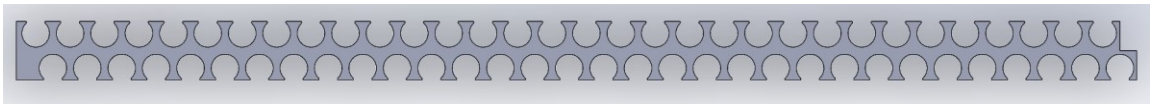

***Figure 3.17** - CAD model vertical press-fit view parallel to fibres*

3) Single-layer press fit

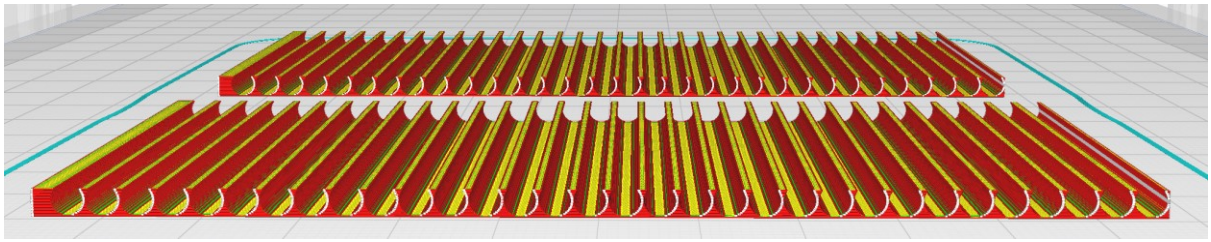

***Figure 3.18** - FDM slicing profile of single-layer press-fit*

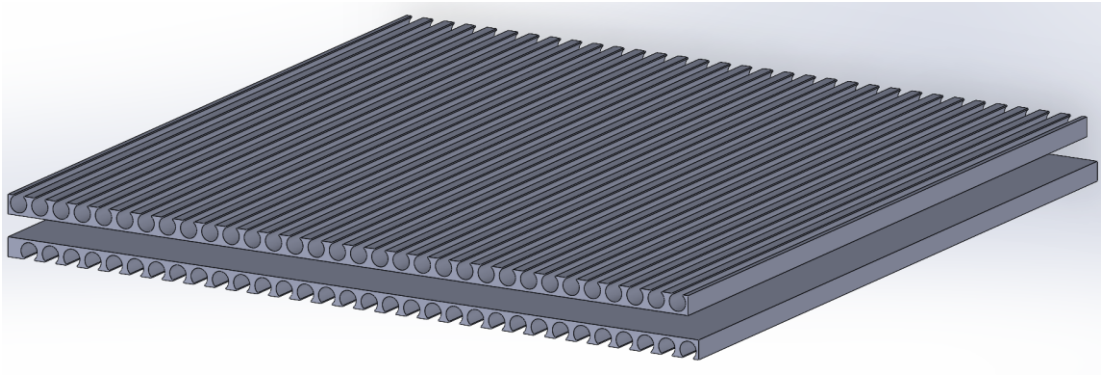

Figure 3.19 *- CAD model isometric view of single layer press-fit. Adhesives are used to join single layers together.*

3.5.2 Manufacturing Process

Reviewing the manufacturing process will give insight into the required resolution for thicker 3mm fibre to be installed, ID 1.2. The manufacturing process will also affect the print time and the material costs, ID 4.1, 4.2. The two types of AM processes investigated are **FDM** and **SLA**.

The **FDM** solutions have used two diameters of nozzles, a standard **0.4mm nozzle** and a smaller **0.2mm nozzle**, to improve the resolution. FDM 0.4mm is unable to print the required features to house the 3mm fibres as the walls between fibres are too thin as shown in Figure 3.20.

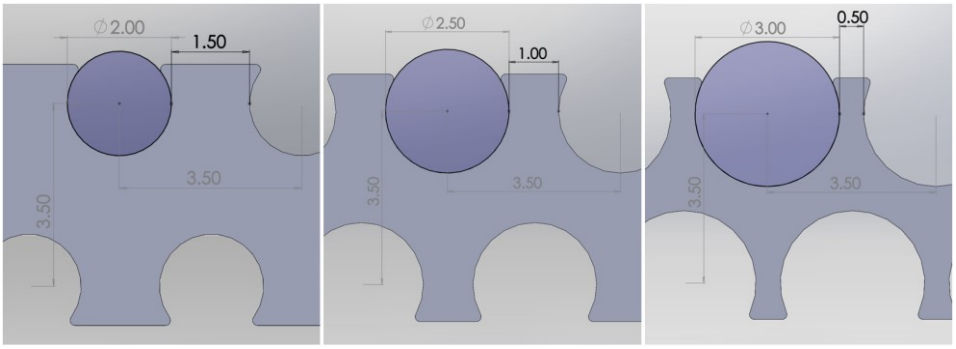

Figure 3.20 *– Effect on wall minimum wall thickness with increased fibre diameter. Fibre diameter increasing from 2mm to 3.5mm*

Both SLA and FDM 0.2mm is capable of printing the required wall thickness. SLA can achieve significantly higher resolutions than FDM 0.2mm. However, the required post-processing steps and the equipment and material costs are higher.

The orientation of SLA parts is less of a concern when fabricating so the single-layer press-fit has not been considered for this manufacturing solution

3.5.3 Physical Testing Of Geometry And Manufacturing Solutions

Small-scale parts were fabricated, varying the fibre diameter, geometry and manufacturing process. FDM parts were fabricated using PETG. Recommended temperatures from the material supplier were used. SLA parts were fabricated using 'ABS-like' material from Phrozen. Recommended exposure times and layer heights from the supplier were used. Corresponding fibre diameters were manually installed in channels, and visual inspection identified strengths and weaknesses.

FDM 0.4mm nozzle

For FDM with a 0.4mm nozzle, the square geometry performed poorly due to high friction preventing alignment with the end of the channel. Blockages and sagging within the channels prevented the installation of some fibre leading to dark zones.

The single layer press-fit channel is deflected with fibres installed. Using adhesives will reduce this; however, internal strains will occur in the fibre reducing the longevity of life.

The vertical press-fit performed well with low friction and no blockages. The alignment of the fibres at the end of the channel was good

As previously mentioned fibre diameter directly affects the angular resolution of the detector. However, thicker fibres require thinner wall material which is physically impossible to fabricate with a 0.4mm nozzle as the spacing between fibres is less than 0.4mm.

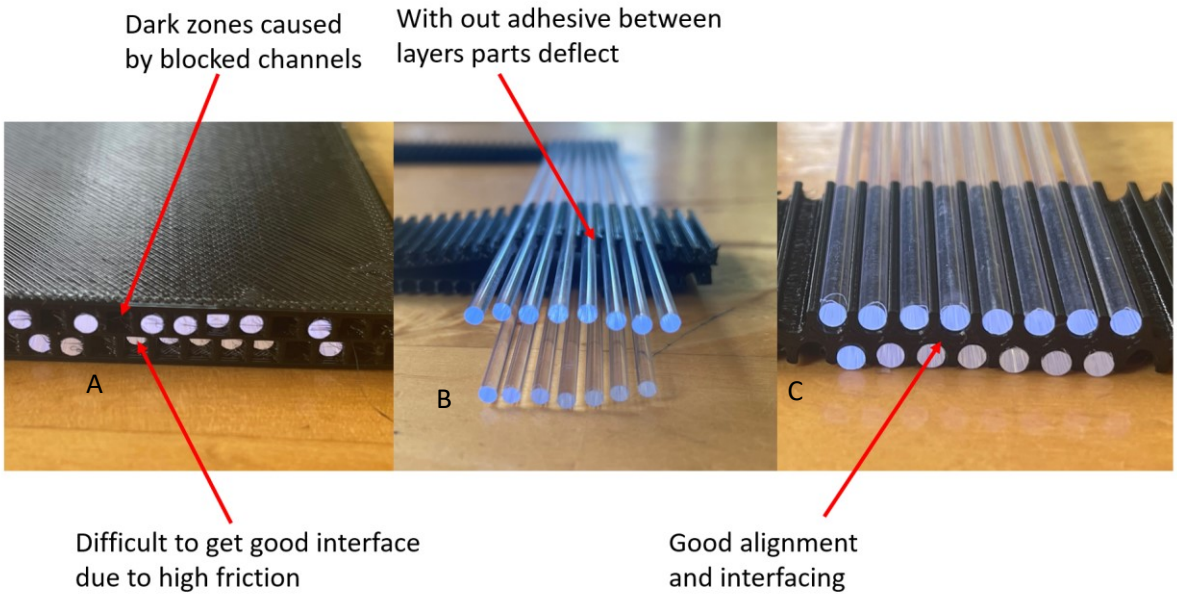

Figure 3.21 *–FDM 0.4mm nozzle channel test prints with 2.5mm fibres installed A) square geometry 2.5mm fibre. B) single layer press fit 2.5mm fibre c) vertical press fit 2.5mm fibre*

FDM 0.2mm nozzle

FDM 0.2mm could not achieve the required tolerance to house 3mm fibres in the square channel. Single layer press-fit was too weak to house the fibres leading to failures during installation. The vertical press-fit performed well, capable of housing 3mm fibres with minimal warping and demonstrated good alignment with the end of the channel.

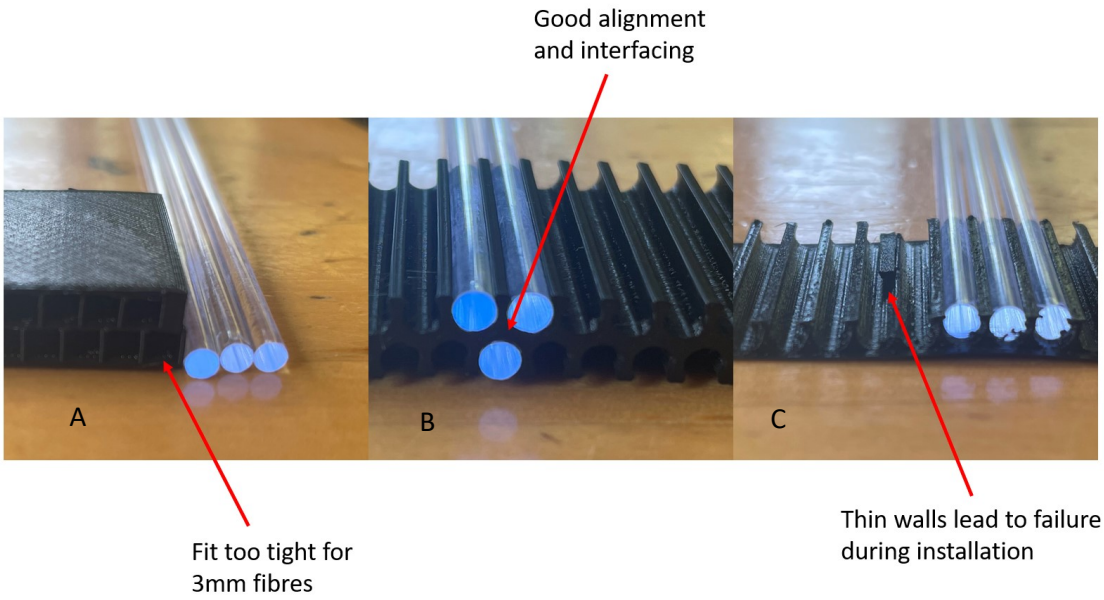

Figure 3.22 *–FDM 0.2mm nozzle channel test prints with 3mm fibres installed. A) square geometry 3mm fibre. B) Vertical press fit 3mm fibre. C) single layer press fit 3mm fibre*

SLA

SLA parts performed the best. The high resolution of SLA printing allows excellent tolerancing of channels and both diameters of fibres to be fabricated. There was minimal friction between channels and fibres, allowing good alignment with the end of the channel for all geometries and fibre diameters.

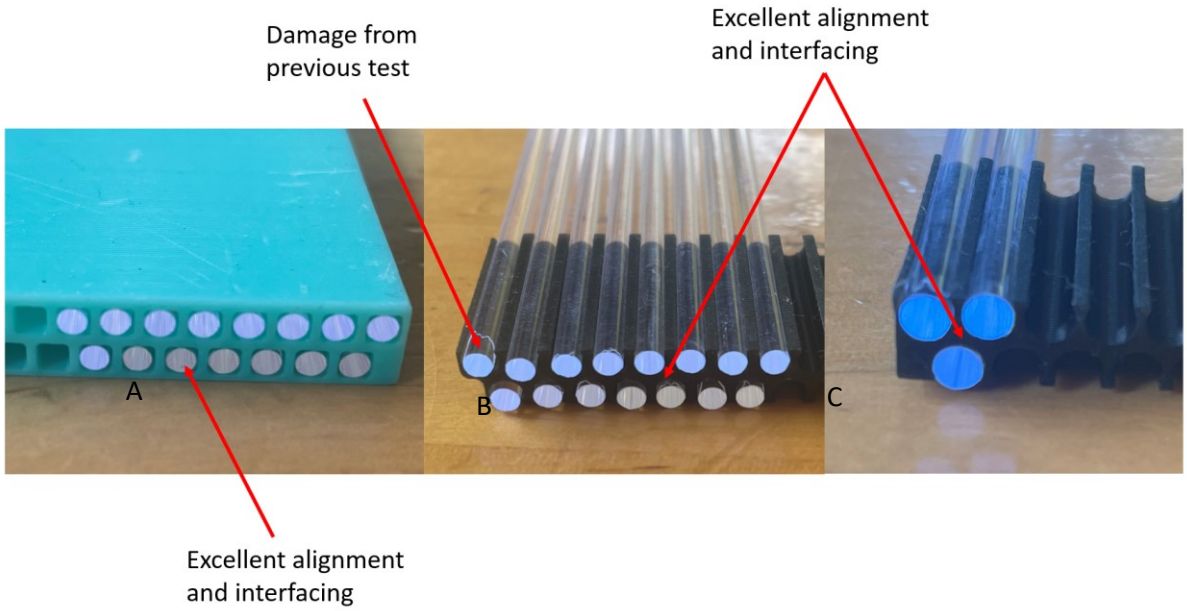

Figure 3.23 *–SLA channel test prints with 3mm fibres installed. A) square geometry 2.5mm fibre. B) vertical press fit 2.5mm fibre. C) vertical press fit 3mm fibre*

From the physical testing, the best performing manufacturing process was SLA. Due to the high resolution of SLA, all geometries tested had good tolerances and alignment and did not fracture upon fibre installation. The best performing geometry was the vertical press-fit which provided the most reliable, strongest and best alignment with the end of the channel for all manufacturing processes tested.

3.5.4 Simulated Printing Tests For Geometry And Manufacturing Solutions

Simulations of print runs were used to quantify the economical investment for combinations of AM process, channel geometry, and fibre diameter. Simulations used equivalent channel areas for comparative analysis, 150mmx150mm. No simulations were run for single-layer press fit for prints as there are no benefits from separating the geometry with SLA. For consistency, the channels' top and bottom layers were simulated for the single-layer press-fit geometry.

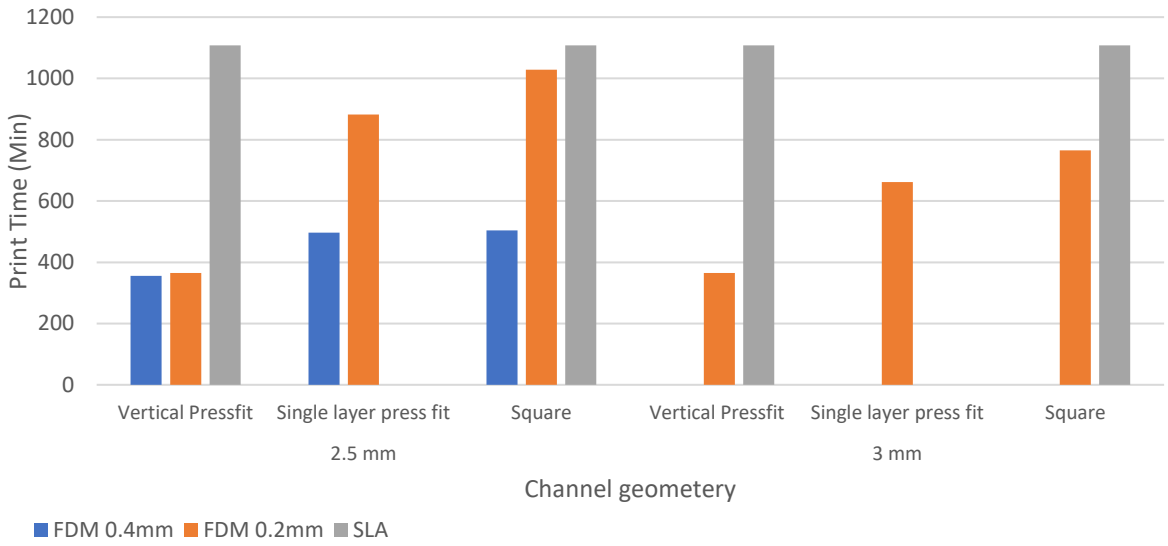

Figure 3.24 *– Simulated print time vs geometry, manufacturing method, and fibre diameter. Simulations were carried out on Cura.*

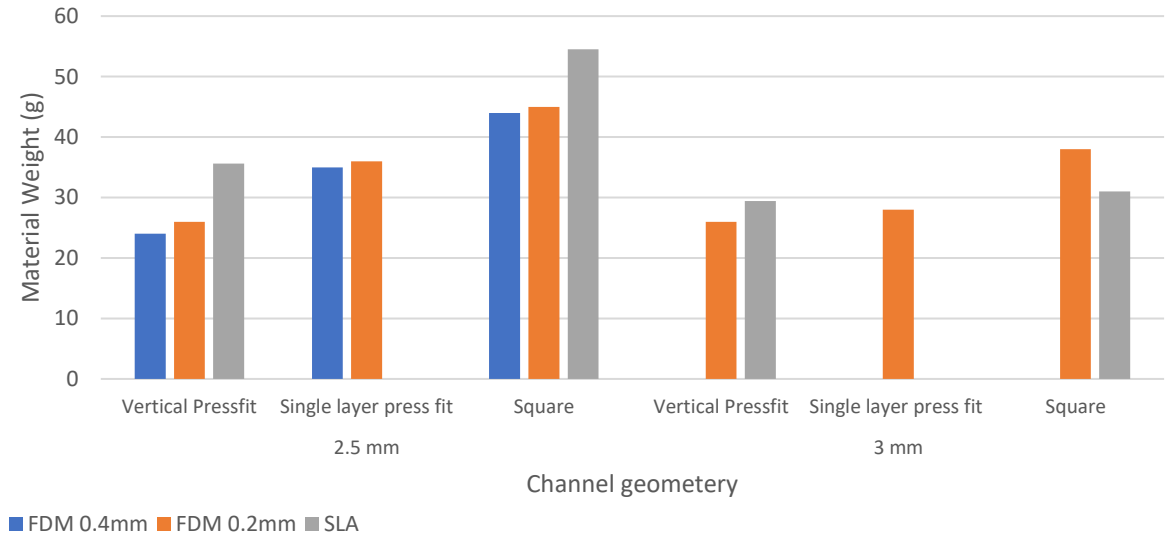

Figure 3.25 *- Simulated material weight vs geometry, manufacturing method, and fibre diameter. Simulations were carried out on Cura.*

From simulations the vertical press-fit geometry is most efficient in terms of print time and material weight, supporting the results from physical testing. In general, square geometries require the most material and time to print.

SLA print times are equivalent for all geometries because the time is determined by the number of layers, which is consistent for the unit area being printed irrespective of the geometry. Material weight is higher for SLA compared to FDM. SLA resin is also more expensive than FDM filament.

FDM 0.4mm is constantly the fastest and uses the least material. However, FDM 0.4mm is unable to print channels for 3mm fibres. Comparing FDM 0.2mm to FDM 0.4mm, material use is higher for single-layer press-fit and similar for a vertical press fit. While it would be expected that decreasing the nozzle diameter would increase the print time, the utilisation of slicing software, removing infill and using vase mode, has made the simulated print times between the two nozzle diameters identical.

The material weight for different nozzle sizes is also similar. The main difference between the nozzle sizes is the ability to print for thicker fibres with a 0.2mm nozzle. For 3mm fibres, FDM 0.2mm performs better than SLA in all data sets except the material used for the square geometry.

3.5.5 Further Improvement Summary

SLA produced the most accurate channels from scaled parts and simulated print runs. However, the significant increase in print time and material use reduces the manufacturability and increases the costs. From the results, the channels are recommended to be printed with a vertical press-fit geometry on an FDM printer with a 0.2mm nozzle. This allows 2.5 mm and 3 mm fibres to be housed in the channels while maintaining minimal print time and material usage.

Table 3.4 compares the solutions presented from further improvements to the design specification.

Table 3.4 – Comparison of further improvement to remaining design specification deliverables

Deliverable met		Deliverable partially met	Deliverable not met
ID	Deliverable	Discussion	Further solutions
1.2	Angular resolution	Increased possible fibre ammeter from 2mm to 3mm	
1.4	Light proofing	No further improvements made	Integrate shell structure to block external light sources
3.1	Radiation robustness	No testing carried out	Chapter 4
4.1	Fabrication time	Fabrication of channels has decreased by	
4.2	Reduce cost	Material wight of channel component has reduced by	
5.1	Assembly time and manual labour	No further improvements made	Combine functionality of parts to reduce total components
5.2	Maintenance	Open press-fit channel geometry allows for installation and maintenance of fibres without out total disassembly	

3.6 Design Process Conclusion

To conclude, this chapter assessed preliminary design approaches to 3D printing muon detection structures by 3DScint. Through investigation of 3DScints design proposal, a design specification was produced to define requirements and compare improvements thought the process.

From the specification, a novel design solution was proposed that integrated electronics and incorporated a modular channel design. This solution was then assembled, and validated at The University of Glasow.

Results from novel design testing demonstrated that 3D printing is a viable option for manufacturing scintillating muon-imagining structures:

- Events were successfully recorded and reconstructed to produce spatial plots of the distribution of events within the detection area
- Beta source emitter was able to be successfully located within the detection area
- No cross-talking was detected, evidenced by the localised distribution of events during beta source testing
- Modular assembly increased the detection area by 335%, compared to 3DScints proposal
- Integrated electronics improved the compactness and mobility of the system
- All structural components were fabricated within the constraints of AM
- No adhesives were required allowing full disassembly and removal of fibres to reuse in other systems

However, the initial design was limited to 2mm fibres, had multiple assembly steps, and channels were prone to blocking – reducing the detection rate. The design process presented then addressed these new limitations. The limitations were targeted by focusing on a single component, the fibre channels. Two areas of the channel fabrication were investigated, geometry and manufacturing process.

The results from further improvements have recommended an improved channel geometry and vertical press-fit. Additionally, the results have recommended an FDM with a 0.2mm nozzle as the preferred manufacturing method. The new geometry has leveraged AM to enhance the performance of the system:

- The smaller nozzle increased the resolution of prints allowing larger fibres to be installed within the channels. Larger fibres increase the angular detection probability and thus reducing the time frame for image reconstruction

- The new geometry requires less material, less print time and more can be printed in a single batch. These factors improve manufacturing and reduce the costs of the system.
- FDM 0.2mm is significantly faster and cheaper than SLA
- The open channel design allows fibres to be installed, repositioned and removed without requiring total disassembly.

The results indicate that commercial benefits are gained from integrating electronics and utilising a modular design. The changes to channel geometry and manufacturing have been provided to Lynkeos for future testing. The recommendation proposed in this chapter will improve the performance, scalability, assembly process, and cost of full-scale systems, ultimately providing Lynkeos with a competitive edge in the market.

Chapter 4: Radiation Material Testing

4.1 Introduction

In this chapter, the response of 3D printed parts to gamma radiation was investigated. Lynkeos currently characterise nuclear waste containers and have shown interest in using AM to fabricate their muon detector structures. Their system will be deployed in close proximity to radioactive material for extended periods. A maximum exposure level when operating near spent nuclear fuel containers within one meter is 5500 Gy/day [59]. Over a year of operations, this equates to 1.65MGy.

As previously discussed in the design section, FDM has been recommended for manufacturing the fibre channels. While advanced high resistance composites such as carbon fibre and ceramics have been shown to be able to be manufactured with FDM, these composites require a polymer-based matrix for fabrication. It has been well documented that polymers will degrade with prolonged exposure to ionising radiation [60]. To ensure the safety and continued performance of the system, it is crucial to assess how the mechanical and chemical properties of FDM parts will respond in this operating environment.

The research presented in this chapter has irradiated three commonly 3D printed materials, Polylactic acid (PLA), Acrylic styrene-acrylonitrile (ASA), and Polyethylene terephthalate glycol (PETG), to increasing levels of gamma radiation to mimic the operating environment. Two print orientations have been investigated to assess the tensile strength and the layer adhesion strength response following radiation exposure. To investigate mechanical changes, tensile and hardness testing was conducted. Fourier transform infrared (FTIR) investigated chemical changes in PETG and ASA. Finally, fracture surfaces were visually inspected to validate the findings from the experiments.

4.2 Methodology

4.2.1 Materials

Two materials selected for investigation in this thesis have previously not been tested for radiation-induced response in literature, PETG and ASA (Table 4.1). The third material, PLA, has previously been tested in literature and was the choice of material for 3DScints 3D printed muon detection system. PETG has gained significant market interest in recent years due to the ease of printing, matching the printability of PLA and surpassing ABS. PETG is also more resistant to high temperatures, UV rays, water, and chemical solvents [85], making it an excellent choice for deployment in harsh environments. Moreover, these properties do not come at a higher cost when compared to PLA, making PETG accessible to a range of consumers and industries. One drawback with PETG is the poor bridging characteristics, leading to surface stringing and making detailed prints more

difficult. However, these can be removed during post-processing and optimising the printing parameters. ASA is well known in the 3D printing community for its excellent weathering resistance, surpassing PLA, ABS and PETG in UV, water, and thermal resistivity [86]. ASA is also easier to print than ABS, with less warping and cracking occurring when printing at larger scales. However, ASA still requires a fume cupboard during printing, as toxic fumes are released due to the presence of the styrene molecule.

It is hypothesised that new materials, PETG and ASA, will demonstrate better resistance to radiation-induced degradation. Polymers containing phenyl groups in the main chain, such as PETG, are known to be more robust to radiation, as the phenyl group absorbs energy, mitigating bond ruptures [62] [83][87]. Similarly, polymers that contain a benzene ring, such as ASA, are more resistant to radiation than polymers that contain saturated bonds [60] [65] [88].

Preliminary 3D printed muon detector structures designed by 3DScint used PLA. Results from PLA testing were used to validate results against previous literature and compare PETG and ASA. Table 4.1 shows the mechanical properties provided by the suppliers for PLA, PETG and ASA. This data will be used as a baseline comparison for the non-irradiated samples.

Table 4.1 Summary of material properties for PLA, PETG and ASA from supplier database

Property	**PLA**(34)		**PETG**(35)		**ASA**(36)	
Supplier	Prusa		Prusa		Prusa	
SKU	PRM-PLA-JET-1000		PRM-PETG-JET-1000		PRM-ASA-JET-850	
Orientation	Horizontal	Vertical	Horizontal	Vertical	Horizontal	Vertical
UTS (MPa)	50.8 ± 2.4	37.6 ± 4.0	47 ± 2	30 ± 5	42 ± 1	9 ± 1
YM (GPa)	2.2 ± 0.1	2.3 ± 0.1	1.5 ± 0.1	1.4 ± 0.1	1.6 ± 0.1	1.4 ± 0.1
Hardness (HV)	20.07± 0.21		15.15± 0.75		N/A	
Elongation at break (%)	2.9± 0.3	1.9± 0.3	5.1± 0.1	2.5± 0.5	3.3± 0.1	0.6± 0.1
Filament Diameter (mm)	1.75 ±0.015		1.75 ±0.02		1.75 ± 0.03	
Cost (£/kg) at the time of writing	26.99		26.99		31.75	

4.2.2 3D Printing Methodology

Samples were printed in batches of 15 using a Prusa I3Mk3 FDM printer (Prusa Research a.s.). Samples were designed in Solidworks and sliced in Ultimaker Cura 4.7 (Ultimaker B.V.). Figure 4.1 shows the two orientations relative to the build plate, which were printed to investigate the response

of tensile strength (horizontal build) and layer adhesion strength (vertical build) to gamma radiation. Standard printing parameters were used and kept identical between materials, except for the nozzle and build plate temperature, where supplier recommendations were used (Table 3).

Table 4.2 Sample printing parameters

Printing parameter	PLA	PETG	ASA
Infill (%)	100	100	100
Nozzle Temp (°C)	210	260	255
Bed Temp (°C)	65	90	100
Layer Height (mm)	0.2	0.2	0.2
Raster orientation (°)	± 45	± 45	± 45
Walls	2	2	2
Speed (mm/s)	60	60	60

The dimensions of the design, print orientations and resulting printed samples are shown in Figure 1a. The cell size constrained the dimensions of the samples within the chamber used to apply the gamma radiation. The size of each cell was 25 x 25 x 120 mm, and 5 samples were required to fit within each cell. The measured dimensions of the samples were larger than the CAD model, which has been attributed to overflow resulting from the 100% infill. The midsection's average cross-sectional area was 27.3 mm^2 (6.45 x 4.233 mm). This measurement was used for mechanical strength calculations. From the Cura slicing profile (Figure 4.2), infill in yellow, alternating raster angle of 45° with sequential layers, and the wall material in red (outer) and green (inner) can be seen. Wall material was the initial deposition path taken for each layer and follows the perimeter of the layer cross-section.

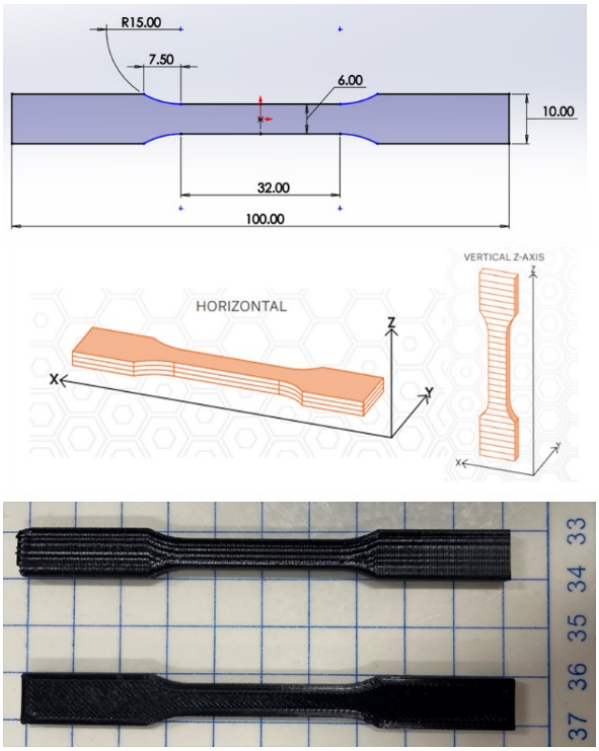

Figure 4.1 - Design dimensions, print orientations and photo of samples after fabrication (vertical sample (top), horizontal sample (bottom))

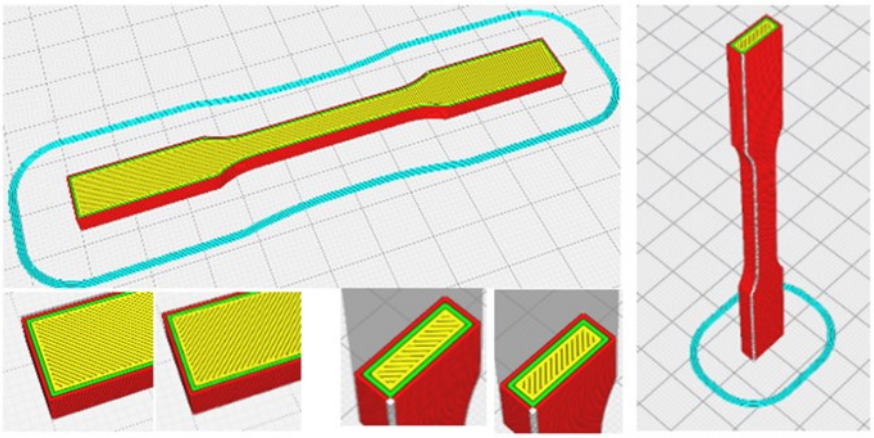

Figure 4.2 - Sample orientation slicing profile from Cura. Lower 4 photos show the change in raster angle with alternating layers

4.2.3 - Irradiation Of 3D Printed Parts

Irradiation of the samples was conducted at the Dalton Cumbria Facility (DCF) at The University of Manchester. Samples were exposed to gamma radiation using three high-activity sealed cobalt-60 sources in a Foss Therapy Services Inc. (California, USA) model 812 irradiator at room temperature. Absorbed dose rates were determined using an ion chamber, calibrated annually to

traceable international standards (Radcal Corporation Accu-Dose+ base unit equipped with ion chamber).

This work employed high radiation exposure levels to mimic extended deployment in highly radioactive zones or multiple sterilisations of medical apparatus. To allow for comparison between materials, PETG and ASA were irradiated to the same exposure, with similar dose rates as listed in Table 4.3. Note that PLA was exposed to significantly lower radiation dosages due to the sensitivity mentioned earlier. Samples were irradiated at varying dose rates from 22.4 Gy/min to 110 Gy/min. To control the radiation dose, samples were grouped into sets of five for repeat measurements and placed in specific cells within the chamber. The distance from the radiation source determined the dose rate. Irradiation took around two weeks.

Table 4.3 Radiation doses for 3D printed parts

Radiation level (MGy)	PLA		PETG		ASA	
	Dose (MGy)	Rate (Gy/min)	Dose (MGy)	Rate (Gy/min)	Dose (MGy)	Rate (Gy/min)
0	None	-	None	-	None	-
1	0.1	22.4	0.75	35	0.75	35.5
2	0.2	24.2	1.5	69	1.5	71.5
3	N/A	N/A	2.25	110	2.25	103.5

4.2.4 Infrared Spectroscopy And Mechanical Testing Of 3D Printed Parts

Infrared spectroscopy was conducted using a Perkin Elmer Frontier FT-IR spectrometer (Perkin Elmer, US) , Figure 4.3, in ATR configuration on PETG and ASA. A load of 70N was applied to the samples to ensure consistent contact with the infrared crystal. Each measurement was taken 20 times per sample, and three samples were tested for each material/exposure combination.

Tensile testing was carried out using a Hounsfield H25KS (Tinius Olsen Ltd, UK) Universal Testing Machine, Figure 4.3. Due to the constraints on dimensions previously mentioned, tensile testing was conducted following a modified version of the ISO 527 (37) standard with an extensometer used to measure strain. Dog bone samples were loaded into the grips with a separation of 45mm. The test was run with a strain rate of 1 mm/s. Five repeats (n=5) for each measurement were taken. Hardness testing was performed following the BS EN ISO-6507 (38) and ISO/TS 19278:2019 (39) standards. An Innova Test Vickers hardness testing rig (Innova Test, Netherlands) , Figure 4.3, was used to indent and measure the hardness. Four repeats were carried out on three samples (n = 12) for each exposure level and material. A load of 200-gram force and a dwell time of 15 seconds were used. For repeatability, a pyramidal indenter was pressed into the build plate surface of the horizontal build

samples, and the diagonal length was measured using a microscope to calculate hardness. Following mechanical testing, the fracture surface was inspected visually.

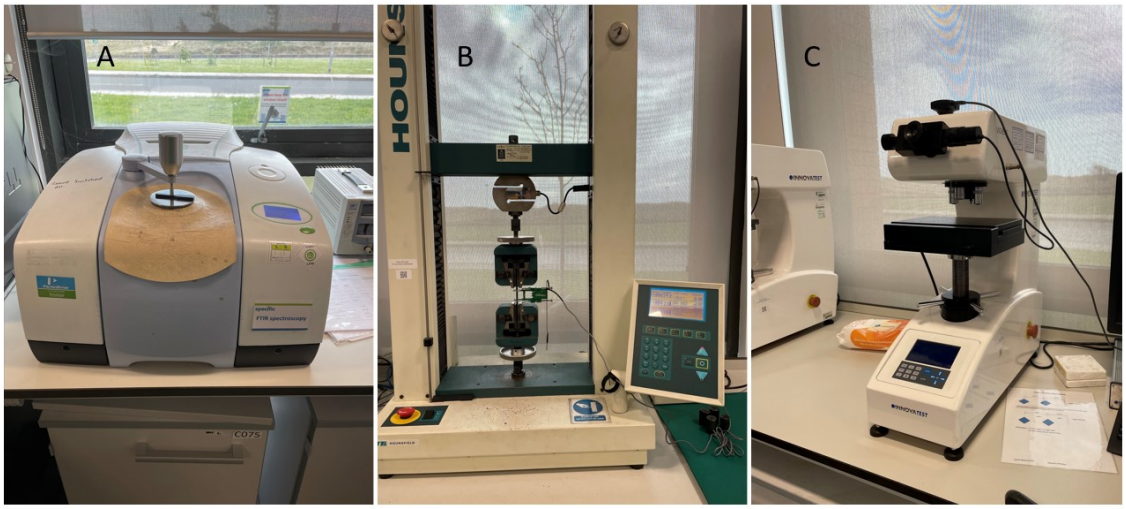

Figure 4.3 *- Testing apparatus A) Perkin Elmer Frontier FT-IR spectrometer. B) Hounsfield H25KS. C) Innova Test Vickers hardness testing rig*

5.3 Results

5.3.1 Infrared Spectroscopy

Infrared spectra of PETG and ASA before and after the various amounts of gamma exposure are shown in Figure 4.4. Key peaks and transmission per cent are itemised in Table 4.5.

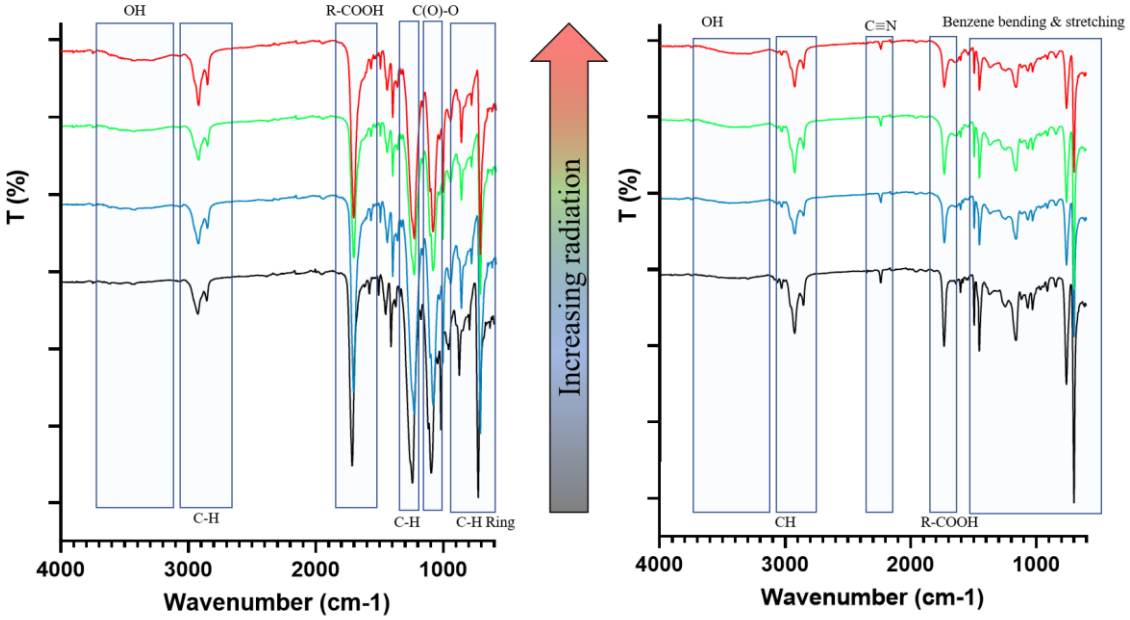

Figure 4.4 *-PETG (left) and ASA (right) Infrared spectra. Wavenumbers corresponding to specific bonds have been labelled*

PETG

Non-irradiated PETG showed a characteristic peak at 1712 cm^{-1} [89], corresponding to the carboxylic group, R−COOH. The peak at 724 cm^{-1} corresponds to the deformation of the C-H carbonyl substituents on the aromatic ring [90]. The peak seen at 1408 cm^{-1} corresponds to the CH in-plane bending of the ring [91], and 1240 cm^{-1} corresponds to the stretching of the ester groups C(O)-O [92]. The two peaks at 2925 cm^{-1} and 2855 cm^{-1} correspond to the C-H stretching [93] in PETG. Finally, the C-H stretching of the cyclohexylene ring was seen at 956 cm^{-1} [94].

Following irradiation, a new broad peak at 3293cm^{-1} corresponding to a hydroxyl group OH bond [80] [95] was observed. The two peaks associated with C-H stretching, 2855-2925 cm^{-1} and the peak associated with C-H bending, 1408 cm^{-1}, showed an increase in absorption at the highest exposure level suggesting the formation of CH bonds. For most of the other listed bonds, there was no clear trend of increased or decreased absorption with exposure over 0.75MGy.

ASA

ASA showed a characteristic peak at 1733 cm^{-1} corresponding to C=O stretching in the carboxyl group, a peak at 2239 cm^{-1} corresponding to C≡N stretching group [96], peaks at 1452, 1494, and 1602 cm^{-1} associated with the bending vibration of the benzene ring and 698, and 758 cm^{-1} corresponding to the stretching vibrations of the benzene ring [97] [98].

Similarly to PETG, the only new peak formation was observed at the 3300cm^{-1} wavelength, associated with an OH bond, again suggesting that cross-linking has occurred [80]. The 2293 cm^{-1} peak associated with the C≡N bond maintained the peak intensity with exposure. This is expected as triple bonds are considerably stronger than saturated bonds [99]. All other peaks decreased in intensity at the 0.75 MGy exposure level and remained lower than the control sample intensity up to the 2.25MGy exposure level.

Table 4.4. Key peaks from FT-IR analysis of PETG and ASA

Material	Bond	Wavenumber (cm^{-1})	Transmission (%) at radiation exposure (MGy)			
			0.0	0.75	1.5	2.25
PETG	RING C-H	724	70.74	69.12	77.09	72.23
	C-H Stretching cyclohexylene ring	956	89.83	88.4	91.58	89.39
	Ester C(O)-O Stretching	1240	72.46	71.64	79.63	74.28
	C-H Bending	1408	90.21	89.45	90.2	76.85
	Carbocyclic acid R-COOH	1712	74.79	74.39	81.76	71.12
	C-H stretching	2855	96.28	95.66	96.29	94.14
		2925	94.58	93.63	94.44	91.5
	OH Hydroxyl	3293	None	98	98.17	97.27
ASA	Benzene Stretching	698	69.36	81.13	77.35	82.67
		758	84.98	90.66	88.79	91.1
	Benzene bending	1452	89.24	93.21	91.91	93.5
		1494	92.64	95.45	94.71	95.67
		1602	96.98	97.89	97.25	97.37
	Carbocyclic acid R-COOH	1733	89.98	93.52	92.5	93.92
	C≡N	2239	98.17	98.86	98.47	98.88
	C-H stretching	2853	95.34	97.1	95.82	96.32
		2923	91.67	94.73	92.67	93.94
	OH	3300	None	98.78	98.66	98.24

5.3.2 PLA Tensile Testing Results Comparison To Literature

Previous literature has produced equations (Eq. 1-3) to predict the degradation of **horizontal** build PLA sample's mechanical properties when exposed to gamma radiation. In Figures 4.4, 4.5, and 4.6, horizontal build and vertical build samples have been plotted and compared to findings from West et al. [71], who tested PLA in a horizontal orientation up to 0.15 MGy of exposure. Equations presented have been normalised onto the non-irradiated result.

PLA samples were irradiated to 0.3 MGy. However, at high exposures, the samples became too brittle to test. Horizontal sample results up to 0.2 MGy and vertical sample results up to 0.1 MGy are shown.

In Figure 4.5, Eq. (1) predicts the UTS degradation of PLA when exposed to gamma radiation. A significant reduction in UTS is measured at 0.1MGy, reducing to 23% when compared to the non-

irradiated sample. Vertical sample UTS reduced to 15.7% when compared to the non-irradiated sample.

$$f(x) = A + B/(1 + C * \exp\left(\frac{x}{D}\right)) \quad (1)$$

Where A= 2.12 [MPa], B= 41.7 [MPa] (UTS at 0 kGy), C= 0.0500, and D= 30.20 [kGy], x = exposure to radiation [kGy] [71]

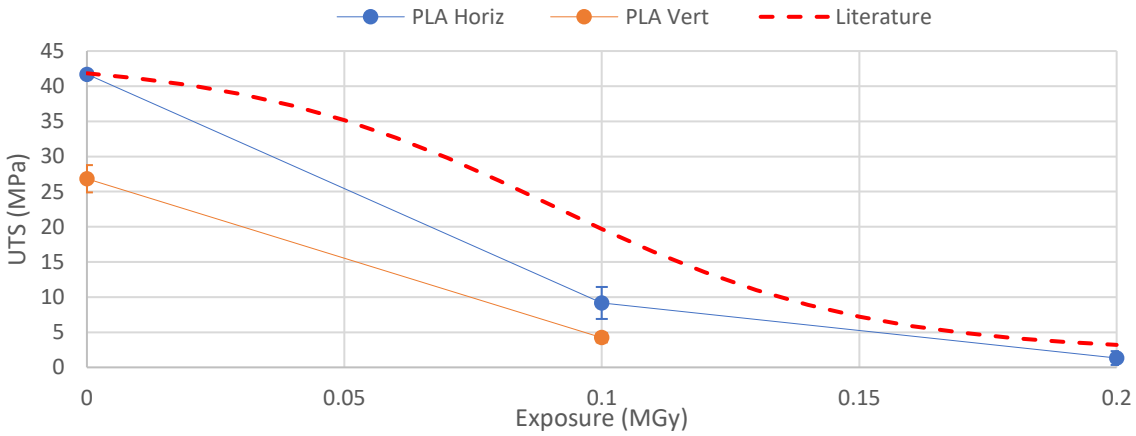

Figure 4.5 *– Ultimate tensile strength of PLA, recorded in tensile (Horizontal build) and layer adhesion (vertical build) planes. Results have been compared to literature from Eq.(1)*

In Figure 4.6, Eq. (2) predicts the maximum strain degradation of PLA when exposed to gamma radiation. Similarly to UTS significant reduction in the maximum strain was observed, with the horizontal sample reducing to 9.5% and vertical samples reducing to 11.8% at 0.1 MGy compared to the non-irradiated samples.

$$f(x) = A * \exp\left(-\frac{x}{B}\right) \quad (2)$$

Where A = 3.698 [%] (Max strain at 0 kGy) , B = 60.9 [kGy], x = exposure to radiation [kGy] [71]

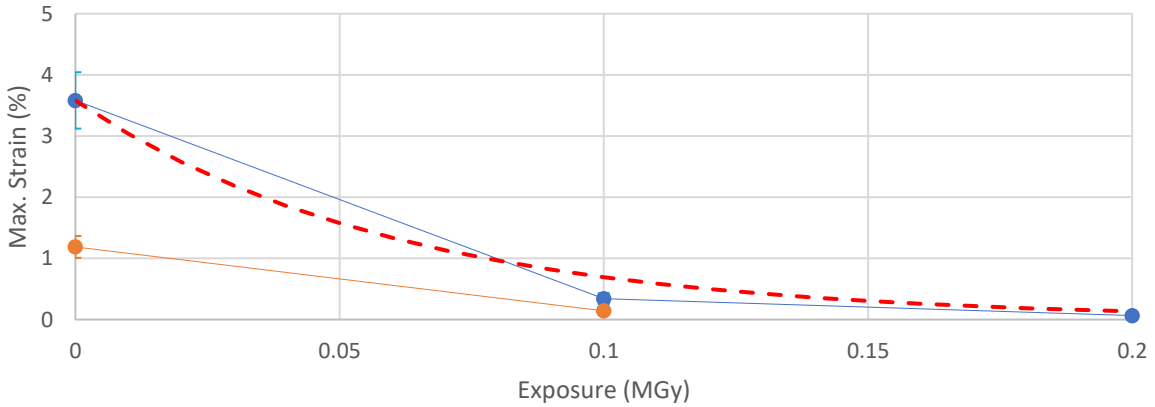

Figure 4.6 *- The maximum strain of PLA is recorded in tensile (Horizontal build) and layer adhesion (Vertical build) planes. Results have been compared to literature from Eq.(2)*

Finally, in Figure 4.7, Eq. (3) predicts the Young's modulus degradation of PLA when exposed to gamma radiation. Increases in the Youngs modulus are observed, which is in line with previous literature. For horizontal samples, an increase of 3.3% and for vertical samples, an increase of 21.25% was observed at 0.1MGy compared to previous literature.

$$f(x) = A + Bx \tag{3}$$

Where A = 2941.5 [MPa] (YM at 0.0 MGy), B = 1.77 [MPa/kGy], and x = exposure to radiation [kGy] [71]

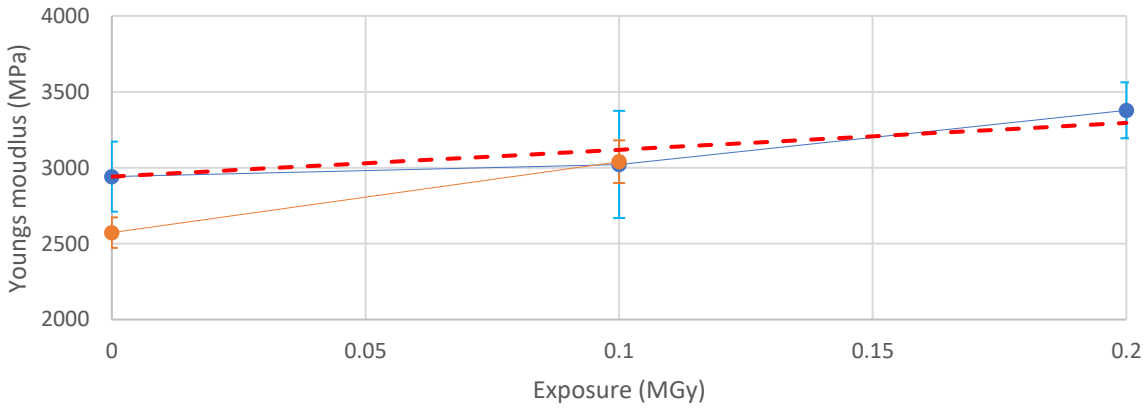

Figure 4.7 *- Young's modulus of PLA, recorded in tensile (Horizontal build) and layer adhesion (Vertical build) planes. Results have been compared to literature from Eq.(3)*

5.3.3 Mechanical Testing Of PETG And ASA

Stress-strain curves from tensile testing from all PETG and ASA samples have been overlaid and are presented in Figures 4.8 & 4.9. Results for horizontal build (primarily representative of material tensile strength) and vertical build (primarily representative of layer adhesion strength) are plotted on separate graphs. Increasing exposure has been offset on the strain axis to compare the data at different radiation exposure levels.

Regardless of the choice of material or degree of exposure to radiation, the levels of stress and strain at failure were substantially lower for the vertical build than the horizontal build. ASA samples showed generally lower levels of stress and strain at failure than their PETG counterparts. Additionally, both materials decreased in UTS and maximum strain with increasing exposure to gamma radiation. A slight increase in Young's modulus and hardness was observed with increased exposure to radiation. Non-irradiated horizontal build samples demonstrated signs of ductility, as reported previously [100].

While non-irradiated vertical build samples demonstrated brittle failure, as reported in previous literature [101].

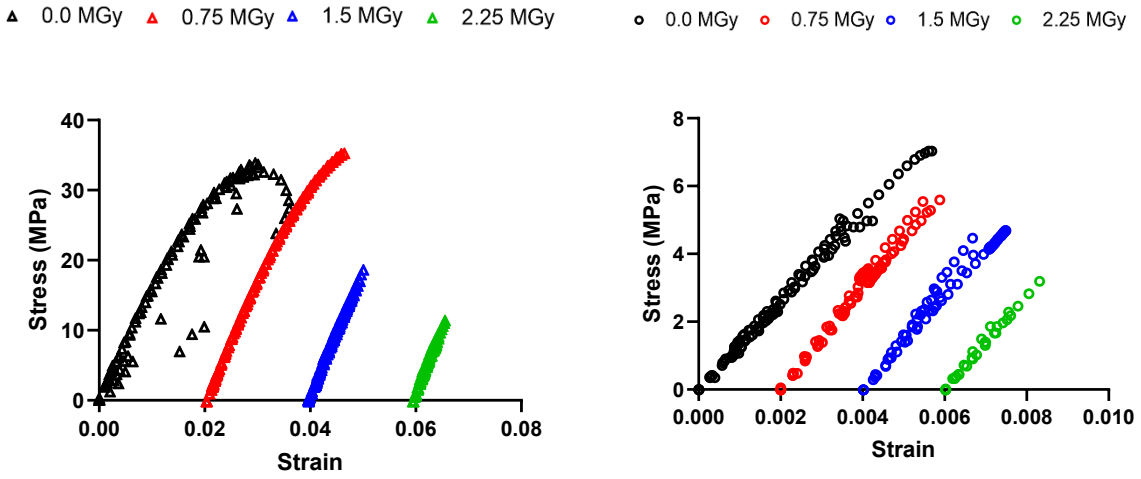

Figure 4.8 *– Stress-Strain curve for PETG horizontal build (left), vertical build (right) increased exposure offset on the strain axis*

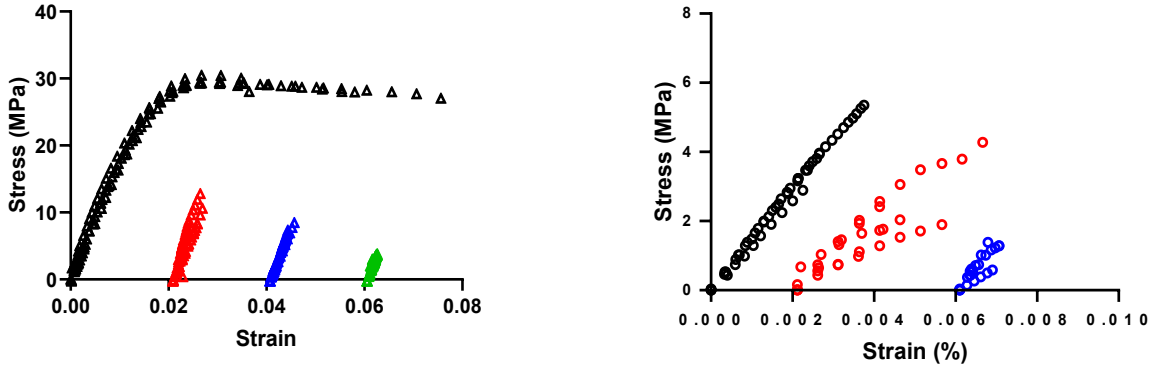

Figure 4.9 *- Stress-Strain curve for ASA horizontal build (left), vertical build (right) increased exposure offset on the strain axis*

The key mechanical properties (UTS, maximum strain, Young's modulus, and hardness) are shown in Figures 4.10-4.13.

Compared to supplier data sheets in Section 4.1, there are differences in the non-irradiated samples for both horizontal and vertical samples. These differences are further discussed in section 4.3. For both materials, decreases in UTS and maximum strain were observed, and a slight increase in Young's modulus and hardness was observed with increased exposure to radiation. ASA samples showed

generally lower levels of stress and strain at failure than their PETG counterparts. Vertical build samples had lower UTS, maximum strains, and Youngs moduli compared to the horizontal samples.

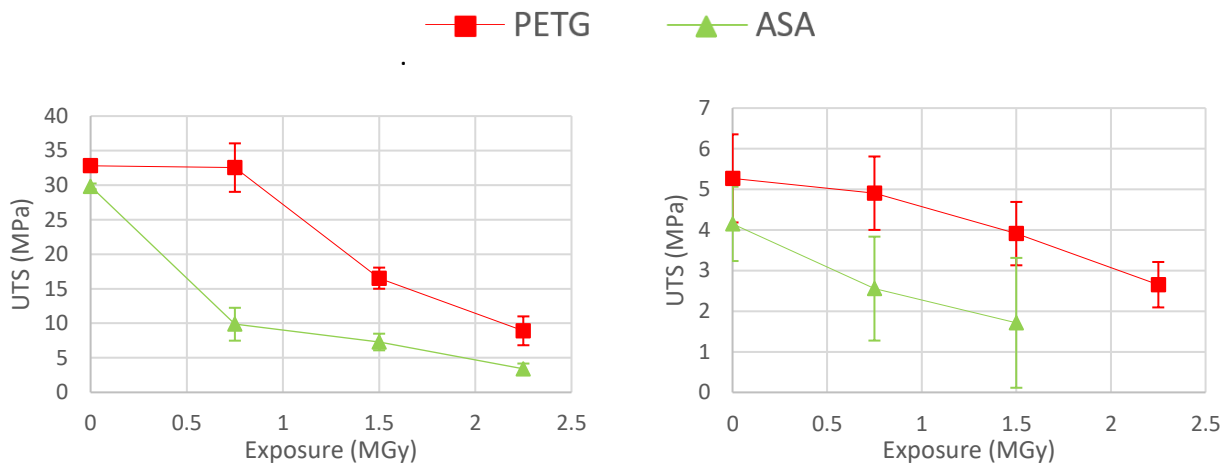

Figure 4.10 *– Change in UTS with increasing exposure to gamma radiation. Horizontal build (Left) vertical build (Right)*

PETG horizontal build maintained the control samples' UTS of 32MPa at 0.75 MGy, ultimately dropping to 8.91MPa at 2.25 MGy. ASA horizontal builds reduced significantly in UTS from 30 to 9.9MPa at 0.75MGy and ultimately reduced to 3.5 MPa at 2.25 MGy. Vertical build samples achieved significantly lower UTS when compared to horizontal build. Similar decreases in UTS with increasing exposure to radiation were observed, with PETG reducing from 5.3 to 2.7 MPa at 2.2 5MGy and ASA reducing from 4.2 to 1.7 MPa at 1.5 MGy.

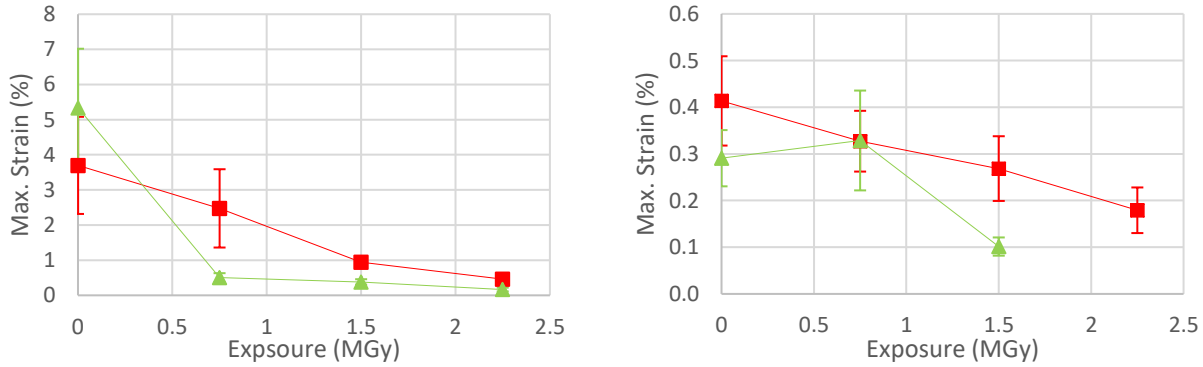

Figure 4.11 *- Change in maximum strain with increasing exposure to gamma radiation. Horizontal build (Left) vertical build (Right)*

For both materials, the maximum strain was reduced with increased exposure to radiation, agreeing with findings from stress-strain curves that radiation has induced embrittlement in the materials. PETG horizontal builds reduced from 3.9% to 0.46% at 2.25 MGy. While ASA reduced in maximum strain significantly from 5.3% to 0.5 % at 0.75MGy, ultimately reducing to 0.17% at 2.25MGy. Vertical

build samples similarly reduced in maximum strain with PETG reducing from 0.41% to 0.18 % at 2.25 MGy and for ASA from 0.29% to 0.10%

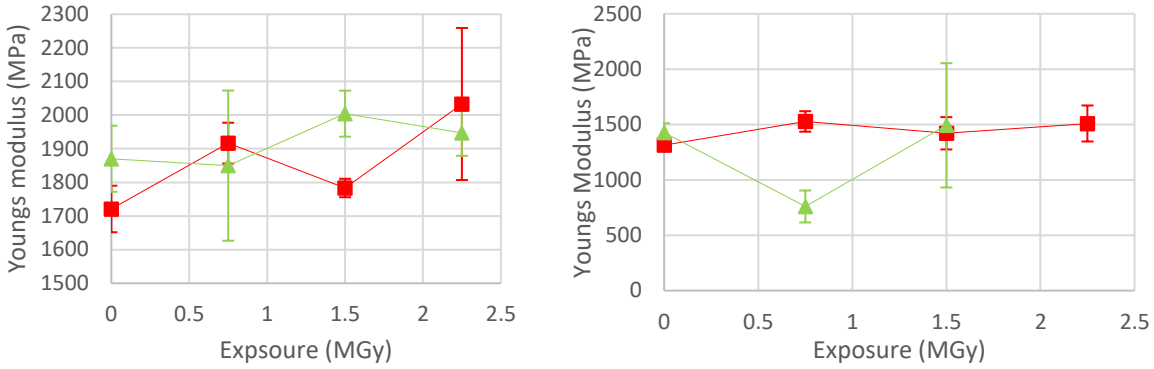

***Figure 4.12**- Change in Youngs modulus with increasing exposure to gamma radiation. Horizontal build (Left) vertical build (Right)*

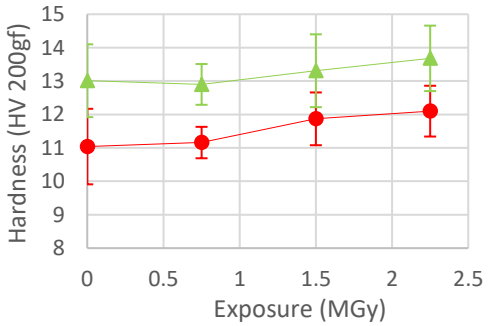

***Figure 4.13** - Change in hardness with increasing exposure to gamma radiation*

Increases in both Young's modulus and hardness averages were observed. However, the variation in measurement makes it difficult to conclude the actual effect radiation has had on the elastic and hardness properties of the materials. Variance in results has been attributed to dislocation within the macrostructure of the material due to the fabrication method. Generally, there is more variance in vertical build results when compared to horizontal. Additionally, there is a large variance in the horizontal build Young's modulus results. Variance in the hardness results has been attributed to different build plate adhesion between samples. Build plate heating is not equal across the build plate surface, leading to better adhesion for the samples in the centre of the build volume when compared to the samples on the perimeter of the print batch

5.3.4 Visual Inspection Of Fracture Surfaces

Images of fractured 3D printed PETG samples are shown in Figures 4.14 & 4.15. Nonirradiated samples are compared to samples irradiated at the highest level (2.25MGy).

The appearance of the fracture for horizontal build samples changed following irradiation. Nonirradiated samples, Figures 4.13 a) & c), had rough surfaces, distinct infill and wall regions and evidence of thinning occurring after fracture, indicative of ductile failure. Following irradiation, Figures 4.13 b) & d), fracture surfaces were flatter, smoother and showed no sign of local thinning, corresponding with observations from tensile testing and showing that gamma radiation-induced embrittlement in the material.

For the vertical build, Figure 4.14, all fracture surfaces occurred between layer boundaries, creating flat fracture surfaces with no evidence of necking. From the front view images, the macrostructure of the deposition lines can be seen. There is no noticeable qualitative change as a result of radiation exposure. Again, this corresponds with the consistent brittle failure mode in the vertical build samples. Similar results were recorded for ASA.

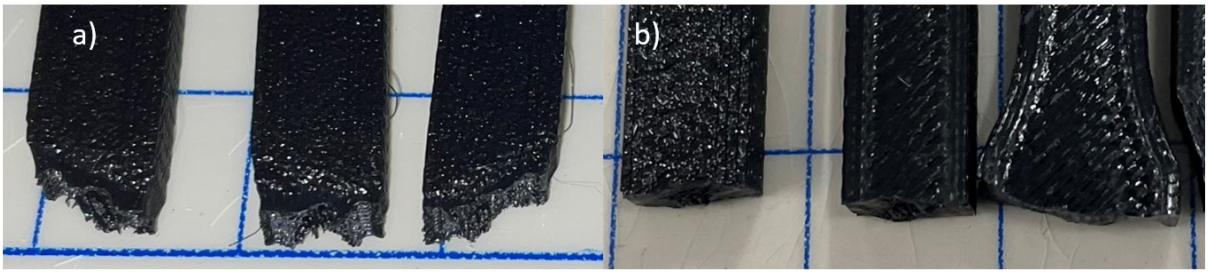

Figure 4.13 *– PETG horizontal build fracture surfaces. a) Non-irradiated, b) 2.25 MGy exposure*

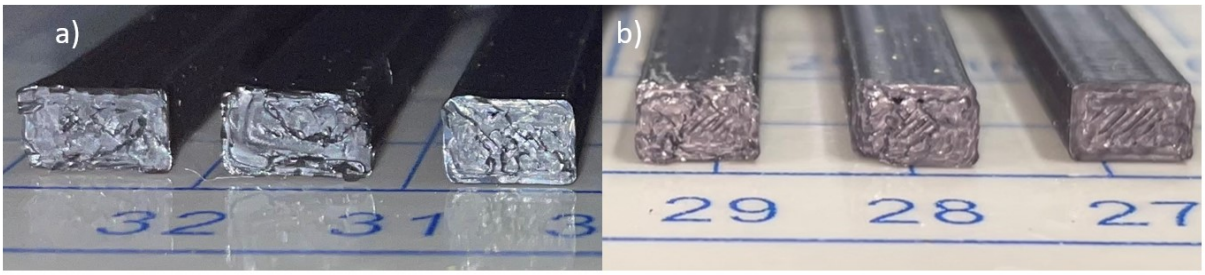

Figure 4.14 *- PETG vertical build fracture surfaces. a) Non-irradiated, b) 2.25 MGy exposure*

5.4 Discussion

There are differences in mechanical properties measured between the work presented in this chapter and the expected results from supplier data sheets. All samples were fabricated using supplier printing temperatures. However, other printing parameters, such as infill type, layer height, number of walls and print speed, were not provided. It has been shown that changes in the printing parameters can drastically affect mechanical properties [56]. For PLA, the UTS and maximum strain for horizontal and vertical build samples are slightly lower than expected from supplier data sheets. Regarding PETG and ASA, the UTS result for both materials is lower than expected for horizontal builds. The maximum strain for PETG is lower, and for ASA higher than expected. Young's modulus is slightly higher than expected for both materials. The ASA UTS and maximum strain results for vertical builds are lower, and the Youngs modulus is as expected from the supplier datasheet. The most significant discrepancy between supplier properties and those measured in this chapter is for vertical build PETG. The UTS and maximum strain is 16% of the expected values.

In Contrast, for PETG and ASA, comparing previously published work to the results presented in this chapter, the UTS was similar or lower for non-irradiated PETG and slightly lower maximum strain and Young's modulus [102] [103]. Previously published work for non-irradiated ASA samples measured similar or slightly higher UTS and higher maximum strain [104] [105] compared to this chapter's results. Moreover, previous work has identified the difficulties in testing vertical build samples due to the fragile nature and inconsistency in layer adhesion at high Z coordinates [101]. Little research has been conducted on PETG or ASA samples printed in the vertical orientation.

There is a noticeable variance between previously published work, supplier data sheets, and work presented in this thesis. This has been attributed to a lack of standardisation in the AM space. As discussed, printing parameters can significantly affect the mechanical properties of parts. At the time of writing, no tensile testing standard for 3D printed samples exists. This has led to a large variance in reported mechanical properties in nonirradiated 3D printed samples.

For irradiated PLA, comparing tensile testing results to equations produced by literature, reductions in UTS and maximum strain and increases in Young's modulus were measured in line with the decay rate predicted by equations [71]. This gives confidence in the experimental methodology. Differences in the decay rate are attributed to material, print parameters, and dose rate. It is also noted that significant degradation in the UTS and maximum strain of PLA were recorded at just 0.1 MGy, confirming findings from the literature that PLA is ‘hyper sensitive’ to gamma radiation.

Research suggests that the AM fabrication process does not alter functional groups present in 3D printed parts when compared to bulk material [102]. However, gamma radiation has been shown to alter the intermolecular bonding within polymers [70]. Crosslinking is known to induce embrittlement in the material, reducing the maximum strain and increasing the Young's modulus [62]. In contrast to cross-linking, chain scission leads to a lack of elastic properties, reducing the Youngs modulus and elastic properties of the material. Increases in these properties would be an indication of crosslinking, and decreases would be an indication of chain scission [62]. These mechanisms counteract each other, making it difficult to definitively identify a primary mechanism from tensile results.

For PETG and ASA, the spectra produced by FTIR suggest evidence of crosslinking occurring in both materials. Indicated by the formation of the broad peak located at 3300 cm^{-1} [71], corresponding to the hydroxyl group OH bond [80] [95]. From the PETG spectra, increases in peak intensity in bonds corresponding to CH groups further indicate the radicalisation of hydrogen electrons and the reforming of new bonds. Mechanical testing agrees with the findings from FTIR. Embrittlement of the materials is evidenced by the decrease in maximum strain and increase in Young's modulus. Additionally, chain scission is expected to occur alongside crosslinking, evidenced by the decrease in UTS and loss of elastic properties with increasing exposure to radiation. Furthermore, visual inspection of the fracture surfaces following irradiation indicated the horizontal build failure modes increased in brittleness with exposure. At the same time, vertical build fracture surfaces showed minimal change with exposure. This implies that the failure mechanism in the layer adhesion remains dependent on the interlayer bonding strength, which can be improved by optimising printing parameter. This agrees with mechanical testing where the relative change in mechanical properties between non-irradiated and highly irradiated samples was higher for horizonal build samples. At the time of writing there exist no research into the effect high levels gamma radiation have on the layer adhesion strength.

Previous work has focused on the robustness of PLA and ABS to gamma radiation. Table 4.6 compares previous work investigating the radiation response of PLA and ABS to results from PETG and ASA in this thesis. Research has shown PLA to become unsuitable for functional use at exposure over 0.05MGy [71] [70] [78]. In comparison, ABS has been shown to be more resistant to radiation, increasing in UTS and maximum strain at exposures lower than 0.05 kGy [81] [82]. However, at higher dosages, above 1 MGy, ABS significantly reduced in UTS and maximum strain. The results presented in this chapter show that PETG performs better than PLA and ABS in mechanical testing. ASA performs better than PLA and similarly to ABS. Note that direct comparison to previous work is difficult due to differences in dose rate and print parameter settings, i.e. work from [81] used thicker 2mm walls. Ultimately, the results demonstrate the higher robustness of PETG to radiation compared to other similarly priced materials on the market.

Table 4.5 A comparison between literature and work presented in this thesis of the mechanical response in UTS and maximum strain of different materials at increased exposure to radiation, around 1.5MGy and above 2MGy. No published results for PLA at the doses listed.

Dose (MGy)	Material	UTS (MPa)	Maximum Strain (%)	Ref
1.4	PLA	Negligible	Negligible	Thesis
	ABS	8.1	0.3	[81]
1.5	PETG	16.53	0.94	Thesis
	ASA	7.29	0.38	Thesis
2.25	PETG	8.91	0.461	Thesis
	ASA	3.4	0.164	Thesis
2.628	PLA	Negligible	Negligible	Thesis
	ABS	8	NA	[70]

The research presented has investigated dog bone samples printed in two orientations. This has provided insight into both the tensile and layer adhesion strengths response to increased exposure. While this is a controlled geometry, the findings are transferable to real-world applications as the mechanisms occurring on the microscopic scale will be similar no matter the chosen geometry. Regarding the impact for Lynkeos, the findings presented will influence the material choice for deployment in the Muon Imaging System. Previous work by 3DScint used PLA to fabricate the channel structure. From previously published work and the work in this thesis, PLA has been shown to be a poor choice for channel fabrication.

5.5 Radiation Testing Conclusion

Research presented has indicated that the material choice will affect the mechanical response to gamma radiation exposure. PETG has been shown to be a promising material for deployment in radioactive areas, maintaining a UTS up to 0.75 MGy. This equates to a month of operation in Fukushima or half a year in close proximity to spent nuclear waste containers. These results are advantageous for Lynkeos and their MIS as PETG has shown to be significantly more robust than PLA, the previous material used by 3D Scint. However, higher dosages from prolonged exposure are likely to lead to a significant reduction in mechanical properties. This must be considered during the operation and maintenance of 3D-printed parts in radioactive areas; it is recommended that fibre channel inspection will be required three times a year.

Chapter 6: Conclusion

This thesis explored the feasibility of adopting AM into the fabrication process of muon imaging system structural components. The research has built upon preliminary design proposals by 3DScint. This preliminary design proposal previously demonstrated the feasibility for AM to manufacture a muography system however limitations with designs were identified:

- The design was unable to be scaled to fit customer needs.
- A large footprint was required due to external electronics. External electronics also reduce the efficiency of detection.
- High angular spacing between fibres, reduces the probability of muon detection.

Following the identification of limitations with the preliminary design, A PDS was produced to identify **limitations, constraints and objectives** with design proposals. A novel design solution was proposed to integrate the electronics and incorporate modularity into the design. The design has proven successful in addressing the limitations identified with the preliminary design proposal. Through the adoption a modular design the **detection area increased by 335%** compared to the preliminary design proposal. Integrating electronics **increased the compactness and portability** of the design. The novel design was successful in recording passive background radiation and locating a beta source emitter within the detection area. The results demonstrate that AM designs can **reliably measure cosmic ray interaction** and improve the scaling potential and compactness of the system. Further limitations with the novel design were identified and solutions to limitations focused on the fibre channel components. The improvements reviewed the geometry and manufacturing process of the component. By leveraging AM advantages, the **print time has decreased by 38%** and the **material weight has decreased by 36**%. Additionally, new channel geometry has **improved the installation and positioning of fibres**.

Results from both the novel design and further improvements have enhanced early commercial viability and analysed economic factors such as fabrication and the reuse of expensive scintillating fibres. Ultimately, the results have proposed new design solutions for Lynkeos to provide a more competitive service.

Significant improvements to the material choice have been made. This work has demonstrated PETG's superior robustness to gamma radiation giving confidence in its ability to maintain performance for extended operation times.

Additional findings from radiation testing are summarised below:

- All polymers experience mechanical degradation at high exposures to gamma radiation.
- Exposure to radiation leads to embrittlement of polymeric materials, which is more apparent in the tensile strength when compared to the layer adhesion strength.
- Materials containing aromatic rings (PETG and ASA) demonstrated significantly more robustness to radiation when compared to materials with saturated bonds (PLA).
- PLA is hyper-sensitive to radiation and loses 78% of the UTS at exposures of only 0.1MGy.
- PETG surpassed the mechanical robustness of ASA (this thesis) and ABS (Literature), maintaining a similar UTS when irradiated to 0.75 MGy compared to the non-irradiated samples. Equivalent to half a year of operations near nuclear waste containers.

The work presented in this thesis has provided recommendations to Lynkeos to help address concerns with scaling up their muography technologies. The work has successfully deployed an AM detector prototype and provided insight into the design and material solutions required for full-scale deployment. The research presented has focused on the system's structural components, and improvement has been targeted to industrial needs through a specified criterion. However, further technological improvements are required for the wide-scale adoption of muography. Such improvements include but are not limited to:

- More complex detector shapes such as a nonplanar borehole detector for subterranean inspection. This will open new markets for the deployment of muography systems.
- Real-world testing of 3D printed imaging systems should be carried out. This should involve fabricating a detector with an active area of at least $1m^2$, which will give insight into the stiffness of the assembly and the long-term effect of exposure to nuclear waste containers.
- Further radiation robustness testing should inspect materials' flexural modulus and glass transition temperature following exposure to high-intensity gamma radiation.

Large-scale muography systems have significant potential to positively impact society in various ways, including better characterisation of nuclear waste, leading to safer and cheaper long-term storage, better insight into the structural integrity of ageing civil structures, and more cost-effectively mining of new ore deposits. The work presented in this thesis will help improve the adoption of muography in these existing NDT markets by reducing the cost and improving the scalability and transportability of the technology.

Bibliography

[1] Non-Destructive Testing Market Outlook, Size (2022 - 27) | Industry Growth [Internet]. [cited 2022 Jul 26]. Available from: https://www.mordorintelligence.com/industry-reports/global-non-destructive-testing-market-industry

[2] Niederleithinger E, Gardner S, Kind T, Kaiser R, Grunwald M, Yang G, et al. Muon tomography of a reinforced concrete block – first experimental proof of concept. arXiv. 2020;1–15. , doi: https://doi.org/10.48550/arXiv.2008.07251

[3] George EP, Evans J. Observations of cosmic-ray events in nuclear emulsions exposed below ground. Proc Phys Soc Sect A. 1950;63(11):1248–64. , doi: 10.1088/0370-1298/63/11/310

[4] Alvarez LW, Anderson JA, El Bedwei F, Burkhard J, Fakhry A, Girgis A, et al. Search for hidden chambers in the pyramids. Science (80-). 1970;167(3919):832–9. , doi: 10.1126/science.167.3919.832

[5] Marchant J. Cosmic-ray particles reveal secret chamber in Egypt's Great Pyramid. Nature. 2017;(November). , doi: 10.1038/nature.2017.22939

[6] Kaiser R, Kaiser R. Muography : overview and future directions Subject Areas : Author for correspondence : Philos Trans R Soc A Math Phys Eng Sci. 2019;377. , doi: https://doi.org/10.1098/rsta.2018.0049.

[7] Lynkeos Technologies Limited [Internet]. Available from: https://www.lynkeos.co.uk/

[8] Mahon D, Clarkson A, Gardner S, Ireland D, Jebali R, Kaiser R, et al. First-of-a-kind muography for nuclear waste characterization. , doi: 10.1098/rsta.2018.0048

[9] Clifford BR, Clarkson A, Connor DO, Gardner S, Gray R, Kaiser R, et al. 3DSCINT – Commodification of Scintillator Detectors using 3D Printing Techniques. Welsh Cent Print Coating, Coll Eng Swansea Univ Swansea Univ. :1–5.

[10] Neddermeyer SH, Anderson CD. Nature of cosmic-ray particles. Rev Mod Phys. 1939;11(3–4):191–207. , doi: 10.1103/RevModPhys.11.191

[11] Zhang ZX, Enqvist T, Holma M, Kuusiniemi P. Muography and Its Potential Applications to Mining and Rock Engineering. Rock Mech Rock Eng [Internet]. 2020;53(11):4893–907. , doi: 10.1007/s00603-020-02199-9

[12] Nagamine K. Introductory Muon Science. Introductory Muon Science. Cambridge university press; 2003. , doi: 10.1017/cbo9780511470776

[13] G.Bonomi P.Checchia M.D'Errico D.Pagano G.Saracino. Applications of cosmic-ray muons. Prog Part Nucl Phys. 2020;112. , doi: https://doi.org/10.1016/j.ppnp.2020.103768

[14] Carbone D, Gibert D, Marteau J, Diament M, Zuccarello L, Galichet E. An experiment of muon radiography at Mt Etna (Italy). Geophys J Int. 2013;196(2):633–43. , doi: 10.1093/gji/ggt403

[15] Tanaka HKM, Miyajima H, Kusagaya T, Taketa A, Uchida T, Tanaka M. Cosmic muon imaging of hidden seismic fault zones: Rainwater permeation into the mechanical fractured zones in Itoigawa-Shizuoka Tectonic Line, Japan. Earth Planet Sci Lett [Internet]. 2011;306(3–4):156–62. , doi: 10.1016/j.epsl.2011.03.036

[16] Borozdin K, Asaki T. Information extraction from muon radiography data. Proc Int Conf … [Internet]. 2004;836(May 2014).

[17] Muon Tomography | CMS Experiment [Internet]. [cited 2022 Jul 26]. Available from: https://cms.cern/content/muon-tomography

[18] Rengifo Gonzáles J. Design and simulation of a cost-affordable Cosmic Ray Muon Tomographer. 2021;(Icrc):249. , doi: 10.22323/1.395.0249

[19] Baesso P, Cussans D, Thomay C, Velthuis J. Toward a RPC-based muon tomography system for cargo containers. J Instrum. 2014;9(10). , doi: 10.1088/1748-0221/9/10/C10041

[20] Al-Dulaimi A, Al-Hamadany A, Al-Gherairy M, Al-Zuhairi R, Al-Timimi A. Study of the Scintillation Detector Efficiency and Muon Flux. Int J Appl Eng Res [Internet]. 2018;13(9):7037–41.

[21] Burns J, Quillin S, Stapleton M, Steer C, Snow S. A drift chamber tracking system for muon scattering tomography applications. J Instrum. 2015;10(10). , doi: 10.1088/1748-0221/10/10/P10041

[22] Jonkmans G, Anghel VNP, Jewett C, Thompson M. Annals of Nuclear Energy Nuclear waste imaging and spent fuel verification by muon tomography. Ann Nucl Energy [Internet]. 2013;53:267–73. , doi: 10.1016/j.anucene.2012.09.011

[23] Clarkson A, Hamilton DJ, Hoek M, Ireland DG, Johnstone JR, Kaiser R, et al. Nuclear Instruments and Methods in Physics Research A GEANT4 simulation of a scintillating- fi bre tracker for the cosmic-ray muon tomography of legacy nuclear waste containers. Nucl Inst Methods Phys Res A [Internet]. 2014;746:64–73. , doi: 10.1016/j.nima.2014.02.019

[24] Jol HM. Ground Penetrating Radar Theory and Applications. Elsevier Science & Technology; 2008. 545 p. , doi: https://doi.org/10.1016/B978-0-444-53348-7.X0001-4

[25] Bergmann RB, Bessler FT, Bauer W. Non-Destructive Testing in the Automotive Supply Industry- Requirements, Trends and Examples Using X-ray CT. Proc ECNDT 2006 Conf. 2006;1–10.

[26] Ramesh N, Hawron M, Martin C, Bachri A. Flux Variation of Cosmic Muons. J Ark Acad Sci [Internet]. 2012;65(May).

[27] Powell BCF, Ph D, Occhialini GPS. A New Photographic Emulsion for the Detection of Fast Charged Particles A New Photographic Emulsion for the Detection of Fast Charged Particles. 1946;

[28] Oláh L, Tanaka HKM, Takao O, Varga D. High-definition and low-noise muography of the Sakurajima volcano with gaseous tracking detectors. 2018;(February):29–33. , doi: 10.1038/s41598-018-21423-9

[29] Bonechi L, Ambrosino F, Cimmino L, Alessandro RD, Mori N, Noli P, et al. A possible point of contact between cosmic ray physics and archaeology : muon absorption radiography at the Tharros Phoenician-Roman site. 2017;1–5. , doi: 10.4401/ag-

[30] GScan [Internet]. Available from: https://gscan.eu/

[31] Access O. Density imaging of volcanos with atmospheric muons Density imaging of volcanos with atmospheric muons. 2012; , doi: 10.1088/1742-6596/375/5/052019

[32] Ideon [Internet]. Available from: https://ideon.ai/

[33] MINFOF. Edition 2018. state 3D Print [Internet]. 2018;1–29.

[34] Charles W. Hull, Arcadia C. APPARATUS FOR PRODUCTION OF THREE-DMENSONAL OBJECTS

BY STEREO THOGRAPHY. Vol. 716. 4,575,330, 1986.

[35] Deckard CR. METHOD AND APPARATUS FOR PRODUCING PARTS BY SELECTIVE SNTERNG. 4,863,538, 1989. p. United States Patent No. 4,863,538, filed October.

[36] S. Scott Crump, Minnetonka M. APPARATUS AND METHOD FOR CREATING THREE-DIMENSIONAL OBJECTS. Vol. 28, BUNSEKI KAGAKU. 5,121,329, 19992. p. 195–6.

[37] Dilberoglu UM, Gharehpapagh B, Yaman U, Dolen M. The Role of Additive Manufacturing in the Era of Industry 4.0. Procedia Manuf [Internet]. 2017;11(June):545–54. , doi: 10.1016/j.promfg.2017.07.148

[38] ISO/ASTM. Additive Manufacturing - General Principles Terminology (ASTM52900). Rapid Manuf Assoc [Internet]. 2013;10–2. , doi: 10.1520/F2792-12A.2

[39] Wong K V., Hernandez A. A Review of Additive Manufacturing. ISRN Mech Eng. 2012;2012:1–10. , doi: 10.5402/2012/208760

[40] Guo N, Leu MC. Additive manufacturing : technology , applications and research needs. 2013;8(3):215–43. , doi: 10.1007/s11465-013-0248-8

[41] Solomon IJ, Sevvel P, Gunasekaran J. A review on the various processing parameters in FDM. Mater Today Proc [Internet]. 2020;37(Part 2):509–14. , doi: 10.1016/j.matpr.2020.05.484

[42] The Free Beginner's Guide - 3D Printing Industry [Internet]. [cited 2022 Aug 16]. Available from: https://3dprintingindustry.com/3d-printing-basics-free-beginners-guide#02-history

[43] Comparison of tribological behaviour for Nylon6-Al-Al2O3 and ABS parts fabricated by fuseddeposition modelling.pdf.

[44] Nikzad M, Masood SH, Sbarski I. Thermo-mechanical properties of a highly filled polymeric composites for Fused Deposition Modeling. Mater Des [Internet]. 2011;32(6):3448–56. , doi: 10.1016/j.matdes.2011.01.056

[45] Castles F, Isakov D, Lui A, Lei Q, Dancer CEJ, Wang Y, et al. Microwave dielectric characterisation of 3D-printed BaTiO3/ABS polymer composites. Sci Rep. 2016;6(March):1–8. , doi: 10.1038/srep22714

[46] Shemelya CM, Rivera A, Perez AT, Rocha C, Liang M, Yu X, et al. Mechanical, Electromagnetic, and X-ray Shielding Characterization of a 3D Printable Tungsten–Polycarbonate Polymer Matrix Composite for Space-Based Applications. J Electron Mater. 2015;44(8):2598–607. , doi: 10.1007/s11664-015-3687-7

[47] Mohan N, Senthil P, Jayanth N. A review on composite materials and processparameters optimisation for the fused depositionmodelling process.pdf. Virtual Phys Prototyp. 2017;12:47–59. , doi: 10.1080/17452759.2016.1274490

[48] Tekinalp HL, Kunc V, Velez-Garcia GM, Duty CE, Love LJ, Naskar AK, et al. Highly oriented carbon fiber-polymer composites via additive manufacturing. Compos Sci Technol [Internet]. 2014;105:144–50. , doi: 10.1016/j.compscitech.2014.10.009

[49] Zhong W, Li F, Zhang Z, Song L, Li Z. Short fiber reinforced composites for fused deposition modeling. Mater Sci Eng A. 2001;301(2):125–30. , doi: 10.1016/S0921-5093(00)01810-4

[50] Rankouhi B, Javadpour S, Delfanian F, Letcher T. Failure Analysis and Mechanical Characterization of 3D Printed ABS With Respect to Layer Thickness and Orientation. J Fail Anal Prev. 2016;16(3):467–81. , doi: 10.1007/s11668-016-0113-2

[51] Magdum Y, Pandey D, Bankar A, Harshe S, Parab V, Mahesh M, et al. Process Parameter Optimization for FDM 3D Printer. Int Res J Eng Technol [Internet]. 2008;(April):1472.

[52] Saini M. Optimization the process parameter of FDM 3D printer using Taguchi method for improving the tensile strength. Int J All Res Educ Sci Methods. 2019;7(4):2455–6211.

[53] Török J, Törökova M, Duplakova D, Murcinkova Z, Duplak J, Kascak J, et al. Advanced configuration parameters of post processor influencing tensile testing PLA and add-mixtures in polymer matrix in the process of FDM technology. Appl Sci. 2021;11(13). , doi: 10.3390/app11136212

[54] Ćwikła G, Grabowik C, Kalinowski K, Paprocka I, Ociepka P. The influence of printing parameters on selected mechanical properties of FDM/FFF 3D-printed parts. IOP Conf Ser Mater Sci Eng. 2017;227(1). , doi: 10.1088/1757-899X/227/1/012033

[55] Sood AK, Ohdar RK, Mahapatra SS. Experimental investigation and empirical modelling of FDM process for compressive strength improvement. J Adv Res [Internet]. 2012;3(1):81–90. , doi: 10.1016/j.jare.2011.05.001

[56] Algarni M, Ghazali S. Comparative study of the sensitivity of pla, abs, peek, and petg's mechanical properties to fdm printing process parameters. Crystals. 2021;11(8). , doi: 10.3390/cryst11080995

[57] K Blake Perez. Design Innovation with Additive Manufacturing (AM): An AM-centric Design Innovation Process. Singapore Univ Technol Des. 2018;168.

[58] Backgrounder On Radioactive Waste | NRC.gov [Internet]. [cited 2022 May 25]. Available from: https://www.nrc.gov/reading-rm/doc-collections/fact-sheets/radwaste.html#stor

[59] Lloyd WR, Sheaffer MK, Sutcliffe WG. Dose rate estimates from irradiated light-water0reactor fuel assemblies in Air. 1994;

[60] Al-Sheikhly M, Christou A. How Radiation Affects Polymeric Materials. IEEE Trans Reliab. 1994;43(4):551–6. , doi: 10.1109/24.370227

[61] Bhattacharya A. Radiation and industrial polymers. Prog Polym Sci. 2000;25(3):371–401. , doi: 10.1016/S0079-6700(00)00009-5

[62] Makuuchi K, Cheng S. Fundamentals of Radiation Crosslinking. Radiat Process Polym Mater its Ind Appl. 2011;26–70. , doi: 10.1002/9781118162798.ch2

[63] Bhat S. 12 - 3D printing equipment in medicine [Internet]. 3D Printing in Medicine and Surgery. Elsevier (Singapore) Pte Ltd; 2020. 223–261 p. , doi: 10.1016/B978-0-08-102542-0/00012-9

[64] Petrovic V, Vicente J, Gonzalez H, Jorda O, Portole L, Gordillo JD, et al. Additive layered manufacturing : sectors of industrial application shown through case studies. 2011;49(4):1061–79. , doi: 10.1080/00207540903479786

[65] Silva Aquino KA da. Sterilization by Gamma Irradiation. Gamma Radiat. 2012; , doi: 10.5772/34901

[66] Martin H, Watson S, Lennox B, Poteau X. Miniature Inspection Robot for Restricted Access eXploration (MIRRAX). WM2018 Conf. 2018;1–9.

[67] Jones AR, Griffiths A, Joyce MJ, Lennox B, Watson S, Katakura JI, et al. On the design of a remotely-deployed detection system for reactor assessment at fukushima daiichi. In: 2016 IEEE Nuclear Science Symposium, Medical Imaging Conference and Room-Temperature

Semiconductor Detector Workshop, NSS/MIC/RTSD 2016. 2017. p. 7–10. , doi: 10.1109/NSSMIC.2016.8069713

[68] Wong JY, Pfahnl AC. 3D printing of surgical instruments for long-duration space missions. Aviat Sp Environ Med. 2014;85(7):758–63. , doi: 10.3357/ASEM.3898.2014

[69] Rochus P, Plesseria JY, Van Elsen M, Kruth JP, Carrus R, Dormal T. New applications of rapid prototyping and rapid manufacturing (RP/RM) technologies for space instrumentation. Acta Astronaut. 2007;61(1–6):352–9. , doi: 10.1016/j.actaastro.2007.01.004

[70] Wady P, Wasilewski A, Brock L, Edge R, Baidak A, McBride C, et al. Effect of ionising radiation on the mechanical and structural properties of 3D printed plastics. Addit Manuf [Internet]. 2020;31(October 2019):100907. , doi: 10.1016/j.addma.2019.100907

[71] West C, McTaggart R, Letcher T, Raynie D, Roy R. Effects of gamma irradiation upon the mechanical and chemical properties of 3D-printed samples of polylactic acid. J Manuf Sci Eng Trans ASME. 2019;141(4). , doi: 10.1115/1.4042581

[72] The ExoMars spacecraft measured radiation in deep space to help keep future astronauts safe [Internet]. [cited 2022 May 25]. Available from: https://www.popsci.com/exomars-radiation-astronauts/

[73] Benton ER, Benton E V. Space radiation dosimetry in low-Earth orbit and beyond. Nucl Instruments Methods Phys Res Sect B Beam Interact with Mater Atoms. 2001;184(1–2):255–94. , doi: 10.1016/S0168-583X(01)00748-0

[74] Berger T. Radiation dosimetry onboard the International Space Station ISS. Z Med Phys. 2008;18(4):265–75. , doi: 10.1016/j.zemedi.2008.06.014

[75] BS EN ISO 11137-2-2013--[2022-05-25--11-29-14 AM].pdf.

[76] TEPCO : Recent Topics:TEPCO HOLDINGS SENT ROBOT INTO FUKUSHIMA DAIICHI UNIT 2 REACTOR TO CLEAR PATH FOR LATER INVESTIGATION WITH “SCORPION” ROBOT [Internet]. [cited 2022 May 25]. Available from: https://www.tepco.co.jp/en/press/corp-com/release/2017/1375551_10469.html

[77] Benavente R, Mijangos C, Perena JM, Krumova M, López D. Effect of crosslinking on the mechanical and thermal properties of poly (vinyl alcohol). Polymer (Guildf). 2000;41:9265–72.

[78] Shaffer S, Yang K, Vargas J, Di Prima MA, Voit W. On reducing anisotropy in 3D printed polymers via ionizing radiation. Polymer (Guildf) [Internet]. 2014;55(23):5969–79. , doi: 10.1016/j.polymer.2014.07.054

[79] Kim E, Shin YJ, Ahn SH. The effects of moisture and temperature on the mechanical properties of additive manufacturing components: Fused deposition modeling. Rapid Prototyp J. 2016;22(6):887–94. , doi: 10.1108/RPJ-08-2015-0095

[80] Benyathiar P. Effect of ionizing irradiation techniques on biodegradable packaging materials [Internet]. ProQuest Dissertations and Theses. 2014. p. 253.

[81] Rankouhi B, Delfanian F, McTaggart R, Letcher T. An Experimental Investigation of the Effects of Gamma Radiation on 3D Printed ABS for In-Space Manufacturing Purposes. 2016;(November). , doi: 10.1115/imece2016-67745

[82] Rankouhi B, Javadpour S, Delfanian F, McTaggart R, Letcher T. Experimental Investigation of Mechanical Performance and Printability of Gamma-Irradiated Additively Manufactured ABS. J Mater Eng Perform [Internet]. 2018;27(7):3643–54. , doi: 10.1007/s11665-018-3463-y

[83] Skiens W. Mechanical properties of polymeric packaging films after radiation sterilization. Radiat Phys Chem. 1980;15:47–57.

[84] Calderón-Ardila R, Jaimes-Motta A, Peña-Rodríguez J, Sarmiento-Cano C, Suárez-Durán M, Vásquez-Ramírez A. Modeling the LAGO's detectors response to secondary particles at ground level from the Antarctic to Mexico. Proc Sci. 2021;358(December 2021). , doi: 10.22323/1.358.0412

[85] PETG vs PLA Filament: The Differences | All3DP [Internet]. [cited 2022 Aug 22]. Available from: https://all3dp.com/2/petg-vs-pla-3d-printing-filaments-compared/

[86] Why ASA filament is better than ABS - Filamentive [Internet]. [cited 2022 Aug 22]. Available from: https://www.filamentive.com/why-asa-filament-is-better-than-abs/

[87] Kabanov VY, Feldman VI, Ershov BG, Polikarpov AI, Kiryukhin DP, Apel' PY. Radiation chemistry of polymers. Vol. 43, High Energy Chemistry. 2009. p. 1–18. , doi: 10.1134/S0018143909010019

[88] Kim D geon, Lee S, Park J, Son J, Kim TH, Kim YH, et al. Performance of 3D printed plastic scintillators for gamma-ray detection. Nucl Eng Technol [Internet]. 2020;52(12):2910–7. , doi: 10.1016/j.net.2020.05.030

[89] Chen T, Jiang G, Li G, Wu Z, Zhang J. Poly(ethylene glycol-co-1,4-cyclohexanedimethanol terephthalate) random copolymers: Effect of copolymer composition and microstructure on the thermal properties and crystallization behavior. RSC Adv. 2015;5(74):60570–80. , doi: 10.1039/c5ra09252c

[90] Yang Z, Peng H, Wang W, Liu T. Crystallization behavior of poly(ε-caprolactone)/layered double hydroxide nanocomposites. J Appl Polym Sci. 2010;116(5):2658–67. , doi: 10.1002/app

[91] Chen T, Zhang W, Zhang J. Alkali resistance of poly(ethylene terephthalate) (PET) and poly(ethylene glycol-co-1,4-cyclohexanedimethanol terephthalate) (PETG) copolyesters: The role of composition. Polym Degrad Stab [Internet]. 2015;120:232–43. , doi: 10.1016/j.polymdegradstab.2015.07.008

[92] Guo RH, Jiang SQ, Yuen CWM, Ng MCF. Microstructure and electromagnetic interference shielding effectiveness of electroless Ni-P plated polyester fabric. J Mater Sci Mater Electron. 2009;20(8):735–40. , doi: 10.1007/s10854-008-9795-x

[93] Gracias DH, Zhang D, Shen YR, Somorjai GA. Surface chemistry-mechanical property relationship of low density polyethylene: An IR+visible sum frequency generation spectroscopy and atomic force microscopy study. Tribol Lett. 1998;4(3–4):231–5. , doi: 10.1023/a:1019175826460

[94] Paszkiewicz S, Szymczyk A, Pawlikowska D, Irska I, Taraghi I, Pilawka R, et al. Synthesis and characterization of poly(ethylene terephthalate-: Co -1,4-cyclohexanedimethylene terephtlatate)- block -poly(tetramethylene oxide) copolymers. RSC Adv [Internet]. 2017;7(66):41745–54. , doi: 10.1039/c7ra07172h

[95] Dispenza C, Alessi S, Spadaro J. Radiation processing of polymers in aqueous media. Applications of Ionizing Radiation in Materials Processing [Internet]. 2017. 291–326 p.

[96] Kökçan YE, Tamer Y. Effect of O-MMT content on properties of poly (Vinyl chloride)/poly (acrylonitrile styrene acrylate) blends. J Turkish Chem Soc Sect A Chem. 2020;7(3):635–48. , doi: 10.18596/jotcsa.635095

[97] Zhang Y, Xu Y, Song Y, Zheng Q. Study of poly(vinyl chloride)/acrylonitrile-styrene-acrylate blends for compatibility, toughness, thermal stability and UV irradiation resistance. J Appl Polym Sci. 2013;130(3):2143–51. , doi: 10.1002/app.39405

[98] Orlov AS, Kiselev SA, Kiseleva EA, Budeeva A V., Mashukov VI. Determination of styrene-butadiene rubber composition by attenuated total internal reflection infrared spectroscopy. J Appl Spectrosc. 2013;80(1):47–53. , doi: 10.1007/s10812-013-9719-2

[99] Al-Sheikhly M, Christou A. Tutorial How Radiation Affects Polymeric Materials. IEEE Trans Reliab. 1994;43(4):551–6. , doi: 10.1109/24.370227

[100] Guessasma S, Belhabib S, Nouri H. Microstructure, Thermal and Mechanical Behavior of 3D Printed Acrylonitrile Styrene Acrylate. Macromol Mater Eng. 2019;304(7):1–11. , doi: 10.1002/mame.201800793

[101] Szykiedans K, Credo W, Osiński D. Selected Mechanical Properties of PETG 3-D Prints. Procedia Eng [Internet]. 2017;177:455–61. , doi: 10.1016/j.proeng.2017.02.245

[102] Santana L, Alves JL, Sabino Netto A da C, Merlini C. A comparative study between PETG and PLA for 3D printing through thermal, chemical and mechanical characterization. Rev Mater. 2018;23(4). , doi: 10.1590/s1517-707620180004.0601

[103] Modeling D, Hsueh M hsien, Lai C jung, Wang S hao, Zeng Y shan, Hsieh C hsin, et al. Effect of Printing Parameters on the Thermal and Mechanical Properties of 3D-Printed PLA and PETG , Using Fused. Vol. 13, Polymers. 2021. p. 1–11.

[104] Polymer additive manufacturing of ASA structure Influence of printing.pdf.

[105] Grabowik C, Kalinowski K, Ćwikła G, Paprocka I, Kogut P. Tensile tests of specimens made of selected group of the filament materials manufactured with FDM method. MATEC Web Conf. 2017;112:1–6. , doi: 10.1051/matecconf/201711204017

[106] Quickast. FDM printing [Internet]. 2019. Available from: http://quickastmaker.com/fdm-3d-printing/

[107] University of Loughbrorough. The 7 Categories of Additive Manufacturing [Internet]. Available from: https://www.lboro.ac.uk/research/amrg/about/the7categoriesofadditivemanufacturing/

[108] Hollister SJ. Porous scaffold design for tissue engineering. Nat Mater. 2005;4(July):518–524. , doi: https://doi.org/10.1038/nmat1421

[109] Tren SJ, Awad A, Goyanes A, Gaisford S, Basit AW. 3D Printing Pharmaceuticals : Drug Development to Frontline Care. , doi: 10.1016/j.tips.2018.02.006

[110] Harrysson OLA, Cansizoglu O, Marcellin-Little DJ, Cormier DR, West HA. Direct metal fabrication of titanium implants with tailored materials and mechanical properties using electron beam melting technology. Mater Sci Eng C. 2008;28(3):366–73. , doi: 10.1016/j.msec.2007.04.022

[111] OPTOMEC [Internet]. Available from: https://optomec.com/

[112] CRPtechnology.

[113] Zhang Y, Liu H. Application of Rapid Prototyping Technology in Die Making of Diesel Engine. Vol. 14, Tsinghua Science and Technology. 2009. p. 127–31. , doi: 10.1016/S1007-0214(09)70079-3

[114] Wiedemann B, Jantzen HA. Strategies and applications for rapid product and process development in Daimler-Benz AG. Comput Ind. 1999;39(1):11–25. , doi: 10.1016/S0166-3615(98)00126-2

[115] Ilardo R, Williams CB. Design and manufacture of a Formula SAE intake system using fused deposition modeling and fiber-reinforced composite materials. 20th Annu Int Solid Free Fabr Symp SFF 2009. 2009;(Figure 1):770–80.

[116] Buswell RA, Soar RC, Gibb AGF, Thorpe A. Freeform Construction: Mega-scale Rapid Manufacturing for construction. Autom Constr. 2007;16(2):224–31. , doi: 10.1016/j.autcon.2006.05.002

[117] Buchanan C, Gardner L. Metal 3D printing in construction : A review of methods , research , applications , opportunities and challenges. Eng Struct [Internet]. 2019;180(March 2018):332–48. , doi: 10.1016/j.engstruct.2018.11.045

[118] Rouhana C, Faek F, Jazzar M El, Hamzeh F. THE REDUCTION OF CONSTRUCTION DURATION BY IMPLEMENTING. 2014;(March 2015). , doi: 10.13140/RG.2.1.1718.4646/1

[119] Review SAT year, Jamali K, Kaushal V. Evolution of Additive Manufacturing in Civil Infrastructure. 2021;1–7.

Appendix

Additive manufacturing process types

1. Material Extrusion

Fused Deposition modelling (FDM) is a liquid-based material extrusion process which deposits thermoplastics in a predefined tool path. The polymer, which is heated in a hot end, is extruded through a nozzle. Once the material has cooled, the desired geometry is formed. Using several stepper motors, the deposition location can be controlled by moving the gantry to which the nozzle is attached. The cost of FDM printers and materials has significantly reduced in previous years. FDM has risen in popularity in recent years primarily due to the low equipment and material cost. This has made FDM printing accessible to researchers, industry, hobbyists, and 'at home' inventors [33]. More details on FDM are provided in Section 2.3.4.

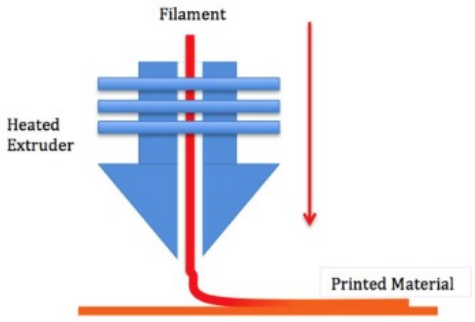

Figure 6.1 *– Diagram of FDM nozzle and deposition method* [106]

2. Vat polymerisation

Stereolithography (SLA) was the first type of AM technology to emerge. Using photosensitive resin, a UV light source, and an LED, cross sections of the desired geometry are cured, the bed is moved up, and the next cross-section is cured. SLA can achieve a significantly higher resolution than FDM, as the limiting factor is the resolution of the LED. SLA requires post-processing work to remove excess resin after printing. This is usually done by submerging the part in isopropanol alcohol (IPA) and blanketing the part in UV light to cure excess resin fully.

Polyjet printing has developed from the well-established inkjet printing process. Similarly, to FDM, the print head is attached to a gantry which moves to deposit material selectively. Polyjet printing jets photosensitive resin which is quickly cured by a UV light source. Unlike SLA, Polyjet allows the mixing

of materials while maintaining a high resolution. Polyjet can produce strong parts with excellent accuracy and is capable of printing on a large scale than SLA.

3. Sheet lamination

Sheet Lamination bonds thin sheets of materials together. Typical materials include paper, plastics and metal foils. Common examples of this classification are Lamination Object Manufacturing (LOM) and Ultrasonic Consolidation (UC). Sheet lamination is a cheap and rapid manufacturing method that can create composite parts by swapping the sheet material during fabrication. However, sheet lamination is a relatively low-accuracy process.

4. Powder bed fusion

Selective laser melting (SLM) was an early form of AM to emerge. This method uses a powdered metal which is preheated before fabrication. A laser is then used to scan the layer into the powder, which mechanically joins the powder together. This method uses unfused powder as a support structure, so overhangs are not an issue during design. SLM allows metal parts to be fabricated with significantly better mechanical properties than the FDM or SLA. Post-processing is required to remove excess unfused material from the part.

Electron beam melting (EMB) is similar to SLM, using a bed or powered material and selectively melting material together. The main difference is the heat source which uses an electron gun in a vacuum to fuse material. EMB is faster than laser alternatives; however, the parts produced are not as accurate, and the print volume is reduced.

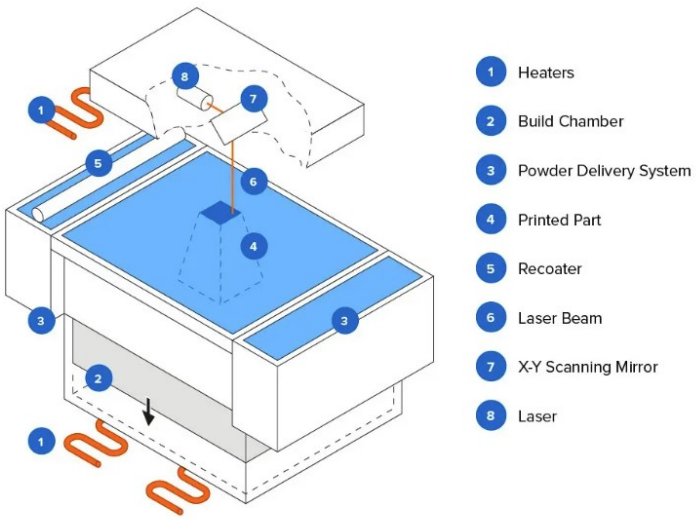

Figure 6.2 *– Diagram of powder bed fusion AM process taken from* [107]

5. Binder jetting

Binder jetting is a bi-material process. Typically, one material is in a powdered form, and the other is a liquid. The liquid material (binder) is an adhesive for the powdered material. The binder is selectively deposited onto the powdered material for the part. Similarly, to powder bed fusion, the print is self-supported by non-bonded powder. Binder jetting can fabricate many materials, including metals, polymers, and glass.

Further information on the categories and types of AM processes can be found on Loughborough Universities' page [107].

Applications of AM

The increased interest in AM for rapid prototyping (RP) and manufacturing can be seen across various sectors. These industries are leveraging the advantages AM solutions have over traditional manufacturing techniques.

1. Medical

AM technologies have many applications in the medical industry. Specifically, SLA has successfully been used to fabricate prosthetics and bone transplants. Printing bone transplants allows the density, porosity and geometry to be controlled, Figure 2.8. These factors are essential for the body to accept foreign objects and encourage growth from existing tissues. Additionally, The mechanical strength of the implants increases and the risk of inflammation is decreased [108] [64] [63]. Another exciting advancement in the medical industry enabled by 3D printing is the development of pharmaceuticals. 3D printing allows medicines to be personalised on demand to the patient's needs[109].

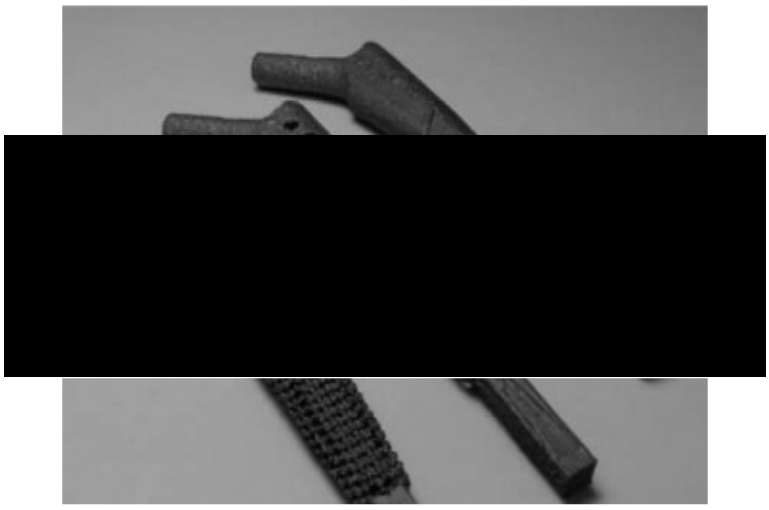

Figure 6.3 – *Porosity controlled hip stems using EBM* [110]

2. Aerospace

AM is well suited for the aerospace industry as complex geometries can be produced. This allows high-strength, low-weight parts to be fabricated from engineering-grade materials [40]. Additionally, aerospace production is limited to small production volumes. The Laser Engineering Net Shape (LENS) process has been used to fabricate components for helicopters, satellites and jet engines [111]. Studies have shown that AM solutions can reduce material usage by 40% whilst maintaining the same critical mechanical properties [64].

3. Automotive

The automotive industry relies on new product development to stay competitive in a saturated smarket. However, this is a costly and time-consuming process. AM technologies are being used to aid the design. Scaled concept cars have been fabricated using SLA [112]. On the other end of the spectrum, SLS and EBM have been used to produce high-performance parts components for F1 gearboxes, mould core fabrication for engine block casting, and titanium lattice structural engine components[40] [112] [113] [114]. FDM has been used to fabricate complex geometries such as manifolds which can then be reinforced with a fibre layup process, Figure 2.9.

Figure 6.4 *– FDM printed intake manifold (Left), Composite layup and electronics added (Right)* [115]

4. Civil

The civil industry has recently developed technologies that allow 3D printing of structural components [116], Figure 2.10, or entire civil structures, including home sand bridges [117]. Incorporating AM into a civil project will lead to less labour, reduce work-based accidents, reduce waste associated with building infrastructure, and improve designer freedom for architects [118] [119].

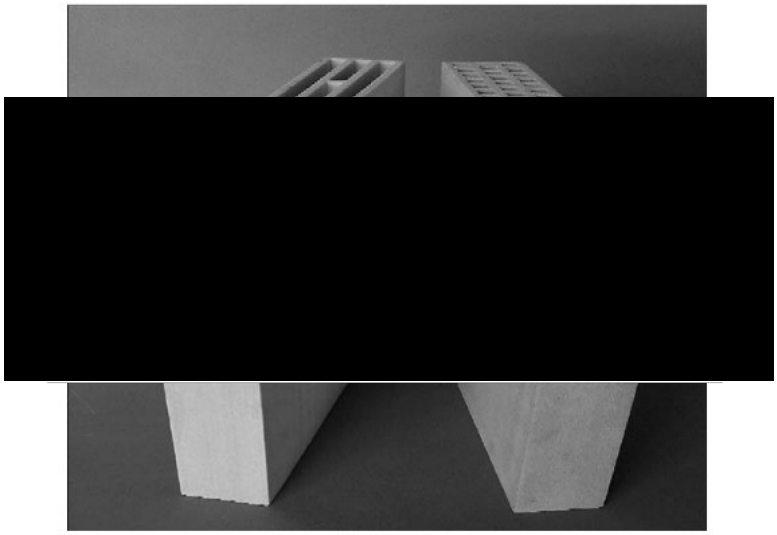

Figure 6.5 *– Gypsum concrete panels designed to minimise thermal conductivity* [116]